Synthesis and Study of Zn(Mn) Ferrite Nanoparticles, Thin Films and Zn(Mn) Ferrite-BaTiO₃ Composites

A thesis submitted to University of Hyderabad in partial fulfillment for the award of the degree of Doctor of Philosophy.



by

Atiya Farheen (Reg. No. 14PHPH03)

Supervisors:

Prof. Rajender Singh Dr. Venkataiah Gorige

School of Physics University of Hyderabad Hyderabad, Telangana-500 046, India



DECLARATION

I, Atiya Farheen hereby declare that the thesis entitled "Synthesis and Study of Zn(Mn) Ferrite Nanoparticles, Thin Films and Zn(Mn) Ferrite-BaTiO₃ Composites" submitted by me for the award of the degree of Doctor of Philosophy in Physics is done under the supervision of Prof. Rajender Singh and Dr. Venkataiah Gorige, School of Physics, University of Hyderabad, India is a bonafide research work and is free from plagiarism. I hereby declare that it has not been submitted previously partially or fully to this University or any other university or institution for the award of any degree or diploma.

Atiya Farheen Reg. No.:14PHPH03 School of Physics University of Hyderabad Hyderabad, India

Place: Hyderabad

Date:



CERTIFICATE

This is to certify that the research work presented in the thesis entitled "Synthesis and Study of Zn(Mn) Ferrite Nanoparticles, Thin Films and Zn(Mn) Ferrite-BaTiO₃ Composites" submitted by Ms. Atiya Farheen bearing the Reg. No 14PHPHO3 in partial fulfillment of the requirements for the award of Doctor of Philosophy in the School of Physics is a bonafide work carried out by her under my direct supervision in the School of Physics, University of Hyderabad, India.

This thesis is free from plagiarism and has not been submitted previously in part or in full to this University or any other University or institution for the award of any degree or diploma. Further, the student has the following publications and conference proceedings before the submission of the thesis for adjudication.

International Journal papers

- 1. **Atiya Farheen** and Rajender Singh, Effect of hydrothermal annealing on structure and magnetic properties of RF sputtered Mn-Zn Ferrite thin films, *Material research express* **6** (2019).
- 2. **Atiya Farheen** and Rajender Singh, Effect of Mn Substitution on Structure and Magnetic Properties of Cobalt Ferrite nanoparticles, *Integrated Ferroelectrics* **203**, 91-96 (2019).
- 3. **Atiya Farheen** and Rajender Singh, FMR and Magnetic studies of RF-sputtered Mn-Zn ferrite thin films, *J. Superconductivity and Novel Magnetism* **32** (2019).
- 4. **Atiya Farheen** and Rajender Singh, Synthesis of ferrimagnetic/ferroelectric composite and its magnetic and electrical characterization, *Integrated Ferroelectrics* **193**, 31–35 (2018).
- 5. **Atiya Farheen**, Thirupathi Gadipelly and Rajender Singh, Multiferroic properties of ferromagnetic and ferroelectric coupled Mn-Zn Ferrite and BaTiO₃ composites, *Ferroelectrics* **516**, 82-89 (2017).

Conference Proceedings

- 1 **Atiya Farheen** and Rajender Singh, Structure and Magnetic Properties of Superparamagnetic Ferrite Nanoparticles, *IOP Conf. Ser.: Mater. Sci. Eng.* 577 012057 (2019).
- 2 **Atiya Farheen** and Rajender Singh, Effect of Sintering on Structure and Magnetic Properties of Mn-doped Zn Ferrite, *AIP Conference Proceedings* 1953, 120067 (2018).

- 3 **Atiya Farheen**, Thirupathi Gadipelly and Rajender Singh, Electrical Relaxations Studies of Ferromagnetic-Ferroelectric Composites, *AIP Conference Proceedings* 1832, 040019 (2017).
- 4 **Atiya Farheen**, Thirupathi Gadipelly and Rajender Singh, Microstructure and magnetic properties of RF sputtered Mn-Zn ferrite thin films, *ISBN No.* 978-81-931227-0-9 (2015).

Manuscript under preparation

- 1 Atiya Farheen and Rajender Singh, Structural, magnetic and dielectric properties of Mn-Zn ferrite nanoparticles (to be communicated).
- 2 Atiya Farheen and Rajender Singh, Structural, magnetic and electrical characterization of BaTiO₃/Mn_{0.1}Zn_{0.9}Fe₂O₄ composite ceramics (to be communicated).

Presentation at Conferences

- 1. Poster Presentation at 5th International conference on Nanoscience and Nanotechnology (ICONN 2019), Tamil Nadu, India, 28-30 January 2019.
- 2. Poster Presentation at the International conference on Nano-Structured Materials & Devices (ICNSMD 2018), New Delhi, India, 17-20 December 2018.
- 3. Poster Presentation at International Conference on Magnetic Materials and Applications (ICMAGMA-2018), Bhubaneswar, India, 9-13 December 2018.
- 4. Poster Presentation at International Conference on Advances in Materials & Manufacture Applications (ICONAMMA 2018), Bangalore, India, 16-18 August 2018.
- 5. Attended workshop on "Functional Magnetic Materials" organized by the University of Hyderabad, Hyderabad-India 26th February 3rd March 2018.
- 6. Attended workshop on "Processing and Characterization of Thin Films" organized by the University of Hyderabad, Hyderabad-India, 3-9 January 2018.
- 7. Poster Presentation at 6th International Symposium on Integrated Functionalities (ISIF 2017), New Delhi, India, 10-13 December 2017.
- 8. Poster Presentation at 2nd International Conference on condensed matter & Applied Physics (ICC-2017), Bikaner, India, 24-25 November 2017.
- 9. Poster Presentation at International Conference on Magnetic Materials and Applications (ICMAGMA-2017), Hyderabad, India, 1-3 Feb, 2017.
- 10. Poster Presentation at DAE Solid State Physics Symposium (DAE SSPS 2016), Bhubaneswar, India, 26-30 December 2016.
- 11. Poster Presentation at International Conference on Technologically Advanced Materials and Asian Meeting on Ferroelectricity (ICTAM-AMF 10), New Delhi, India, 7-11 November 2016.

- 12. Poster Presentation at International Conference on Magnetic Materials and Applications (ICMAGMA-2015), Vellore, India, 2-4 December, 2015.
- 13. Poster Presentation at First National Conference on Advanced Nanomaterials (CAN-2015), Kerala, India, 1-3 October 2015.

Further, the student has passed the following course towards the fulfillment of course work required for the Ph.D.

S. No.	Course code	Name	Credits	Pass/Fail
1	PY801	Advanced quantum mechanics	4	Pass
2	PY803	Advanced Statistical mechanics	4	Pass
3	PY804	Advanced electromagnetic theory	4	Pass
4	PY821	Research Methodology	4	Pass

Prof. Rajender Singh

Dr. Venkataiah Gorige

Dean School of Physics University of Hyderabad

Place: Hyderabad

Date:

ACKNOWLEDGMENTS

At first, I would like to express all my thanks and praise to Allah, for uncountable blessings.

Next, I would like to owe my deepest gratitude to my supervisor, Professor Rajender Singh. He is the person who suggested this work. His invaluable guidance and thoughtful suggestions over the entire period of my research at the School of Physics, University of Hyderabad are appreciated. Daily interaction, valuable discussions improved my experimental skills and analysis capabilities.

I would like to thank my co-supervisor Dr. Venkataiah Gorige and my doctoral committee members Prof. S. V. S. Nageswara Rao, Dr. Ashok V. Udyagiri and Prof. P. K. Suresh for their suggestions throughout my research period. I am thankful to all the former and present deans, School of Physics for providing me the facilities. I also thank all the faculty members who have helped me throughout my Ph.D.

I am grateful to all the non-teaching and technical staff of the School of Physics specially: Mr. Abraham, Ms. Deepika, Mr. Sudarshan, Mr. Narsimha, Mr. Sekhar, Mr. Prasad, Ms. Shailaja, Ms. Jyothi, Ms. Sunitha, Mr. Santosh, Mr. Naresh, Mr. Laxminarayana, and Ms. Arundhathi. I thank the staff of central instruments laboratory (CIL) Dr. S. M. Ahmed (PSO), Dr. S. Manjunath, Mr. Suresh, Mr. Sudhakar, Mr. Pavan Mr. Rajesh, Mr. Nagaraju for the technical support. I also thank Mr. Mantoo Kumar, Giri and Mr. Sai for their help. I thank XRD operators from SEST Mr. Mallesh and Mr. Dinakar and Nanotechnology Technical Staff Mr. Pankaj, Mr. Prasanth, Mr. Durgaprasad, Ms. Sandhya, and Ms. Grace David for their help.

I would like to thank all of my seniors and lab mates Dr. G. Thirupathi, Dr. A. Ramesh, Dr. M. Padmavathi, Dr. Jasmeet Kaur, Mr. K. Ravi Babu, and Ms. Nisha Gautam.

I would like to thank Prof. S. Srinath for allowing me to do the measurements in his lab. I am very thankful to Dr. Binoy Krishna Hazra, Ms. Leelashree, and Mr. Sarthak for their help in measurements.

Now, I would like to thank my friends, batch-mates, and all research scholars at the School of Physics: Mr. Pradeep, Mr. Junaid, Mr. Mahinder, Ms. Akshara, Mr. Pundareekam, Mr. Avisek, Mr. Naresh, Mr. Nilanjan, Ms. Praneetha, Mr. B. Kranthi Kumar, Ms. Manasa, Ms. Leelashree, Ms. Atasi, Ms. Pooja, Ms. Aishwarya, Ms. Debika, and all other SoP friends.

I would like to especially thank my friends Ms. Anupama, Ms. Nisha, and Mr. Chakradhara.

A special thanks to my friends from other departments Ms. Nidhi, Ms. Sybil, Ms. Nisha Singh, Ms. Annapurna, and Ms. Sakhina for their friendship during my stay in the hostel. Also, I would like to thank my present and past friends.

Finally, I would like to mention the support and encouragement of my family members throughout my life. My parents (Mr. Sayad Mohd Fayak and Mrs. Shahnaz Parveen) who gave me life and grew me up, my sister Neha and brother Zaid with them I have shared my childhood experiences. Special thanks to the one who has given me moral support and encouragement my husband Mr. Majid. Also, I would like to thanks my in-laws for their support. At last, I can say the efforts of my entire family were, and still are, made me capable to attain my goals in reality. I want to dedicate this work to my family.

I also thank all my teachers who kept me in the right direction and supported. Still, so many people helped me in different stages or situations. Though I have not listed their names here, those all are in my heart, Thank you one and all.

I would like to thank the Department of Science and Technology (DST) India for providing me financial assistance under the scheme "DST-INSPIRE fellowship" during my Ph. D. tenure.

(Atiya Farheen)

Dedicated to

My Family....

ABSTRACT

In recent years, great interest has been focused on ferrites because of their vast range of technological applications in electronics and communication engineering. The main advantage of ferrites is that, by the introduction of a relatively small amount of foreign ions, important modification in structure and magnetic properties can be obtained. Ferrite nanoparticles, thin films, and ferromagnetic-ferroelectric (FM-FE) composites have several applications. The study of such systems is quite interesting and challenging to find improved characteristics in research and development. Therefore, the present work includes the study of ferrite nanoparticles, ferrite thin films and ferromagnetic-ferroelectric composites. The Mn_xZn_{1-x}Fe₂O₄ (x=0 to 1) (ZMF) nanoparticles were prepared via chemical coprecipitation whereas BaTiO₃ (BTO) was prepared via hydrothermal method. The Mn_{0.5}Zn_{0.5}Fe₂O₄ thin films were fabricated via RF-magnetron sputtering, and the FM-FE composites were prepared via the solid-state route.

To understand the effect of Mn-doping on the properties of ferrite nanoparticles, we have done a detailed structural, morphological, and magnetic studies of the synthesized nanoparticles. Structural studies of the prepared nanoparticles confirm the formation of cubic spinel structured nanosize ferrite with 5 to 70 nm particle size. The magnetization of the prepared ferrite nanoparticles is found to increase with increasing Mn-doping due to alteration in cation distribution and an increase in crystallite size. Ferromagnetic resonance studies show an increase in the internal field of nanoparticles with the increase in Mn-doping, which is indicative of dominant ferromagnetic interactions for Mn-rich samples. These results confirm that crystallographic parameters are related to the magnetic properties of the ferrite nanoparticles.

The structural and morphological studies of the prepared ferrite thin films confirm the single-phase cubic spinel structure with the nano-cluster formation in the films. It is found that the magnetic and optical parameters of the prepared thin films are related to the crystallographic parameters and deposition conditions. The magnetization versus field plots reveals the soft ferrimagnetic behavior of the synthesized films. The angle-dependent magnetization and ferromagnetic resonance studies confirm the presence of magnetic anisotropy in the prepared thin films.

Multiferroic composites of Mn_{0.5}Zn_{0.5}Fe₂O₄ (ZMF) with barium titanate were well-studied. The structural, morphological, magnetic and electrical properties of composites were taken into account to understand the multiferroics behavior of the prepared composites. The structure and morphology confirm the coexistence of ZMF and BTO phases in the composites. The magnetization is found to increase through the inclusion of ferrite because of the mixture rule. The existence of a magnetic hysteresis loop and *P-E* hysteresis loop is an indication of magnetic and electric ordering in the FM-FE composites. The FM-FE composites show a decrease in dielectric constant value with an increase in the dielectric loss by increasing ferrite-content. It is found that magnetic, electric and dielectric properties of composites strongly depend on the microstructure of the sample and ferrite percentage.

CONTENTS

Chapter 1: Introduction	
1.1 Applications of ferrite	1
1.2 Structure of ferrites	3
1.3 Fundamentals of Magnetism	5
1.3.1 Exchange interactions	5
1.3.2 Magnetic anisotropy	8
1.4 Applications of ferrimagnetic-ferroelectric Composite	11
1.5 Structure of Barium titanate (BaTiO ₃)	12
1.6 Aim	13
1.7 Objectives of the present study	13
1.8 Organisation of the thesis	14
References	16
Chapter-2: Preparation and characterization Techniques	
2.1 Material Preparation methods	2 1
2.1.1 Synthesis of ferrite nanoparticles	22
2.1.2 Synthesis of BaTiO ₃ (BTO) nanoparticles	23
2.1.3 Synthesis of multiferroic bulk composite	24
2.1.4 Preparation of sputtering target	25
2.1.5 Deposition techniques of thin films	26
2.2 Characterization techniques	29
2.2.1 X-ray diffraction	29
2.2.2 Raman Spectroscopy	31
2.2.3 Field Emission Electron Microscopy	34
2.2.4 Spectrophotometer	36
2.2.5 Vibrating sample magnetometer	37
2.2.6 Ferromagnetic resonance spectroscope	38
2.2.7 Impedance analyzer	40
2.2.8 P. E. Loop Tracer	41
References	44

Chapter-3: Structural, morphological and magnetic properties of Mn-Zn ferrite

nanoparticles

3.5 FMR Study	66
3.6 Chapter Summary	68
References	69
Chapter-4: Structural, optical and magnetic properties of Mn-films	·Zn ferrite thin
4.1. Introduction	71
4.2 Selection of target composition for thin film deposition	71
4.3 Structural Study of MZF films	73
4.4 Microstructural Study of MZF films	76
4.5 Optical Study of MZF films	79
4.6 Magnetization Study of MZF films	84
4.7 FMR Study of the MZF films	88
4.8 Chapter Summary	94
References	95
Chapter-5: Structural, magnetic and electrical properties of M BaTiO ₃ composites	n _{0.5} Zn _{0.5} Fe ₂ O ₄ -
5.1 Composite multiferroic	97
5.2 Structural study of composites	99
5.3 Morphological study of composites	101
5.4 Magnetization study of composites	102
5.5 Electrical study of composites	105
5.6 Chapter Summary	111
References	112
Chapter-6: Summary and future scope	
6.1 Summary of the present work	115
6.2 Future Scope of the present work	118

Chapter 1

Introduction

The chapter deals with the general introduction and applications of magnetic nanoparticles and thin films. The historical background of ferrite, basic theories of magnetization and applications of the ferrimagnetic-ferroelectric composite are included in this chapter.

1.1 Applications of ferrite

Ferrites are important technological materials that are potential candidates for many applications like transformer cores, magneto-caloric refrigeration, high-density information storage in computers, magnetic recording, ferrofluid technology, spintronics, etc. [1-9]. Low permeability loss, high resistivity and strong magnetic coupling at microwave frequencies make them an irreplaceable candidate for microwave devices. Moreover, superexchange causes ferrimagnetism in the ferrites. However, magnetization is lower because of the opposite spin in ferrite. However, the resistivity of ferrites is higher than ferromagnetic materials because of the intrinsic atomic level interaction among oxygen and metal ions. Therefore they are useful in many high-frequency applications. Apart from this, ferrites are very useful in the preparation of multiferroic composite with sufficient magnetoelectric coupling when compared with single-phase multiferroic [10].

In recent years, miniaturization of electronic devices leads to a reduction in the size of magnetic materials up to nanometers dimensions [11]. Particle size reduction leads to an increase in the surface to volume ratio, which results in the alteration of the physical and chemical properties of ferrite. Therefore, nanoparticles of ferrite offer great advantages over bulk material and are found very useful in the field of medicine and biology [12-14], such as magnetically targeted drug delivery, MRI, etc. Ferrites are easy to prepare at a large scale with effective low cost. Ferrite properties are highly sensitive to the preparation condition and compositions [15-16]. Hence, controlled synthesis of ferrite nanoparticles of the desired dimensions and their

structural correlation with other physical properties have become an interesting area of activity for the scientific community [17-18].

Thin films of soft ferrite are also gaining scientific community attention as a potential candidate to replace their bulk counterpart in many electronic devices such as microwave devices [9], [19-21]. Ferrite thin films show high electric resistivity than the bulk counterpart. The difference in the properties of film compare to bulk arises because of the large surface-to-volume ratio, less thickness, and unique microstructure of the films [22-24]. In addition to this, ferrite films have applications in high-density magnetic recording, magnetic-optical recording, micro-transformers, magnetic sensors, high-frequency power supply, etc. Thus, ferrite nanoparticles and thin-film systems are quite interesting because of their magnetic and electronic properties differ from their bulk counterpart, as we have discussed above.

1.1.1 Ferrites

Similar to the ferromagnetic material, ferrites are also consists of domains and exhibit spontaneous magnetization with a typical hysteresis loop. Magnetic parameters like saturation magnetization, coercivity, permittivity, permeability, resistivity, etc. play an important role to define a particular application for the ferrite. These parameters can be controlled by manipulating porosity, grain size, and microstructure of ferrite. Ferrites show high resistivity (order of $10^7 \Omega$ m) with low eddy current losses [25-27], which makes them an efficient candidate in high-frequency electromagnetic applications [28].

In recent years, considerable efforts have been focused on the development of ferrimagnetic materials, especially Mn-Zn ferrite, because of their promising magnetic properties in high-frequency devices, magnetic resonance imaging, and spintronics devices, etc. [29-30]. Mn-Zn ferrite is a highly stable soft ferrimagnetic material due to the high moment Mn⁺² ion. The Zn⁺² ion in Mn-Zn ferrite control over the particle size and provides structural stability to the system. Curie temperature is high for Mn-Zn ferrite. The outstanding properties of Mn-doped Zn ferrite have found their applications in high-frequency devices [31-32].

1.2 Structure of ferrites

Ferrite is divided into various classes depending on the structure and magnetic properties, as they are listed in the following table [28].

Table 1.1: Classification of the ferrites.

Туре	Structure	Formula	Possible ions in the formula
Spinel	Cubic	M ²⁺ Fe ³⁺ ₂ O ₄	M ²⁺ = Ni ²⁺ , Mn ²⁺ , Co ²⁺ , Cu ²⁺ , Mg ²⁺ , Zn ²⁺ ions or a combination of these ions
Garnet	Cubic	R ³⁺ Fe ³⁺ ₅ O ₁₂	$R^{3+} = Y^{3+}, Gd^{3+},$
Hexaferrite	Hexagonal Magnetoplumbite	AFe ₁₂ O ₁₉ M-Type AM ₂ Fe ₁₆ O ₂₇ W-Type AM ₂ Fe ₂₃ O ₄₆ X-Type A ₂ M ₂ Fe ₁₆ O ₂₇ Y-Type A ₃ M ₂ Fe ₂₄ O ₄₁ Z-Type A ₄ M ₂ Fe ₃₆ O ₆₀ U-Type	A=Ba, Sr, Pb, Ca M ²⁺ = Fe ²⁺ , Ni ²⁺ , Mn ²⁺ , Zn ²⁺ , Mg ²⁺ ions or a combination of these ions
Ortho-ferrite	Orthorhombic Perovskite	R ³⁺ Fe ³⁺ O ₃	R is a rare-earth ion

All the ferrite mentioned in Table 1.1 shows different properties depending on their crystal structure. Therefore, each ferrite has applications in different areas [33]. Among all the ferrites, spinel ferrite is a simple class of magnetic material with a cubic close-packed structure. A- and B-site metal ions with oxygen cubic close-packed arrangement of spinel ferrite is demonstrated in Fig. 1.1. Top and bottom layers of oxygen create two different kinds of voids: one is tetrahedral while another one is octahedral.

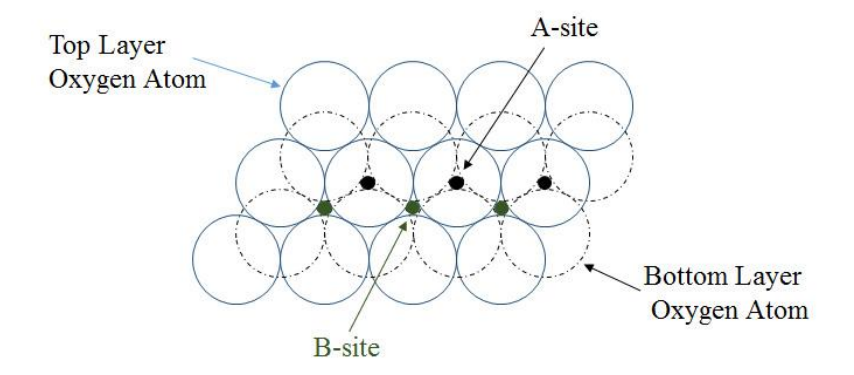


Figure 1.1. A- and B-site metal ions with oxygen cubic close-packed arrangement.

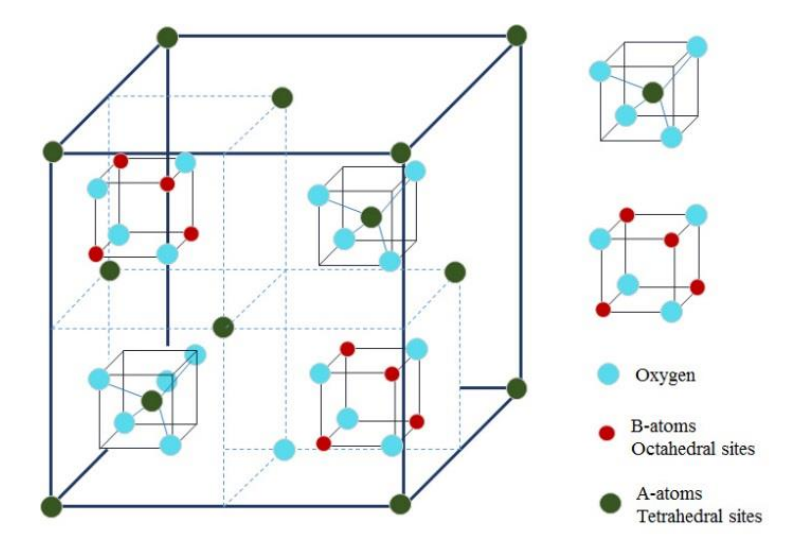


Figure 1.2. Schematic drawing of the spinel unit cell [34].

Fig. 1.2 demonstrates a diagram of a "cubic spinel unit cell". Oxygen atom sits on the corner of the cube to generate closed fcc cubic lattice. In general, a spinel structure contains two different kinds of magnetic sublattices: tetrahedral (A) with four nearby oxygen and another octahedral (B) with six nearby oxygen. Therefore, the general formula for spinel ferrites are written as " $(Me^{2+}_{(1-\varkappa)}Fe^{3+}_{\varkappa})[Me^{2+}_{\varkappa}Fe^{+3}_{(2-\varkappa)}]O_4$ ", whereas "Me" is a divalent metal ion. The degree of inversion ($_{\varkappa}$) is the fraction of trivalent cations (Fe⁺³ ions), which occupy the tetrahedral site. Inversion parameter ($_{\varkappa}$) describes the cation distribution of spinel ferrite as follows:

 $_{\varkappa} = 0$ for "normal spinel"

 $_{\varkappa} = 1$ for "inverse spinel"

 $0 < \kappa < 1$ for "mixed spinel" [35-36].

Parenthesis () and square [] brackets correspond to the A- and B-sites. The cation distribution among A- and B-sites determine the magnetic properties of spinel ferrites [7], [37-39]. The following table lists the magnetic moments of metal ion on tetrahedral sites.

Metal Ion	Theoretical moment	Experimental moment
Mn^{+2}	5	4.6
Fe	4	4.1
Co ⁺²	3	3.7
Ni	2	2.3
Cu ⁺²	1	1.3
Mø	0	1.1

Table 1.2: Magnetic moment of metal ion on tetrahedral sites.

1.3 Fundamentals of Magnetism

As we know, electrical charge motion produces a magnetic field. Similarly, in atoms, the motion of "electron-spin" and "orbital-angular momentum" around the nucleus generates a magnetic moment, as demonstrated in Fig. 1.3. An atom's net magnetic moment is the addition of every constitutive electron's magnetic moment [36], [40].

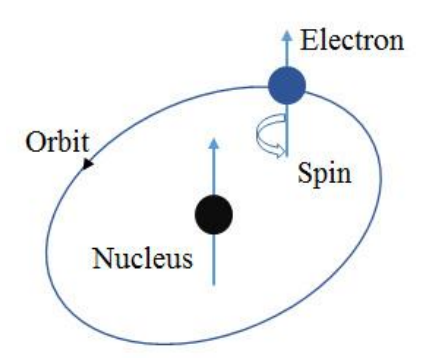


Figure 1.3. The spinning electron's orbit around the nucleus.

1.3.1 Exchange interactions

The exchange interaction can be described as a quantum mechanical effect among identical particles due to the wave function of the particles. Exchange symmetry (either symmetric or antisymmetric) affects the interaction between the wave function of particles [41-42]. Exchange interactions among magnetic moments lead to a ferromagnetic or antiferromagnetic arrangement [27], [43-44]. Some of the exchange interactions are summarized below.

1.3.1.1 Direct exchange

If the wave functions of two particles are sufficiently overlapped, then direct exchange interaction comes in the picture and gives a short but strong coupling that diminishes once ions are separated. Since "Coulomb interaction" is nominal whenever the atoms are close, then the electrons stay mostly in between the nuclei. This small interatomic distance gives an antiparallel alignment or "negative exchange (antiferromagnetism)" as following Fig. 1.4.



Figure 1.4. "Antiparallel alignment" for small interatomic distances.

The electrons stay mostly far from one another to keep down the "electron-electron repulsion" when the atoms are far away. Therefore, it causes a parallel alignment or "positive exchange (ferromagnetism)" as following Fig. 1.5.



Figure 1.5. "Parallel alignment" for large interatomic distances.

In direct interatomic exchange, "exchange coupling constant (j)" might be (+)ve or (-)ve relying upon the "Coulomb energy" and "Kinetic energies".

1.3.1.2 Double exchange

Zener (1951) proposed a direct exchange mechanism for interaction among the nearest ions of parallel spin through an O-ion. Double exchange arises among the ions possessing different valence states but belongs to the same metal. For the 180° bond angle in "Mn-O-Mn", then the interaction of "eg orbitals" of Mn with "2p orbitals" of O provides more electrons to one Mn ion than the other as demonstrated in Fig. 1.6.

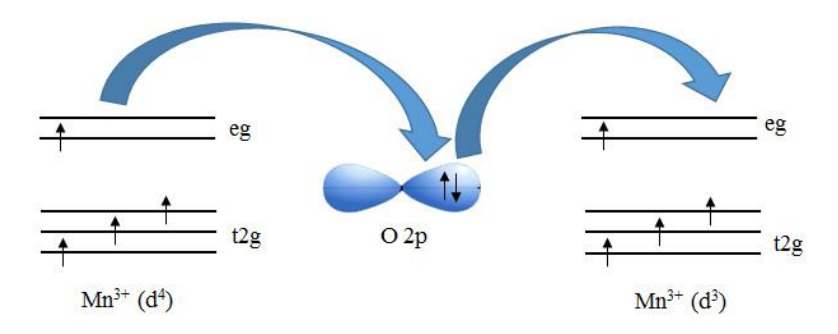


Figure 1.6. Double exchange in Mn-ions from d-orbitals.

1.3.1.3 Indirect Exchange

In the case of metal or semiconductor, indirect exchange interaction is prominent. In these materials, the interaction between two paramagnetic ions/atoms happens indirectly with the mediation of free electron of electron clouds (conduction electron). Therefore, this kind of interaction is named as an "indirect exchange interaction".

1.3.1.4 Super exchange

The "superexchange interaction" is an "indirect exchange interaction" that takes place among the magnetic ions via the nonmagnetic ion placed in between them. Despite the non-overlapping wave-functions of magnetic ions, they can interact with the help of nonmagnetic ion and show appreciable spontaneous magnetization [36], [40].

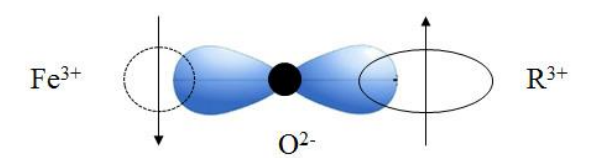


Figure 1.7. Example of superexchange interaction.

Fig. 1.7 demonstrates the coupling among the moments of the metal-cations part by "diatomic-anion". Fe³⁺ has spherical symmetry, whereas rare-earth ion (R) is asymmetric with strong spin-orbit coupling. The moment of both the ions is coupled via the superexchange. Therefore alteration in Fe moment changes the overlapping of the R cation.

1.3.1.5 Itinerant Exchange

Non-localized electrons that are shared by the entire system can have interaction among themselves. This electron-electron interaction is termed as an "itinerant exchange interaction".

1.3.2 Magnetic anisotropy

The energy difference among two magnetization directions w.r.t. the crystallographic axis is called "magnetic anisotropy". The energy difference within the easy and hard axis of magnetization gives rise to different kinds of magnetic anisotropies, such as magnetocrystalline anisotropy, shape anisotropy, growth-induced anisotropy and stress-induced anisotropy. These anisotropies depend on sample shape, crystal structure and atomic or micro-scale texture [45-46]. Also, the anisotropy depends on temperature and must tend to zero at T_C if there is no applied field.

1.3.2.1 Magnetocrystalline anisotropy

The energy required for changing the direction of magnetization from easy to the hard axis is called magnetocrystalline energy [47]. A material can have one or more easy direction of magnetization. Based on the number of easy axes, the material can fall under the category of uniaxial and cubic anisotropy. The material can be divided into two categories depending on the energy required for magnetization of the material as follows:

- (A) **Isotropic:** If same amount of energy is required for magnetization along the easy and hard axis, then the material falls under the category of isotropic.
- **(B) Anisotropic:** The easy and hard axis differ from each other in terms of free energy in an anisotropic material.

For crystals of "cubic symmetry", the "anisotropy energy" is described in terms of the "direction cosines (α_1 , α_2 , α_3)" of the internal magnetization along the three cube edges [48] as follows;

$$E_a = K_1(\alpha_1^2 \alpha_2^2 + \alpha_2^2 \alpha_3^2 + \alpha_3^2 \alpha_1^2) + K_2 \alpha_1^2 \alpha_2^2 \alpha_3^2 + \dots (1.1)$$

Here, K_1 and K_2 represent "first- and second-order temperature-dependent magnetocrystalline anisotropy constants", respectively. " $\alpha_1 = \cos \alpha$ ", " $\alpha_2 = \cos \beta$ ", " $\alpha_3 = \cos \gamma$ ", and α , β , γ are the "angles between the magnetization and the three

crystal axes (easy axis)". The unit of K_i is "Jm⁻³", and the unit of E_a is "energy per unit volume". This anisotropy is termed as "cubic anisotropy".

For "hexagonal symmetry", anisotropy energy is written as [48]

$$E_a = K_1 \sin^2 \theta + K_2 \sin^4 \theta + \dots = \sum K_n \sin^{2n} \theta$$
 (1.2)

Here, θ is "angle between the magnetization and c-axis (easy-axis)". This anisotropy is termed as "uniaxial anisotropy" [48].

1.3.2.2 Shape anisotropy

The "shape anisotropy" occurs in ferromagnetic/ferrimagnetic materials with high intrinsic susceptibility and low degree of magneto-crystalline anisotropy [49]. In larger particles, "shape anisotropy" is insignificant than the "magneto-crystalline anisotropy". The shape anisotropy does not exist for an exact spherical sample. However, for a nonspherical sample, magnetization is easy in the long axis because of the smaller demagnetization field along the axis [50]. This anisotropy mostly exists in the films due to non-spherical grains. In thin-film grains may have an ellipsoidal shape (prolate or oblate type), leading to in-plane alignments of magnetic dipoles. The shape anisotropy energy is given by,

$$E = \frac{1}{2}\mu_0 M_s^2 \cos^2 \theta \tag{1.3}$$

Here, M_s is "saturation magnetization" and θ is "angle between magnetization and plane normal".

1.3.2.3 Surface anisotropy

Surface effects are the main contributor to the anisotropy of nanosize magnetic particles. Symmetry breaking and reduction of the nearest neighbor coordination creates surface anisotropy in the system.

The "Effective magnetic anisotropy" for the thin film is expressed as a sum of volume and surface terms [Johnson 1996]:

$$K_{\text{eff}} = K_{v} + \frac{2}{t}K_{s} \tag{1.4}$$

Here, t denotes "thickness of the film", K_s denotes "surface contribution", and K_v represents "volume contribution". The above equation consists of "magnetocrystalline", "magnetostriction" and "shape anisotropy" terms.

For small spherical particles of diameter d, the "effective magnetic anisotropy" is described as

$$K_{\text{eff}} = K_v + \frac{s}{v}K_s = K_v + \frac{6}{d}K_s$$
 (1.5)
Here, $S = \pi d^2$ and $V = \frac{1}{6}\pi d^3$

Here, S and V are "surfaces and volume of the particle", respectively.

1.3.2.4 Growth-induced anisotropy

The growth-induced anisotropy arises from the conditions during the growth process. In this case, a certain ordering of the respective ions takes place along the growth directions, which leads to a uniaxial growth-induced anisotropy [48]. For polycrystalline specimens, the induced anisotropy energy is,

$$E = K_u \sin^2(\theta - \theta_u) \tag{1.6}$$

Here, K_u represents "induced anisotropy constant" and $(\theta-\theta_u)$ is "angle of the measuring field (θ) relative to the induced field (θ_u) ".

1.3.2.5 Stress-induced anisotropy

This anisotropy is created by external factors such as stress-induced in the system. The influence of the stress or strain also affects the preferred directions of magnetization due to the "magnetoelastic interactions". The strain of the system alters "magnetocrystalline anisotropy" and, therefore, alters the magnetization direction. This effect is opposite to the "magnetostriction". In the case of magnetostriction, sample dimensions vary on the alteration of magnetization direction [51-52].

Energy linked up with "stress-induced anisotropy" is proportional to the applied stress and the magnetic dipole's orientation. The energy density per unit volume is given by [52];

$$E = \frac{3}{2}\lambda\sigma\sin^2\theta\tag{1.7}$$

Here, λ is "magnetostrictive constant" which depends on the orientation of dipoles, σ represents "applied stress" and θ denotes "angle between the magnetization and applied stress".

1.4 Applications of ferrimagnetic-ferroelectric Composite

Multiferroics consists of more than one ferroic order such that "electric, magnetic and elastic behavior" simultaneously [53]. The simultaneous existence of ferroelectricity and magnetic ordering in multiferroic materials are gaining special interest due to their promising applications in various multifunctional devices [54-61]. There are two types of magnetoelectric (ME) multiferroic materials; single-phase and composite. Generally, the ME effect in the single-phase multiferroic appears at low temperature and contains relatively weak magnetoelectric coupling, which limits their practical applications [62]. On the other hand, the composite multiferroics consist of ferrimagnetic (magnetostrictive property) and ferroelectric (piezoelectric property) phase at room temperature. These composites show the parent as well as their coupling material properties. Neither the magnetic nor the ferroelectric phase has the ME effect, but the composites exhibit a remarkable ME effect than that of single-phase compounds. Also, the composites are important for the advancement of various applications including four-state logic memory devices, magnetoelectronic devices, magnetoelectric sensors, magnetoelectric random access memory, etc. [63-65]. During the past decade, several multiferroic composite materials were studied including Ni(Co, Mn)Fe₂O₄–BaTiO₃ [66], CoFe₂O₄–BaTiO₃ [67], NiFe₂O₄–BaTiO₃ [68], Ni(Co, Mn)Fe₂O₄–PZT [69], etc. and found coupling between ferrimagnetic and electric degrees of freedom with remarkable properties.

In recent years, researchers are looking forward to obtaining multiferroics with good magnetoelectric (ME) effect. Usually, the ME coupling mechanisms take place due to strain mediated coupling, exchange interaction mediated mechanisms and charge coupling (interfacial electronic reconstruction) [70]. In order to get higher magnetoelectric coupling: high magnetostriction, good piezoelectric coefficient and strong mechanical interaction between the phases are required [56], [67]. Therefore, for the preparation of the multiferroic composite, we have chosen Mn-Zn ferrite as a ferrimagnetic component and BaTiO₃ as a ferroelectric component [71-73].

1.5 Structure of Barium titanate (BaTiO₃)

BaTiO₃ (BTO) belongs to the perovskites family with formula ABO₃, where A and B cations are of different sizes. BTO is lead-free ferroelectric material with a tetragonal structure at room temperature. Its excellent dielectric, ferroelectric and piezoelectric properties make BTO an efficient candidate for various applications [73-74]. In BTO, a larger "cation A" forms fcc lattice with "oxygen", whereas the smaller "cation B" takes "octahedral interstitial sites", therefore, oxygen becomes the nearest neighbor of "cation B" as demonstrated in Fig. 1.8.

BTO shows an abrupt phase transition from paraelectric to ferroelectric when the temperature is increased (Fig 1.9) (i.e., "cubic→ tetragonal → orthorhombic → rhombohedral at transition temperatures") [75-78]. Therefore, BTO offers to explore the lattice strain-mediated magnetoelectric coupling, also known as a magnetoelastic coupling, in the case of composites. In BTO, the ferroelectric transition occurs around 120°C, which is around the peak of permittivity.

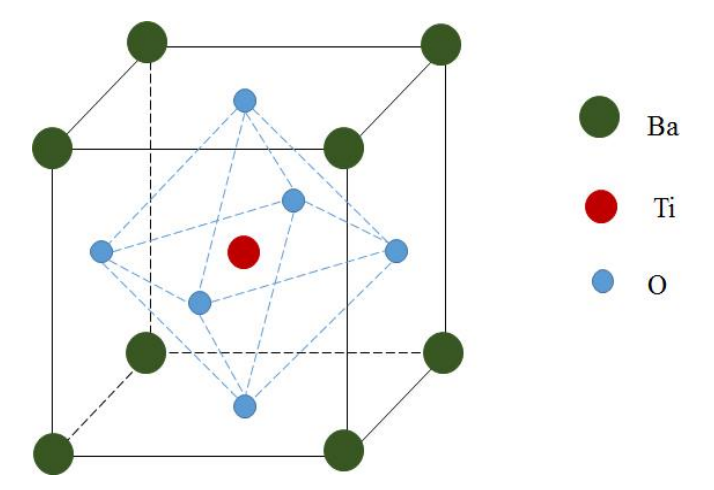


Figure 1.8. Schematic drawing of the perovskite structured BTO unit cell.

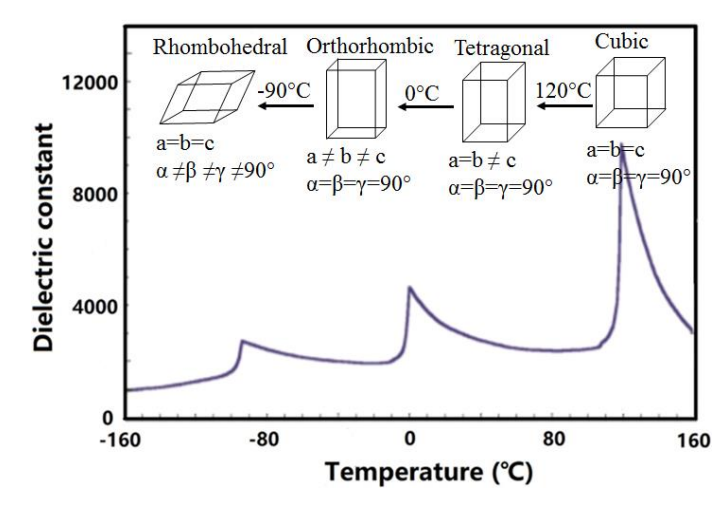


Figure 1.9. The "dielectric constant" of BTO as a function of temperature [77].

1.6 Aim

Magnetic nanoparticles, thin films, and ferrimagnetic-ferroelectric composites have several applications. The study of such systems is quite interesting and challenging to find improved characteristics in research and development. The present work is aspired to control the magnetism in nano polycrystalline and thin films of ferrite by controlling the particle size, composition, and film thickness, respectively. The study of ferrite as nanoparticles, thin films and composites are very interesting from the applied and fundamental point of view. Further to realize the ferrite as a magnetic component in a composite multiferroic, the present work also focuses on the growth, characterization and physical properties of ferrite/BaTiO₃ composites.

Therefore, the present thesis has been presented in three aspects: (i) ferrite nanoparticles, (ii) ferrite thin films and (iii) ferrite and BaTiO₃ composite ceramics.

1.7 Objective of the present study

The present work is focussed on the synthesis and study of Zn(Mn) ferrite nanoparticles, thin films of Zn(Mn) ferrites and Zn(Mn) ferrite-BaTiO₃ composites. To attain these objectives, the following subsystems were studied;

- "Mn_xZn_{1-x}Fe₂O₄" nanoparticles (x=0, 0.1, 0.2, 0.3, 0.4, 0.5, 0.6, 0.7, 0.8, 0.9, 1.0).
- " $Mn_{0.5}Zn_{0.5}Fe_2O_4$ " (MZF) thin films.
- " $(x)Mn_{0.5}Zn_{0.5}Fe_2O_4 + (1-x) BaTiO_3$ " composites (x = 0.05, 0.10, 0.15, 0.20).

These subsystems were studied according to the following plan of work:

- 1. To synthesize " $Mn_xZn_{1-x}Fe_2O_4$ (x=0 to 1)" (ZMF) nanoparticles via the coprecipitation method.
- 2. To study the structure and morphology of ZMF nanoparticles.
- 3. To study the magnetization behavior of ZMF nanoparticles using dc magnetization and ferromagnetic resonance studies.
- 4. To fabricate the MZF thin films by varying deposition conditions.
- 5. To examine the structure, morphology, and optical behavior of MZF films.
- 6. To understand the magnetization behavior of MZF films using dc magnetization studies.
- 7. To carry out ferromagnetic resonance studies to realize the magnetic interactions exist in the MZF thin-films.
- 8. To synthesize the BTO nanoparticles by hydrothermal method.
- 9. To synthesize the ferrimagnetic-ferroelectric composite of ZMF and BTO.
- 10. To study the structure and morphology of the multiferroic composite.
- 11. To study the magnetic and electrical behavior of the multiferroic composite using dc magnetization, dielectric and PE loop studies.

1.8 Organization of the thesis

The work done during the Ph.D. is compiled in the form of six thesis chapters. The first two chapter includes a basic introduction of the material, their synthesis and characterization techniques, whereas chapter 3, 4, 5 covers the result and discussion about the work done during Ph. D. The main results, conclusions, and future scopes are summarized at the end of the thesis in chapter 6. A summary of each chapter is as follows:

Chapter 1: This chapter deals with the general introduction of ferrite nanoparticles, thin films, and its importance. It also contains information about the material which we have used in the preparation of nanoparticles, thin films, and composites.

Chapter 2: This chapter describes the details of the fabrication method and the experimental techniques used for the study. It includes the preparation method of ZMF and BTO nanoparticles, MZF thin films, and composites. The experimental set up for the study of structural, magnetic, optical and electrical properties is also included.

Chapter 3: This chapter combines the structural and morphological study of the ZMF nanoparticles. DC magnetization and ferromagnetic resonance studies of ZMF nanoparticles explain about the magnetic behavior and interaction present in the nanoparticles.

Chapter 4: This chapter consists of structure, morphology, optical, and magnetization study of the $Mn_{0.5}Zn_{0.5}Fe_2O_4$ thin films deposited under different conditions.

Chapter 5: This chapter includes the structural and morphological study of the multiferroic composites. Magnetic and electrical behavior of multiferroic composites is explained using dc magnetization, dielectric and PE loop studies.

Chapter 6: This chapter provides a summary of the work included in the thesis and main conclusions. The future scopes of the work are also included in the chapter.

References

- 1. M. Pardavi-Horvath, J. Magn. Magn. Mater. 215-216, 171-183 (2000).
- 2. J. D. Adam, L. E. Davis, G. F. Dionne, E. F. Schloemann and S. N. Stitzer, *IEEE Trans. Microwave Theory Tech.* **50**, 721-737 (2002).
- 3. C. Miclea, C. Tanasoiu, C. F. Miclea, A. Gheorghiu and V. Tanasoiu, *J. Magn. Magn. Mater.* **290–291**, 1506-1509 (2005).
- 4. V. G. Harris and et al J. Magn. Magn. Mater. **321**, 2035-2047 (2009).
- 5. D. Stoppels, J. Magn. Magn. Mater. 160, 323–328 (1996).
- 6. M. Sultan and R. Singh, *J. of App. Phys.* **107**, 09A510 (2010).
- 7. G. Thirupathi and R. Singh, *IEEE Trans on magnetics* **48**, no. 11 (2012).
- 8. T. Osaka, *Electrochimica Acta* **45**, 3311-3321 (2000).
- 9. E. Scholoemann, J. Magn. Magn. Mater. 209, 15-20 (2000).
- 10. A. Farheen and R. Singh, *Integrated Ferroelectrics* **193**, 31-35 (2018).
- 11. J. T. Lue, *Physical Properties of Nanomaterials*, In Encyclopedia of Nanoscience and Nanotechnology Edited by H. S. Nalwa, American Scientific Vol. X, 1-46 (2007).
- 12. Q. A. Pankhurst, J. Connolly, S. K. Jones, and J. Dobson, *J. Phys. D: Appl. Phys.* **36**, R167-R181 (2003).
- 13. P. Tartaj, M. del Puerto Morales, S. Veintemillas-Verdaguer, T. Gonzalez-Carreno, and C. J. Serna, *J. Phys. D: Appl. Phys.* **36**, R182-R197 (2003).
- 14. C. Berry and A. S. G. Curtis, J. Phys. D: Appl. Phys. 36, R198-R206 (2003).
- 15. C. Liu, A. J. Rondinone, and Z. J. Zhang, *Pure and applied chemistry* **72**, 37-45 (2000).
- 16. S. Sakurai, S. Sasaki, M. Okube, H. Ohara, and T. Toyoda, *Physica B: Condensed Matter.* **403**, 3589-3595 (2008).
- 17. J. Richardi, *Assemblies of Magnetic Nanoparticles*, In: Nanomaterials and Nanochemistry, Edited by C. Brechignac, P. Houdy and M. Lahmani, Springer-Verlag Berlin Heidelberg (2007).
- 18. M. A. Willard, L. K. Kurihara, E. E. Carpenter, S. Calvin and V. G. Harris, *International Materials Reviews* **49**, 125-170 (2004).
- 19. Y. Suzuki, Annu. Rev. Mater. Res. 31, 265-89 (2001).

- C. V. G. Reddy, S. V. Manorama and V. J. Rao, J. Mater. Sci. Lett. 19, 775-78 (2000).
- 21. I. Zaquine, H. Benazizi and J. C. Mage, J. Appl. Phys. 64, 5822–5824, (1988).
- 22. K. Baberschke, *Investigation of Ultrathin Ferromagnetic Films by Magnetic Resonance* In: Handbook of Magnetism and Advanced Magnetic Materials. Ed. by H. Kronmuller and S. Parkin. vol 3: Novel Techniques for Characterizing and Preparing Samples, John Wiley & Sons (2007).
- 23. Yu-Wei Su, Fabrication and Characterization of Ferrimagnetic Film for RF/Microwave Crosstalk Suppression, MSc in chem. Engineering, Oregon State University (2007).
- 24. K. L. Chopra, *Thin film phenomena*, McGraw-Hill, New York (1969).
- 25. R. F. Soohoo, *Theory and application of ferrites*, Englewood Cliffs, N. J. (1960).
- 26. A. J. B. Fuller, IEE Electromagnetic Waves Series 23, 277 (1987).
- 27. A. Goldman, *Modem Ferrite Technology*, 2nd Ed. Springer, New York (2006).
- 28. B. B. Ghate and A. Goldman, Ferrimagnetic ceramics, In: Materials science and technology, vol 11 "structure and properties of ceramics Ed by M.V. Swain" Ed R.W. Cahn, P Haasen and E.J. Kramer (1994).
- 29. H. Waqas, X. L. Huang, J. Ding, H. M. Fan, Y. W. Ma, T. S. Herng, A. H. Quresh, J. Q. Wei, D. S. Xue, and J. B. Yi, *J. Appl. Phys.* 107, 09A514-09A516 (2010).
- 30. G. Thirupathi and R. Singh, *IEEE transactions on magnetics* **50**, no. 11 (2014).
- 31. J. Smit, Magnetic Properties of Materials, McGraw Hill, New York (1971).
- 32. C. Barcena, A. K. Sra, G. S. Chaubey, C. Khemtong, J. P. Liub, and J. Gao, *Chem. Commun.* **44**, 2224-2226 (2008).
- 33. R. B. Jotania and H. S. Wiraka, *Ferrites and Ceramic Composites*, Trans Tech Publications Limited (2013).
- 34. S. S. Kumbhara, M. A. Mahadika, V. S. Mohite, K. Y. Rajpure and C. H. Bhosalea, *Energy Procedia* **54**, 599-605 (2014).
- 35. K. E. Sickafus, J. M. Wills and N. W. Grimes, *J. Am. Ceram. Soc.* **82**, 3279-3292 (1999).

- 36. B. D. Cullity and C. D. Graham, *Introduction to magnetic materials*, 2nd Ed. IEEE Press. USA (2009).
- 37. M. A. Willard, Y. Nakamura, D. E. Laughlin and M. E. McHenry, *J. Am. Ceram. Soc.* **82**, 3342-3346 (1999).
- 38. J. Smit and H. P. J. Wijn, *Ferrites*, Philips Technical Library, Eindhoven (1959).
- 39. P. Hu, H. Yang, D. Pan, H. Wang, J. Tian, S. Zhang, X. Wang and A. A. Volinsky, *J. Magn. Magn. Mater.* **322**, 173-177 (2010).
- 40. N. A. Spaldin, *Magnetic materials: Fundamentals and device applications*, Cambridge University press, Cambridge (2003).
- 41. P. Mohn, *Magnetism in the solid state an introduction*, Springer, Berlin; New York: (2006).
- 42. R. Sharma, C. Pratima, S. Lamba, and S. Annapoorni, *Pramana J. Phys.* **65**, 739-743 (2005).
- 43. K. J. Standley, *Oxide magnetic materials*, Oxford University Press, London (1962).
- 44. S. Blundell, *Magnetism in condensed matter*, Oxford University Press, London (2001).
- 45. J. M. D. Coey, *Magnetism and magnetic materials*. Cambridge: Cambridge University Press (2010).
- 46. R. Malik, S. Lamba, R. K. Kotnala, and S. Annapoorni, *Eur. Phys. J. B* **74**, 75-80 (2010).
- 47. M. T. Johnson, P. J. H. Bloemen, F. J. A. den Broeder, and J. J. de Vries, *Rep. Prog. Phys.* **59** 1409-1458 (1996).
- 48. P. I. Slick, *Ferrites for non-microwave applications*, In: Handbook of Magnetic Materials, vol. **2**, Ed. by E.P Wohlfarth, North-Holland (1982).
- 49. T. Lay, "*Mantle D'' Layer*" in Encyclopedia of Solid Earth Geophysics, H. K. Gupta, Ed. Springer Netherlands, 851-857 (2011).
- 50. C. M. Sorensen, *Magnetism*, In: Nanoscale materials in chemistry Edited by K. J. Klabunde, Wiley, New York (2001).

- 51. R. Coehoorn, Giant magnetoresistance and magnetic interactions in exchange-biased spin-valves for magnetic sensors in Handbook of Magnetic Materials, vol. **15** Edited by K.H.J. Buschow, Elsevier, North Holland (2003).
- 52. M. Farle, Rep. Prog. Phys. 61, 755-826 (1998).
- 53. W. Eerenstein, N. D. Mathur and J. F. Scott, *Nature* **442**, 759 (2006).
- 54. H. Schmid, Multiferroic magnetoelectrics, *Ferroelectrics* **162**, 317-338 (1994).
- 55. N. A. Spaldin and M. Fiebig, Science 309, 391-392 (2005).
- 56. C. W. Nan, *Phys. Rev. B* **50**, 6082-6088 (1994).
- 57. J. V. Suchtelen, Philips Res. Repts. 27, 28-37 (1972).
- 58. M. Liu and N.X. Sun, *Phil. Trans. R. Soc. A* 372, 20120439 (2014).
- 59. S. W. Cheong and M. Mostovoy, *Nature Materials* **6**, 12-20 (2007).
- 60. T. Kimura, T. Goto, H. Shintani, K. Ishizaka, T. Arima and Y. Tokura, *Nature* **426**, 55-58 (2003).
- 61. C. W. Nan, M. I. Bichurin, S. Dong, D. Viehland and G. Srinivasan, *J. Appl. Phys.* **103**, 031101 (2008).
- 62. N. A. Hill, J. Phys. Chem. B 104 (2000).
- 63. N. Ortega, A. Kumar, J. F. Scott and R. Katiyar, *J. Phys.; Condens. Matter* **27**, 23 (2005).
- 64. M. Fiebig, J. Phys. D; Appl. Phys. 38, R123-R152 (2005).
- 65. J. Ryu, S. Priya, K. Uchino and H. E. Kim, *J. Electroceramics* **8**, 107-119 (2002).
- 66. J. V. Boomgaard, R. A. J. Born, J. Mater. Sci. 13, 1538-1548 (1978).
- 67. J. Nie, G. Xu, Y. Yang and C. Cheng, *Mater. Chem. Phys.* **115**, 400-403 (2009).
- 68. R. F. Zhang, C. Y. Deng, L. Ren, Z. Li and J. P. Zhou, *Mater. Res. Bull.* 48, 4100-4104 (2013).
- 69. J. Zhai, N. Cai, Z. Shi, Y. Lin and C. W. Nan, *J. Phys. D: Appl. Phys.* **37**, 823-827 (2004).
- 70. C. Liu, W. Wan, S. Gong, H. Zhang and W. Guo, *Scientific reports* **3856** (2017).

- 71. J. P. Zhou, L. Lv, Q. Liu, Y. X. Zhang and P. Liu, *Sci. Technol. Adv. Mater.* **13**, 12 (2012).
- 72. A. Farheen, T. Gadipelly and R. Singh, Ferroelectrics 516, 1-8 (2017).
- 73. A. Farheen, T. Gadipelly and R. Singh, *AIP Conf. Proceed.* **1832**, 040019 (2017).
- 74. J. C. Burfoot and G.W. Taylor, *Polar Dielectrics and Their Applications*, Berkely: Uni. Calif. Press **20** (1979).
- 75. H. F. Kay and P. Vousden, *Philos. Mag.* **40**, 1019 (1949).
- 76. R. G. Rhodes, Acta Crystallogr. 4, 105 (1951).
- 77. W. J. Merz, *Phys. Rev.* **76**, 1221 -1225 (1949).
- 78. P. W. Forsbergh, *Phys. Rev.* **76**, 1187 -1201 (1949).

Chapter 2

Preparation and characterization techniques

This chapter combines the details of the preparation method of Mn-Zn ferrite (ZMF) nanoparticles, BaTiO₃ nanoparticles, thin films and bulk composites. Various experimental techniques to study the structural, morphological, magnetic, optical and electrical properties of the prepared samples are also described in this chapter.

2.1 Material Preparation methods

Spinel ferrite nanoparticles have stimulated scientific and technological interest among all the magnetic materials due to their promising industrial and biological applications [1]. The surface-to-volume ratio increases with the decreasing size of the nanoparticle. Due to the large surface-to-volume ratio and finite-size effect, ferrite nanoparticles are getting much interest than their bulk counterpart [2]. For the nanocrystalline ferrite, the saturation magnetization decreases due to the increase in surface spin effect (dead or inactive surface layer) compared to their bulk counterpart. The enhanced surface spins in smaller particles lead to the canted or spin-glass like behavior [3]. Moreover, the preparation method strongly influences the chemical, structural, electrical and magnetic properties of the materials. A perfect preparation method needs to give the required particle size with the narrow distributions, good crystallinity, controlled-shape, and required surface, etc. [4]. Therefore we have used different preparation methods for different materials to get the desired parameters. These include chemical methods (coprecipitation) for ZMF nanoparticles, the hydrothermal method for BTO nanoparticles, the ceramic method for bulk composites, and deposition methods (RF-magnetron sputtering) for nanocrystalline thin film samples.

2.1.1 Synthesis of ferrite nanoparticles

The properties of spinel ferrite material strongly depend on the preparation conditions and techniques. In the case of nano-ferrites, the precursors play a crucial role to get the desired structure [5]. The use of appropriate precursors controls the homogeneity and highly dispersed state of the final product. However, there are various preparation approaches such as sol-gel, co-precipitation, hydrothermal, etc. [3], [5-15]. Among them, the chemical co-precipitation method is a commonly used technique to synthesize the ferrite nanoparticles due to the following reasons:

- 1. Particle size can be easily controlled by varying the reaction parameters such as reaction temperature and pH of the solution.
- 2. Easy to obtain uniform and homogenous spherical nanoparticles.
- 3. Simple, economical and large scale preparation technique.

The co-precipitation method used to prepare ZMF nanoparticles can be understood from Fig. 2.1 [3], [16-17].

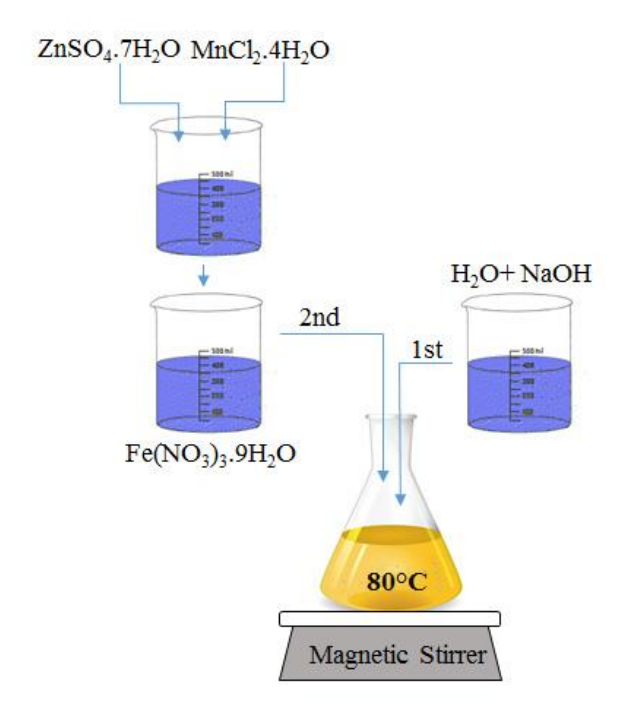


Figure 2.1. Schematic representations of steps to obtain ZMF nanoparticles by coprecipitation method.

Nanoparticles of Mn_xZn_{1-x}Fe₂O₄ (x=0 to 1 with 0.1 step) were prepared via the coprecipitation method [6], [18-22]. The metal salts of Mn²⁺, Zn²⁺, and Fe³⁺ were dissolved in the stoichiometric amount in distilled water. The aqueous solution of these metal salt was mixed and subsequently heated at 90°C. An aqueous NaOH solution was added to the final mixture. "Number of moles (n)" of NaOH controls the "pH of the reaction" which influences the particle size of the ferrites [3]. The following equation governs the chemical reaction involved in the synthesis:

$$xMn^{2+} + (1-x)Zn^{2+} + 2Fe^{3+} + nOH^{-} = Mn_xZn_{1-x}Fe_2O_4 + H_2O$$

The obtained slurry was extensively cleaned with distilled water until the pH reached 7. The final precipitate was dried at 100°C to get the ZMF nanoparticles.

2.1.2 Synthesis of BaTiO₃ (BTO) nanoparticles

There are several procedures have been described by the researcher to obtain nano-powders and nano-materials [23].

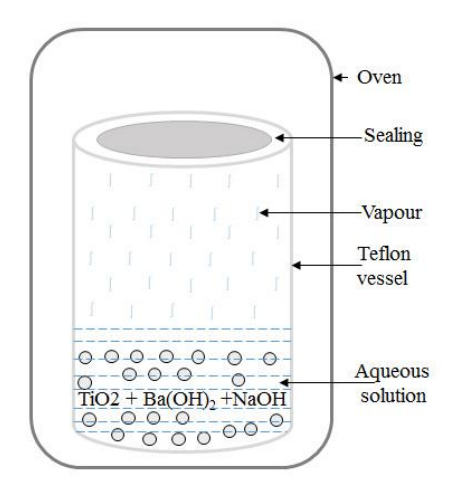


Figure 2.2. Schematic design of an autoclave used for the BTO preparation.

In which hydrothermal procedure has significant advantages like nano-structure, homogeneity, etc. in the synthesis of nanoparticles. Homogeneous grain-growth during the hydrothermal process allows the preparation of materials with desired properties. In the present work, the nanoparticles of BTO were prepared by the hydrothermal method

in an autoclave. The stoichiometric amount of Ba(OH)₂.8H₂O and TiO₂ were dissolved in distilled water and coprecipitated using NaOH. The final solution was heated via the hydrothermal process in an autoclave at 250°C for 12 hours as demonstrated in Fig 2.2. The obtained solution after coprecipitation was almost half filled inside the Teflon vessel with water. The vessel lid is closed tightly with the help of rubber O-ring. This whole set-up was heated inside the oven at approximately 250°C. The heated set-up was cooled to room temperature slowly, and then the pressure was released. The resulting slurry was cleaned with deionized water until the pH reached 7. The final precipitate was dried at 100°C to get the desired BTO particles.

2.1.3 Synhesis of multiferroic bulk composite

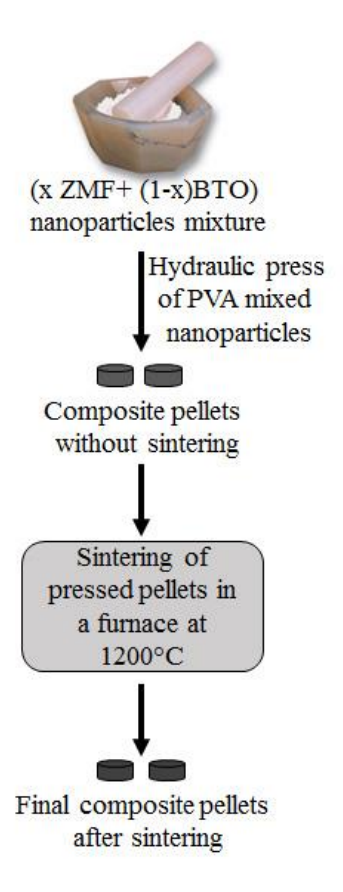


Figure 2.3. Flow chart of the ceramic processing of bulk multiferroic composite samples.

The composites of composition $(1-x)BaTiO_3+(x)Mn_{0.5}Zn_{0.5}Fe_2O_4$ (x=0, 0.05, 0.10, 0.15,0.20 and 1) were synthesized by using the nanoparticles of ZMF and BTO via solid-state route. The nanoparticles of ZMF and BTO were weighed as per the required stoichiometric percentage. Both the nanoparticles were mixed well in "agate mortar and pestle" to yield a homogeneous powder. The approximately 1wt % polyvinyl alcohol (PVA) mixed nanoparticles of ZMF and BTO were ground and pressed into pellets by a "cold uniaxial hydraulic press". Finally, the pressed pellets were sintered in a furnace in an air environment. Initially, the furnace temperature was kept 500°C for 1 hour for complete decomposition of PVA. After this, the furnace temperature was increased to 800°C and maintained it for 2 hours. Further, the temperature was raised to 1000°C for 1 hour. Finally, the furnace temperature was maintained at 1200°C for 6 hours. After this, the furnace temperature was brought to 500°C and switched off to allow the sample to cool. Sintering process controls the structure, microstructure, oxidation state, and physical properties [24] which makes it a most crucial part of the synthesis. Therefore, we have optimized the sintering temperature for composite after so many iterations. Fig. 2.3 shows the flow chart of the ceramic processing of bulk multiferroic composite samples.

2.1.4 Preparation of sputtering target

To obtain Mn_{0.5}Zn_{0.5}Fe₂O₄ (MZF) thin-films via sputtering, we need a two-inch circular target. Therefore, target preparation was done in two steps as follows:

- 1. Synthesis of MZF nanoparticles via co-precipitation method.
- 2. Pressing the PVA mixed MZF nanoparticle powder in the cold hydraulic press followed by sintering at an appropriate temperature.

The sintering of the target is done at high temperature (below the melting point) to fuse the particles to get the dense target. Finally, the MZF target was sintered at 1200°C.

2.1.5 Deposition techniques of thin films

Thin Film deposition can be done by several deposition techniques as shown in Fig. 2.4. Physical vapor deposition techniques follow the below steps:

- Conversion of solid material into ion vapor.
- ❖ Transfer of ion vapor from target to the substrate under pressure.
- Condensation of ion vapor on the substrate of the desired crystal structure.

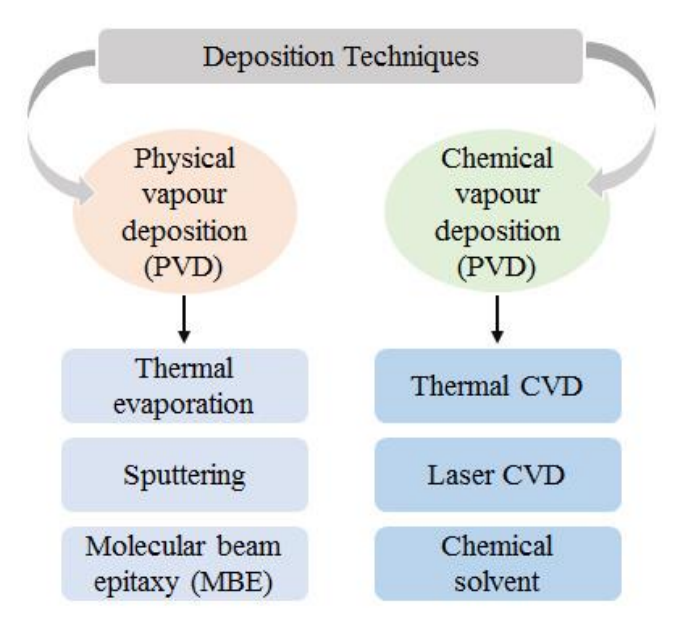


Figure. 2.4. Block diagram of various deposition techniques.

Out of all physical vapor deposition techniques, sputtering was chosen for the deposition of MZF thin films due to the following benefits:

- Controlled deposition rate.
- ➤ Uniformity of film over entire substrate length.
- > Good adhesion of film over the substrate.
- > Reproducibility.
- ➤ Deposition can be done in both reactive and non-reactive mode.

2.1.5.1 Sputtering technique for thin film deposition

Sputtering is one of the physical vapor deposition technique in which the atom of the target material is ejected in the inert gas environment and condensed onto the substrate at a high vacuum to form uniform thin/thick film [25]. Fig 2.5 demonstrates the schematic picture of the sputtering process.

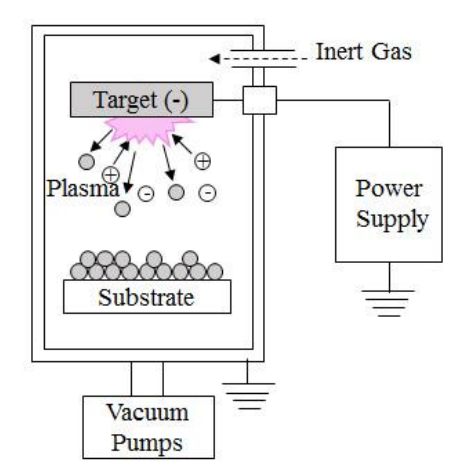


Figure. 2.5. Pictorial presentation of the sputtering procedure.

Operation of sputtering includes the following basic steps:

- 1. Creating a rough vacuum ($\sim 10^{-3}$ Torr) in the chamber using a rotary pump.
- 2. Further, creating a high vacuum ($\sim 10^{-6}$ Torr) in the chamber using a turbo-pump.
- 3. Inclusion of inert gas (e.g. argon (Ar)) or reactive gas (O₂, N₂) into the chamber in a controlled amount.
- 4. Employing DC/RF voltage to the gun cathode to ionize the Ar gas in Ar⁺ and Ar⁻ ions. This procedure generates plasma of different colors depending on the gas used.
- 5. Accelerated Ar⁺ ions collide with the target and extract the target atoms.
- 6. Finally, the target atoms sit on the substrate to grow the film of the target material.
- 7. The Ar⁻ ion goes towards the anode and ionizes further Ar atoms on the way and increases the cycle.

Applied DC/RF voltage, the pressure of the inserted gas and deposition times are the key parameters to get the desired film. These parameters control the nuclear growth, deposition rate and thickness of the film.

2.1.5.2 Specification of the sputtering unit used in the present study

The sputtering system designed by TORR International was used to deposit the thinfilms. The schematic diagram of the sputtering system is shown in Fig. 2.6.

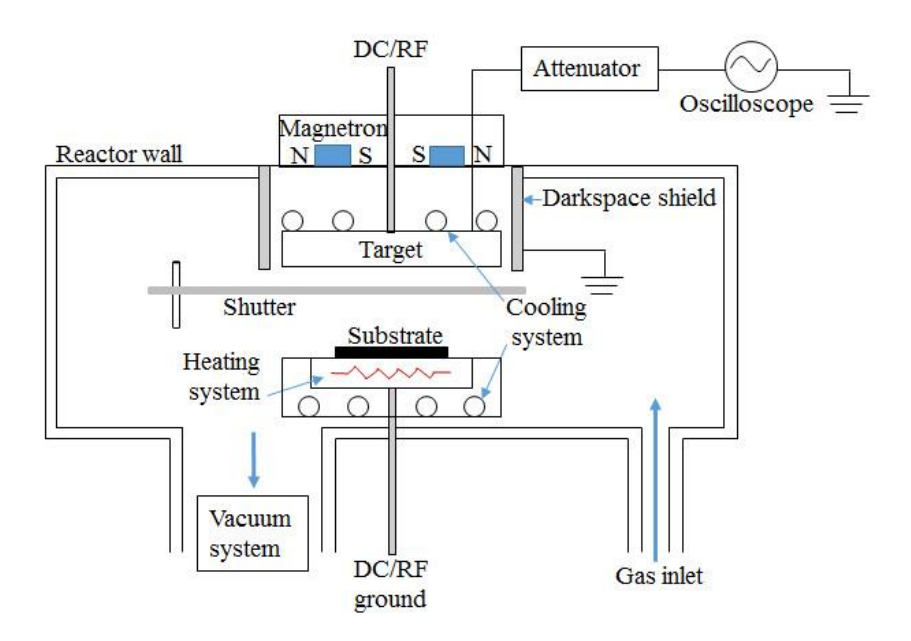


Figure 2.6. Schematic diagram of the magnetron sputtering system [26].

This system contains the following main components [27]:

- > Sputtering chamber
- ➤ Vacuum system
- ➤ RF-Sputtering power supply
- > Target gun assembly
- ➤ Mass flow controller and Pressure Gauge
- > Sample Stage.

In the present study, the ferrite thin films were fabricated via the "RF-magnetron sputtering system" on the thoroughly cleaned 0.5mm thick quartz substrate at room temperature. A two-inch circular polycrystalline Mn_{0.5}Zn_{0.5}Fe₂O₄ (MZF) target was used to obtain the thin films. Three sets of MZF thin were deposited by varying the deposition parameters like applied voltage, gas pressure and deposition time. The distance between the target and substrate was kept 6 cm during all the deposition.

2.2 Characterization techniques

This section includes the working principles of a set of tools used to characterize the synthesized samples. Characterization techniques used to characterize ferrite nanoparticles, thin films, and composites in the study are summarized in Fig. 2.7.

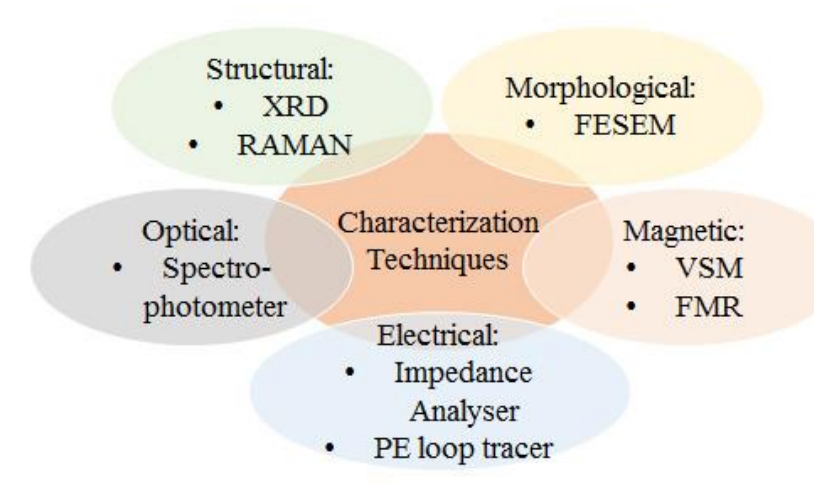


Figure 2.7. Pictorial representation of the characterization techniques used in the present study.

2.2.1 X-ray diffraction

The "X-ray diffraction (XRD)" pattern of the nanoparticles, thin films, and composite samples was recorded with "PANalytical X'Pert³ Powder diffractometer". Cu-Kα source (target) was used in the equipment for producing X-rays. The diffraction pattern can be compared with the standard available data from the "Joint Committee on Powder Diffraction Standards (JCPDS) PCPDF win and National Bureau of Standards".

X-rays are transverse electromagnetic waves with energy ranges from $100\,\text{eV}$ to $10\,\text{MeV}$. It lies on the smaller wavelength side of the electromagnetic spectrum. According to the relation $n=c/v=1/\lambda$, its velocity does not change much when it enters the medium. Hence it shows very less refraction (refractive index slightly less than 1), which makes it suitable for structural characterization of the material. Some general characteristics of X-rays are as follows:

- 1. Due to the high frequency of X-rays, it acts like an energy packet that can easily ionize atoms and rapture bonds in molecules.
- 2. Shorter wavelength than visible light makes it useful to see structures at the atomic level with high resolution in X-ray microscopy.
- 3. X-rays cannot be reflected, refracted, or deflected by an electric or magnetic field as it does not contain the charge.
- 4. The "penetration depth" of X-rays depends on the quality, intensity, and wavelength of the X-ray.

The X-ray diffraction studies mainly done on hard X-rays as it can penetrate deeper without attenuation. It can reveal structural information of the sample. The basic block diagram of the instrument used is demonstrated in Fig. 2.8. It contains three major parts: "X-ray source", "Sample stage", and "X-ray detector".

The monochromatic X-rays penetrates the sample kept on the sample stage. The detector collects the scattered rays after passing across the sample. The intensity of the diffracted beam gives information about the sample structure. The basic structural information can be obtained by JCPDF software. Each intense peak corresponds to the (hkl) plane of the sample according to Bragg's law [28]. The shape of the intense peaks reveals information about crystallite size. The average crystallite size and strain of the samples were estimated using Scherer's formula and Williamson and Hall (W-H) plot [28-29].

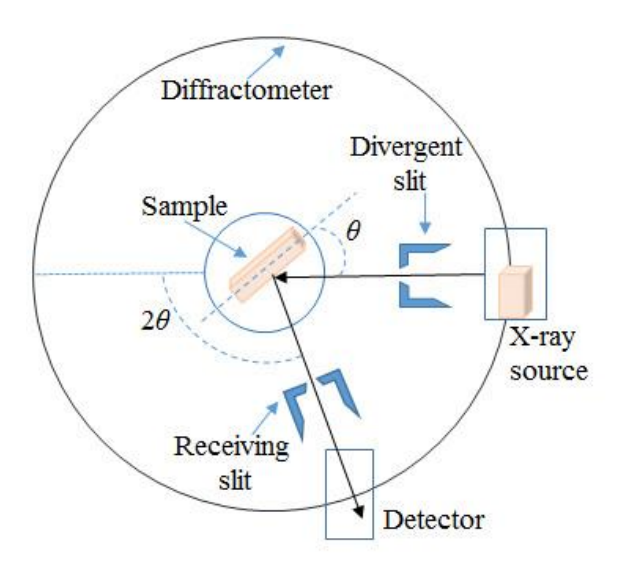


Figure 2.8. Basic block diagram of X-ray diffraction.

Rietveld refinement: Ideally, the shape of the XRD peak should be very sharp, but in real practice, the broadening of shape is observed. The diffraction peaks consist of both Bragg components like size and strain broadening and non-Bragg components like background and instrumental broadening. The refinement of raw XRD data considering both Bragg and non-Bragg component is given by Rietveld and is known as Rietveld refinement [30]. The principle of this method is to minimize the difference between recorded and calculated diffraction patterns. The refinement thus obtained can be used to extract structural information such as phase analysis, crystalline or amorphous nature, lattice parameters, atomic positions, and grain size and temperature vibrations.

The "Rietveld refinement" was executed using the "Full prof suite program" with a "single-phase spinel structure" having "space group Fd-3m" for prepared nanoparticles [31]. The profile used for the fitting is "Thompson-Cox-Hastings pseudo-Voigt convoluted with axial divergence asymmetry function". The crystallite size of the prepared samples was calculated using the "Williamson-Hall" (WH) plot [29], [32-33]. The "FullProf program" was primarily developed for "Rietveld analysis (structure profile refinement) of neutron or powder X-ray diffraction data". However, this can be employed as a "Profile matching tool". We can also do a single-crystal refinement. "PCR file" is the input parameters file for the "FullProf Diffraction profile".

2.2.2 Raman Spectroscopy

"Raman spectroscopy" is a surface-sensitive, nondestructive spectroscopic method which tells about the crystallinity, stoichiometry, and phase transition, etc. Raman spectrum is the fingerprint of the sample and gives detail of the chemical composition. Two phases of the same material cannot have the same Raman spectra; hence they can be easily distinguished. Also, Raman spectra are independent of the frequency of incident light. The intensity of light depends on the number of excited molecules hence gives information about concentration as well. Raman spectroscopy is based on the molecular vibration of monochromatic light (laser light). The major part of the light is of the same frequency as that of the source ("Rayleigh scattering"). A small amount of the scattered light follows a shift in frequency from source frequency. This shift is due to the vibrational interaction of laser light with the molecule. A plot of shifted light intensity with the frequency of the source light gives Raman spectrum. The shifted frequency can be on either side of the Rayleigh frequency. The lower frequency-shifted lines are strokes lines and higher frequency-shifted lines are anti-strokes lines [34]. Fig 2.9 shows the pictorial representation of the Rayleigh line along with strokes and anti-strokes lines.

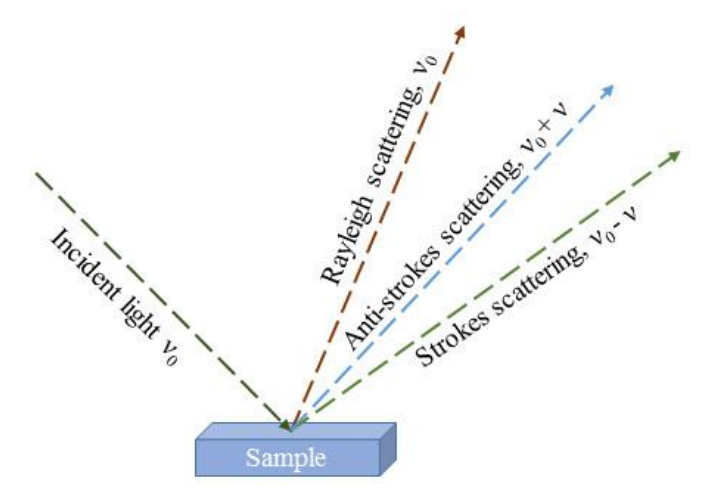


Figure 2.9. Light scattering after laser exposure on a sample surface: Rayleigh line, anti-stroke line, and stroke line.

Advantages of Raman spectroscopy are as follows:

- 1. Sample preparation is not required.
- 2. Nondestructive technique.
- 3. Can be used for solid, liquid or gas sample.
- 4. Short measurement time.
- 5. Analysis of aqueous system.
- 6. Gives quantitative and qualitative information about the sample.

There are three main components of the Raman spectroscopy experimental set-up as shown in Fig 2.10.

Excitation source/Laser: The various types of lasers are used as a source for sample excitation. The basic criteria of laser selection are clean and narrow bandwidth laser to obtain stable and sharp Raman peaks.

Sampling apparatus: The optical microscope or a fiber optic probe is used as a sampling apparatus for focusing the sample.

Detector: The obtained Raman peaks are closely spaced. Therefore, a high-resolution spectrophotometer is used as a detector to distinguish the Raman shift clearly.

The intense peak in the spectrum gives information about vibrational modes of molecules in the sample. The peak fitting of the spectrum can be done using Lorentzian/ Gaussian function to extract the analytical information. The broadness of peak, the height of the peak, and position of peak give important information about the sample. In the case of thin films, a comparison of peak position with bulk gives information about the tensile/compressive strain of the film.

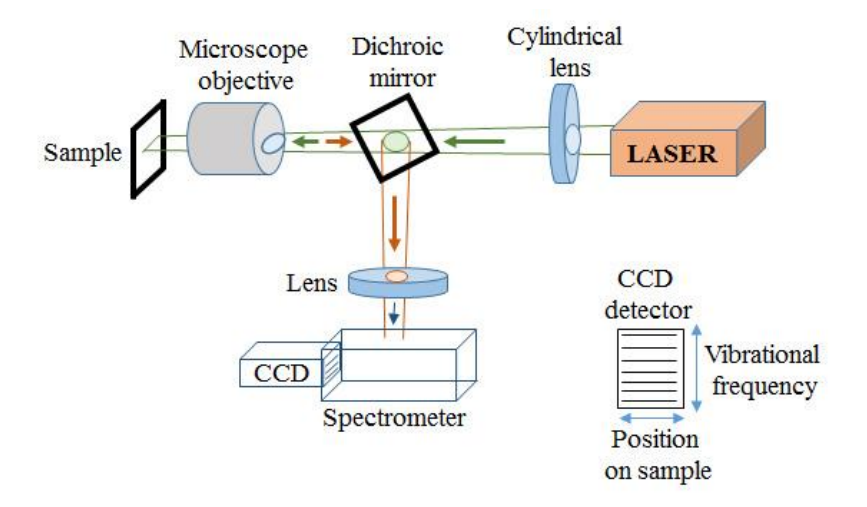


Figure 2.10. Basic assembly of Raman spectrometer.

Raman back-scattering spectra were recorded via "Alpha 300 Witec-Germany Raman spectrometer" with "Nd-YAG laser at 532 nm wavelength".

2.2.3 Field Emission Electron Microscopy

The "Field Emission Electron Microscopy (FESEM)" is useful to understand the morphology of samples and for analyzing the new nanomaterials [35]. The basic principle describes that the beam of high energy electrons is accelerated in a high electric field and focused by electronic lenses in a narrow beam, which bombards the atoms of the sample resulting in the generation of "secondary electrons", "back-scattered electrons (BSE)", "X-rays", light, specimen current, and "transmitted electrons".

Depending on the type of electrons collected and detectors, FESEM can be used in the following three ways:

(a) Imaging: In this case, the secondary generated electrons (SE) are collected by the detector to produce an electronic signal. These signals are then amplified and transformed into an image that can be seen on a monitor (raster image). This imaging can be done with two modes of operation: In lens and SE2.

In lens: In this mode of imaging, the in-lens detector detects secondary electrons generated by primary electrons based on the working distance. The geometry of the

specimen and accelerating voltage limits the working distance, which controls the image clarity.

SE2: In this mode, a special detector is used at the specimen chamber to detect a small component of back-scattered electrons along with the secondary electrons. The working distance is kept at above 4 mm and the specimen is viewed laterally. This mode gives better surface information for some samples.

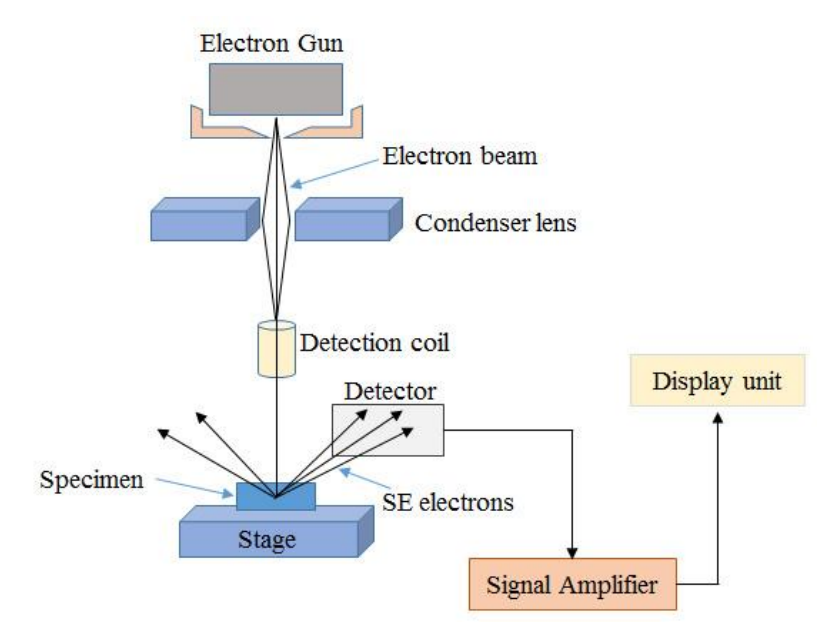


Figure 2.11. Pictorial representation of basic components of FESEM.

(b) Dispersive X-rays: The highly energetic beam (mostly 20 kV) of the electron is used on the sample to knock out inner shell electrons, which leads to the generation of characteristic K_{α} and K_{β} X-rays. These generated X-rays provide information of the elements and composition [36]. These dispersive X-rays are of two types:

EDAX: Energy dispersive X-rays provide details of elemental composition based on the energy generated by X-rays. This technique is used for major elements detection. The number of X-rays generated is related to the number of the element present in the sample. **WDAX:** Wavelength detective X-rays are used to detect the lighter elements present in the sample. It separates the elements based on the wavelength generated and not on

energy. It is a more sensitive technique but causes more destruction to the sample.

(c) The back-scattered electron (BSE) tells about different elements of the sample because the intensity of BSE is a direct measure of the atomic number. Therefore, it is used in elemental analysis than the morphology of the sample.

The block diagram of the set-up used in the study is shown in Fig. 2.11.

The micrographs of nanoparticles, thin films, and composites were recorded using "field emission scanning microscope FESEM, CARL-ZEISS ULTRA 55" in imaging mode. The EDAX mode was used for the element analysis of the samples.

2.2.4 Spectrophotometer

A spectrophotometer amounts to the intensity of light transmitted, reflected, and absorbed after passing through the sample. The amount of light absorbs tells about the optical nature of the sample [37]. The optically active materials having high transmittance in the visible region are useful for photometric devices. Whereas, the highly absorbing materials (high absorbance) can be used to absorb photon energy, which can be to convert to other forms of energy. The high reflectance material gives the "lustrous effect".

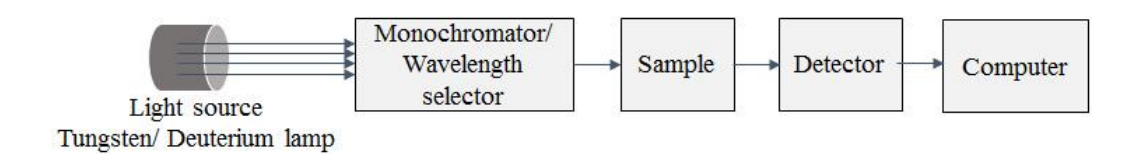


Figure 2.12. Block diagram of basic parts of the UV-Vis-IR spectrophotometer.

Spectrophotometer basic working steps are as follows:

- 1. A light source illuminates the sample.
- 2. Monochromator splits the light into individual wavelength and the adjustable slit allows only the desired wavelength to the sample.
- 3. The sample mounted in the holder is shined by the light of the desired wavelength.
- 4. Finally, the output light is collected and displayed on the screen.

The basic block diagram of the set up used is demonstrated in Fig. 2.12.

The "UV-Vis-NIR spectrophotometer" was used to measure the optical behavior in 190 nm to 2500 nm range of the electromagnetic spectrum. The light source used in this instrument contains two lamps: tungsten lamp for the UV region (190-240 nm) and deuterium lamp in the visible and IR region (240-2500 nm). The spectrophotometer used is a double beam spectrophotometer as it compares the path of the sample with the reference sample.

2.2.5 Vibrating sample magnetometer

The "vibrating sample magnetometer (VSM)" was designed by S. Foner in 1955 [38]. It is a useful instrument to study the sample's magnetic behavior due to its high sensitivity, accuracy, and ease to use. "Faraday's law of electromagnetic induction" is the working principle for VSM. The sample is placed in between the coils of the magnetometer under an external magnetic field. So, the sample magnetizes along the field direction by aligning magnetic domains. The sample magnetization thus increases with an increasing external field. The dipole generated magnetic field produces a "drift field" across the sample. The sample vibrates between the detection coils. Due to the vibration of the sample and drift field, the flux associated with detection coils varies which induces an emf (e) [39] as follows;

$$e = -\frac{d\Phi}{dt}$$

Induced emf is related to the sample's magnetic field. To amplify this little induced "emf", a trans-impedance amplifier and lock-in amplifier are used. The amplified signal is then sent to the computer interface, where suitable software converts it into magnetization value.

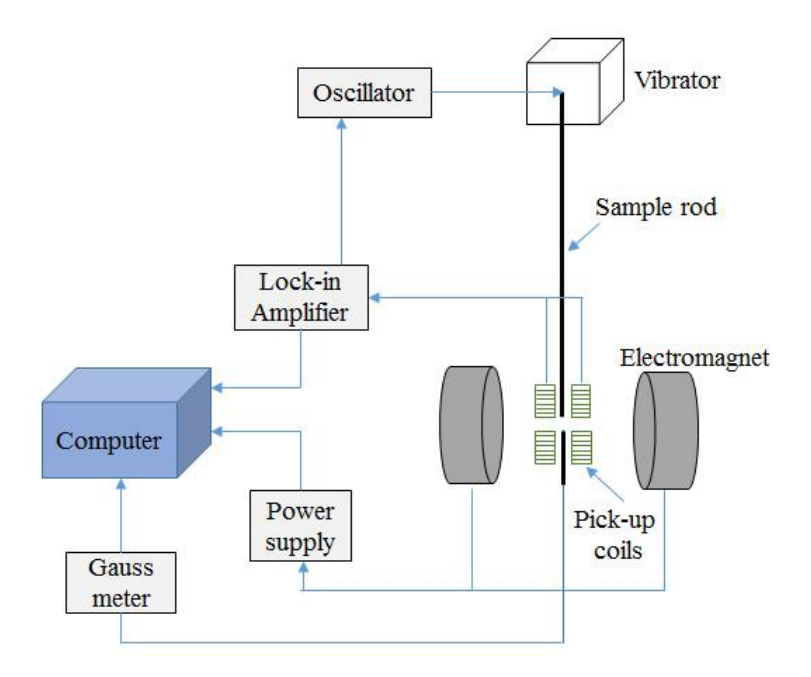


Figure 2.13. Block diagram of the basic components of VSM.

When a magnetic sample is kept in a homogeneous magnetic field, the domains or individual spins align in a particular direction with the field, as a result, the sample gets magnetize. The "Lakeshore design VSM" was used to study the magnetization of the prepared samples. Fig. 2.13 depicts the basic block diagram of VSM.

2.2.6 Ferromagnetic resonance spectroscope

It is the spectroscopic technique which is used to study magnetic behavior of bulk and thin films. The basic principle is based on spin interaction with an external magnetic field in the presence of electromagnetic radiation (in microwave range). The resonance arises when the quantized energy levels of electronic/nuclear moments split in the presence of a uniform magnetic field. The system absorbs energy equivalent to these splited energy levels. This RF induced transition results in absorption spectra as shown in Fig. 2.14. It is first derivative of absorption spectra rather than absorbance spectra which is used for analysis.

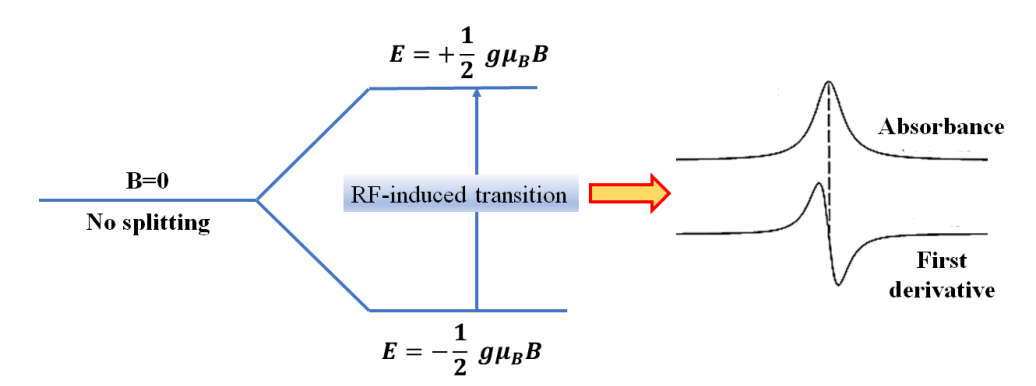


Figure 2.14. Schematic representation of energy level splitting in presence of RF field.

The pictorial representation of RF induced transition is shown in Fig.1.11. The energy associated with this transition is expressed as [64],

$$E = \mu . B = + 1/2g\mu_B B$$

Here, μ_B is Bohr magneton, B is applied magnetic field and g is electron spin g factor. Based on the generated spin, the resonance can be named as electron spin/paramagnetic resonance (ESR/EPR), ferromagnetic resonance (FMR), anti-ferromagnetic resonance (AFMR), spin wave resonance (SWR) and nuclear magnetic resonance (NMR) [65].

The electron spin resonance (ESR)/ferromagnetic resonance (FMR) instrumentation is studied by considering the following parts [40];

- 1. **Radiation source:** The temperature stable Klystron tube circuit arrangement is used as a microwave radiation source. The frequency of the monochromatic source is kept fixed by providing fixed voltage to the circuit through the stabilizer.
- 2. **Waveguide:** The hollow rectangular brass tube is used as a waveguide to pass radiation waves to the sample. The wave-meter is connected in the circuit to measure the frequency of radiation in MHz.
- 3. Sample cavities: The sample is contained in the resonant cavity. The cavity can be rectangular (TE120) or cylindrical (TE011). The magnetic field interacts with the sample in the cavity. So, the position of the sample in the cavity is an important factor. The quality factor Q measures the sensitivity of the spectrophotometer by measuring energy loss in one microwave cycle. The sample is placed in a position where the largest magnetic field can be applied. Thus reduces energy loss and improves the quality factor.

- 4. **Electromagnet:** The stable and uniform magnetic field should pass through the sample. The stability of the magnetic field can be attained by connecting a highly regulated power supply to the electromagnet. The system is connected to a water circulation system to avoid access heat.
- 5. **Detection coils:** The obtained ESR signal after interacting with the field is very weak thus signal amplification is required followed by signal modulation. The modulation is done to carry signal along with the carrier wave. The amplitude modulation is done keeping the frequency and phase the same. These modulation coils are mounted on the cavity wall.

The FMR spectra were recorded via "JEOL JES-FA200 ESR spectrometer at X-band (v = 9.2 GHz)". The basic block diagram of the set-up used in the study is shown in Fig. 2.15.

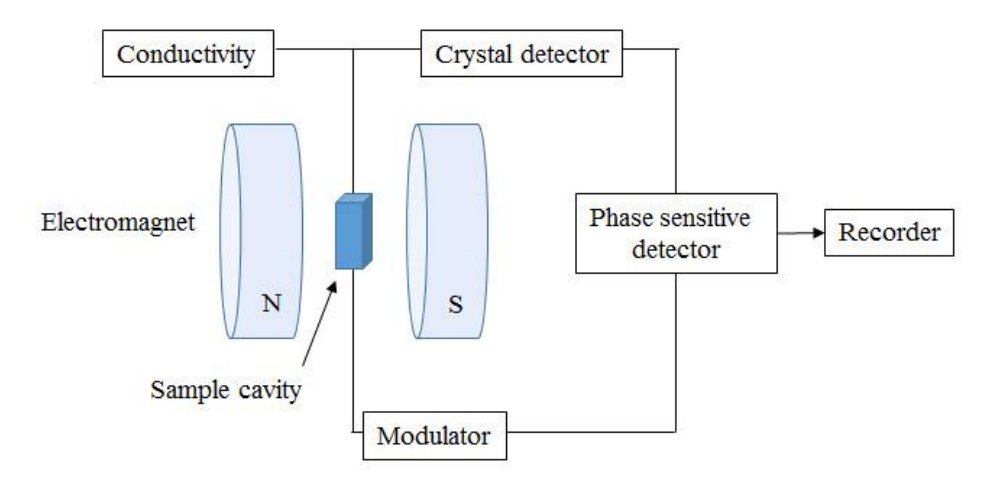


Figure 2.15. Pictorial representation of the basic components of ESR.

2.2.7 Impedance analyzer

Since BaTiO₃ is a constituent of multiferroic composite in the present study, therefore, dielectric properties of the composites were also studied. Dielectric properties of materials are determined by "electrical permittivity (ϵ ')" also known as the "dielectric constant" and the "electrical conductivity (σ)" as following [41-42];

$$\varepsilon' = C_n t / \varepsilon_0 A$$

Here, ε_0 is "permittivity of free space", t denotes "thickness of the sample", and A represents "surface area of the sample" [43].

$$\rho_{AC} = \frac{1}{\varepsilon' \varepsilon_0 \omega tan \delta}$$

In Fig. 2.16, the permittivity is presented as a capacitor (as a parallel plate condenser with the dielectric material). The capacitor is placed parallel to the resistor, the latter presenting the conductivity [44].

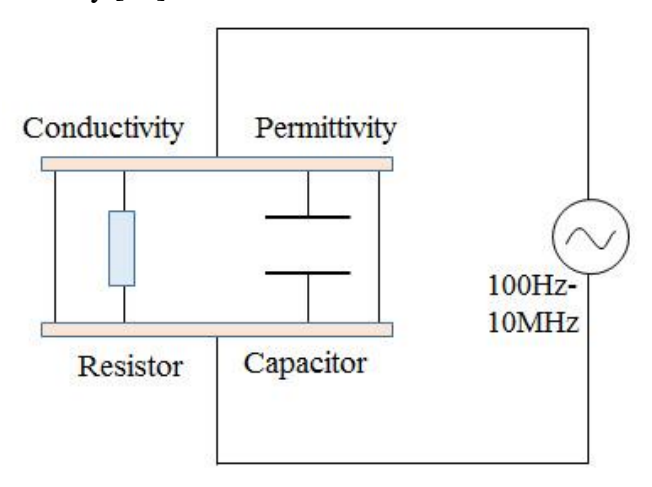


Figure 2.16. Schematic diagram of dielectric measurement setup.

The room temperature relative permittivity study was done using "Impedance analyzer (Agilent E4980A LCR meter)".

2.2.8 P. E. Loop Tracer

Polarization-Electric loop measurement is one of the important techniques to do the electrical characterization of the ferroelectric samples. We can calculate the saturation polarization, coercive electric field, remnant polarization, and leakage current by measuring the "P-E loop". The "P-E loop" is a plot of polarization vs. electric field at fixed frequency [45-47]. Fig. 2.17 shows ideal responses via different P-E loop behavior of simple linear devices.

Working Principle of P-E Loop: This system is based on the "Sawyer Tower circuit" [46] which works according to the principle that if an ac voltage is employed across the capacitors which are attached in series, then both the capacitor will have the same charge. To get the saturation, the "internal capacitance" of the circuit should be greater than the "sample capacitance".

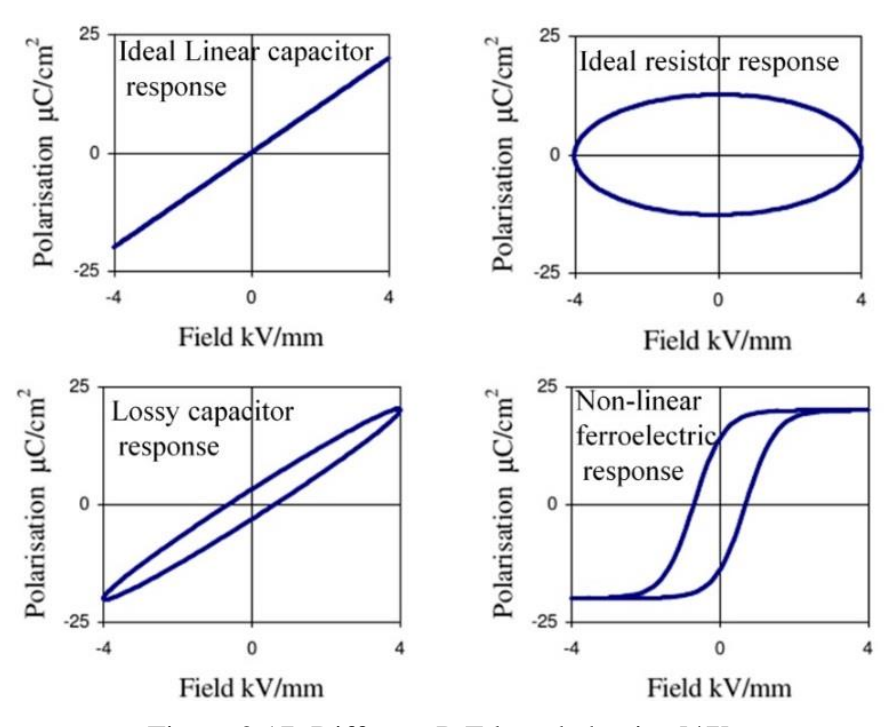


Figure 2.17. Different P-E loop behavior [47].

Fig. 2.18 demonstrates the schematic diagram of the circuit used in the study. The P-E instrument consists of i) main P-E unit including digital oscilloscope, ii) sample holder, iii) temperature controller and iv) desktop (PC) [47].

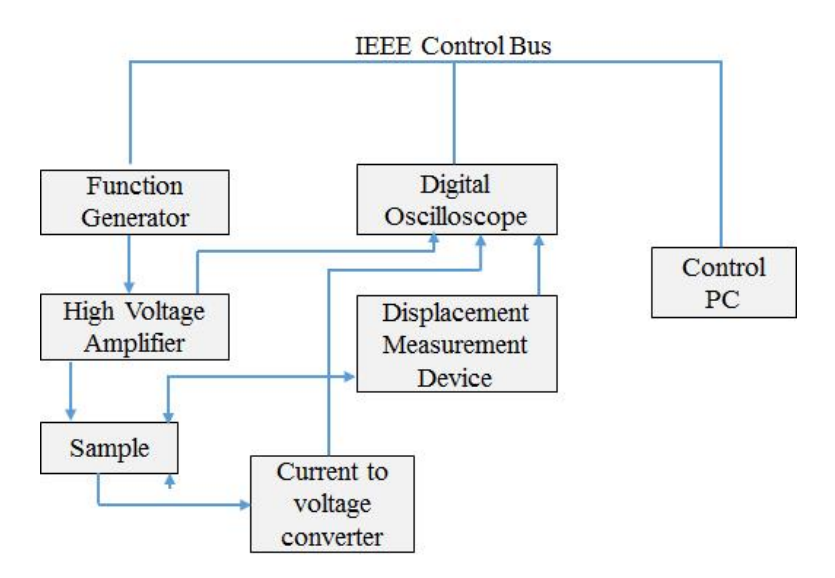


Figure 2.18. Schematic diagram of the P-E loop tracer system [47].

The "Radiant Precision Premier II Analyzer" was used for the P-E loop study of the composites.

References

- Figuerola, R. D. Corato, L. Manna, T. Pellegrino, *Pharmacol. Res.* 62, 1126–1143 (2010).
- 2. R. H. Kodama, J. Magn. Magn. Mater. 200, 359-372 (1999).
- 3. G. Thirupathi and R. Singh, *IEEE trans. on magn.* **48**, 3630-3633 (2012).
- 4. T. Hyeon, Chem. Commun. 927-934 (2003).
- L. Patron, I. Mindru and G. Marinescu, Magnetic Nanomaterials: Nonconventional Synthesis and Chemical Design, In: Dekker Encyclopedia of Nanoscience and Nanotechnology, Marcel Dekker (2004).
- 6. A. Farheen and R. Singh, AIP Conference Proceedings 1953, 120067 (2018).
- 7. Y. Xuan, Q. Li and G. Yang, J. Magn. Magn. Mater. 312, 464–469 (2007).
- 8. K. C. Patil, M. S. Hegd, T. Rattan and S. T. Aruna, *Chemistry of Nanocrystalline Oxide Materials*, World Scientific, Singapore (2008).
- A. H. Lu, E. L. Salabas, and F. Schth, Angew. Chem. Int. Ed 46, 1222-1244 (2007).
- 10. Elkins and K. Eugene, *ProQuest* **69-04** (2008).
- L. Yu, G. Hao, J. Gu, S. Zhou, N. Zhang, and W. Jiang, J. Magn. Magn. Mater.
 394, 14–21 (2015).
- 12. J. H. Yu, D. W. Lee, B. K. Kim, and T. Jang, *J. Magn. Magn. Mater.* **304**, e16–e18 (2006).
- 13. S. Verma, H. S. Potdar, S. K. Date, and P. A. Joy, MRS Online Proceeding Library Archive 818, 83–88 (2004).
- 14. L. B. Tahar, H. Basti, F. Herbst, L. S. Smiri, J. P. Quisefit, N. Yaacoub, J. M. Grenèche, and S. Ammar, *Materials Research Bulletin* **47**, 2590–2598 (2012).
- 15. M. Staruch, D. Hires, D. Violette, D. Navarathne, G. A. Sotzing, and M. Jain, *Integrated Ferroelectrics* **131**, 102–109 (2011).
- 16. Z. Cheng, A. L. K. Tan, Y. Tao, D. Shan, K. E. Ting, and X. J. Yin, *International J. Photoenergy* **2012**, 1-5 (2012).
- 17. G. Thirupathi, S. Saipriya, and R. Singh, AIP Conf. Proc. 1447, 1129 (2012).

- 18. J. Smit and H. P. J. Wijn, *Ferrites*: Physical Properties of Ferrimagnetic Oxides in Relation to Their Technical Applications. Vries, The Netherlands: Philips Tech. Library (1959).
- 19. M. Sertkol, Y. Köseoğlu, A. Baykal, H. Kavas, and A. C. Başaran, *J. Magn. Magn. Mater.* **321**, 157–162 (2009).
- 20. R. J. Joseyphus, A. Narayanasamy, K. Shinoda, B. Jeyadevan, and K. Tohji, *J. Physics and Chemistry of Solids* **67**, 1510–1517 (2006).
- 21. R. M. Freire, T. S. Ribeiro, I. F. Vasconcelos, J. C. Denardin, E. B. Barros, G. Mele, L. Carbone, S. E. Mazzetto, and P. B. A. Fechine, *J. Nanoparticle Research* **15** (2013).
- 22. K. Ali, A. K. Sarfraz, I. M. Mirza, A. Bahadur, S. Iqbal, and A. ul Haq, *Current Applied Physics* **15**, 925–929 (2015).
- 23. B. Jiang, J. Iocozzia and et al, *Chem. Soc. Rev.* **48**, 1194 (2019).
- 24. B. B. Ghate and A. Goldman, *Ferrimagnetic ceramics*, In: Materials science and technology, vol **11** "Structure and properties of ceramics Ed by M.V. Swain" Ed R.W. Cahn, P Haasen and E. J. Kramer (1994).
- 25. M. M. Waite and et al, Sputtering Sources, Rochester, New York Chapter 15 from 50 Years of Vacuum Coating Technology and the growth of the Society of Vacuum Coaters, D. M. Mattox and V. H. Mattox, eds., Society of Vacuum Coaters (2007).
- 26. M. Fanun, *Microemulsions*: Properties and Applications, Taylor & Francis, CRC Press (2009).
- 27. M. Sultan and R. Singh, *J. Physics D: Applied Physics* **42**, 115306 (2009).
- 28. B. D. Cullity and S. R. Stock, *Elements of X-Ray Diffraction*, 3rd Ed., Prentice Hall, New Jersey, USA (2001).
- 29. G. Will, *Powder Diffraction*: The Rietveld Method and Two Stage Method, Springer, Germany (2006).
- 30. H. M. Rietveld, J. Appl. Crystallogr. 2, 65 (1969).
- 31. S. M. Patange, S. E. Shirsath, G. S. Jangam, K. S. Lohar, S. S. Jadhav, and K. M. Jadhav, *J. Applied Physics* **109**, 053909 (2011).

- 32. G. Thirupathi and R. Singh, *IEEE Transactions on Magnetics* **50**, 1–4 (2014).
- 33. D. Varshney, K. Verma, and A. Kumar, *Materials Chemistry and Physics*, vol. **131**, 413–419 (2011).
- 34. J. R. Ferraro, K. Nakamoto, *Introductory Raman Spectroscopy*, Second Edition, Academic press, Amsterdam (1994).
- 35. J. Goldstein, D. Newbury, D. Joy, C. Lyman, P. Echlin, E. Lifshin, L. Sawyer and J. Michael, *Scanning Electron Microscopy and X-Ray Microanalysis*, 3rd. Ed., Plenum Publishers, New York (2003).
- 36. W. Zhou, Z. L. Wang, Scanning Microscopy for Nanotechnology: Techniques and Applications, Springer publication (2006).
- 37. M. W. Jones and K. C. Kao, J. Scientific Instruments (J. Physics E) 2, 331 (1969).
- 38. B. D. Cullity and C. D. Graham, *Introduction to magnetic materials*, 2nd Ed. IEEE Press. USA (2009).
- 39. H. S. Nalwa, *Handbook of Thin Film materials*, Academic press (2002).
- 40. P. H. Rieger, Royal Society of Chemistry (2007).
- 41. K. C. Kao, Dielectric phenomena in solids, Elsevier, USA (2004).
- 42. G. G. Raju, Dielectrics in Electric Fields, Marcel Dekker, New York (2003).
- 43. D. B. Sirdeshmukh, L. Sirdeshmukh and K. G. Subhadra, *Micro- and Macro-Properties of Solids: Thermal, Mechanical and Dielectric Properties*, Springer, New York (2006).
- 44. E. Barsoukov and J. R. Macdonald, *Impedance Spectroscopy*: Theory, Experiment, and Applications 2nd Ed. Wiley, New Jersey (2005).
- 45. Y. Xu, Ferroelectric Materials and Their Applications, North-Holland Elsevier Sci. Publ., Amsterdam (1991).
- 46. C. B. Sawyer and C. H. Tower, *Phys Rev.* **35**, 269 (1930).
- 47. M. Stewart, M. G. Cain and D. A. Hall, Ferroelectric Hysteresis Measurement and Analysis, *NPL Report* CMMT(A) **152**, Teddington, Middlesex, United Kingdom, (1999).

Chapter 3

Structural, morphological and magnetic properties of Mn-Zn ferrite nanoparticles

This chapter combines the detailed study of the Mn-doped Zn ferrite nanoparticles via different characterization.

3.1 Introduction

Nanoparticles of zinc-containing spinel ferrites are extensively used for high frequency and electronic devices as it combines good magnetic, electrical, mechanical and dielectric properties that depend on several factors such as preparation conditions and chemical compositions [1-3]. Manganese-Zinc ferrites (Mn-Zn ferrite) nanoparticles are promising candidates for several technological applications such as choke coil, noise filter, recording-head, and ferrofluid. As well as they are useful for biological applications like hyperthermia, targeted drug delivery and MRI contrast due to their mechanical, chemical and thermal stability [4-9]. The substitution of Mn²⁺ ion in Zn ferrite influences the degree of inversion, magnetic moment and, super-exchange interaction; therefore, Mn²⁺ ions play a crucial role in deciding the magnetic properties [9-10]. The magnetic properties described by the hysteresis loop are highly dependent on both the intrinsic properties of the material (crystal structure and composition) and on extrinsic properties such as grain size and density [7-11].

The polycrystalline " $Mn_xZn_{1-x}Fe_2O_4$ (x=0.0 to 0.1)" (ZMF) nanoparticles were synthesized by co-precipitation as described in second chapter [7], [12-14]. The structure and morphology of all the prepared ZMF nanoparticles were well investigated. The "Fullprof suite program" was used to execute the Rietveld refinements for structural analysis of XRD data. The magnetization measurements of all the samples were carried out at room temperature and low temperature. The FMR study was also done for the prepared samples.

3.2 Structural Study

3.2.1 X-ray diffraction Analysis

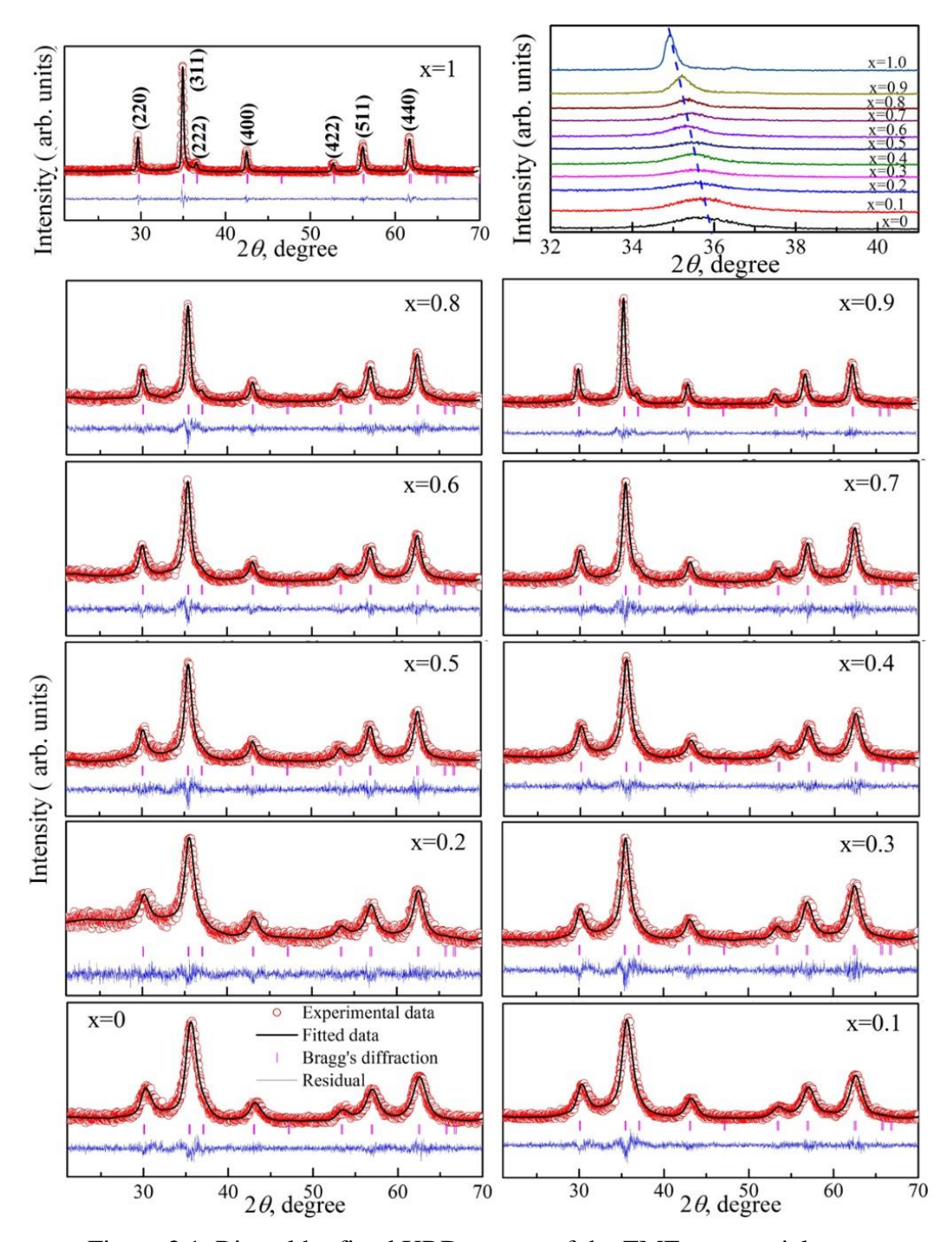


Figure 3.1. Rietveld refined XRD pattern of the ZMF nanoparticles.

Fig. 3.1 depicts the Rietveld refined "X-ray diffraction pattern (XRD)" of the ZMF nanoparticles. The patterns show sharp peaks corresponding to the single-phase "cubic spinel structure" without any detectable impurities. Pure Zn-ferrite in bulk form is normal spinel, but in the case of nanoparticles, it shows a mixed spinel structure [7], [15]. Whereas, pure Mn-ferrite shows an inverse spinel structure. But on substitution of Mn²⁺ in Zn-ferrite, the final product (Mn-Zn ferrite) mostly shows the mixed spinel structure. The shifting of the maximum intense peak towards the lower angle side on increasing Mn-doping evidence the lattice's expansion due to the presence of different strain in the nanocrystalline samples. The surface energy of the nanoparticles increases due to high surface to volume ratio, which creates the uniform and non-uniform strains within the grains.

Further, the detailed structural analysis was done using Rietveld refinement via the Fullprof suite program. The solid black line represents the calculated pattern, and red circles represent the experimental data, while the residual plots (blue color) show the difference between experimental data and calculated pattern. The Rietveld analysis confirms the single-phase cubic spinel structure with the Fd-3m space group [7-10]. X-ray diffraction pattern fits well enough with the "Thompson-Cox-Hastings pseudo-Voigt convoluted with the axial divergence asymmetry function". The "goodness of fit (χ^2)" found from the refinement varied between 1.1- 1.5, which indicates good agreement with the experimental data. The "lattice constant (a)" is extracted from the Rietveld fitting and tabulated in Table 3.1. The crystallite size was calculated using the "Williamson-Hall (W-H) plot".

W-H plot: The XRD peak broadening depends on the following factor: "lattice strain within the sample grain", "instrumental contribution," and the "nature of the sample". Instrumental broadening can be adjusted by taking the peak-widths of the standard (SiO₂) sample. Due to strain involvement, the estimated crystallite size is much bigger than what we get from the Scherrer formula. "Scherrer's formula" modified by "Williamson and Hall" helps to separate the lattice strain broadening contribution from the crystallite size contribution. In other words, we can say that the "Williamson-Hall (W-H)" plot is based on the formula which takes care of both size broadening (β_{size}) and the strain broadening (β_{strain}). Therefore, to estimate the correct size, we have used the W-H plot [16].

$$\beta = \beta_{size} + \beta_{strain}$$

Here, β denotes "full-width half maxima (FWHM)" of the diffraction peaks.

Here,
$$\beta_{size} = \frac{k\lambda}{Lcos\theta}$$
 and $\beta_{strain} = 4\varepsilon \tan\theta$

Size broadening factor varies as $1/\cos\theta$, whereas strain broadening factor varies as $\tan\theta$. Here, ϵ is the "coefficient related to strain", θ is "Bragg's angle", k represents "grain shape factor", and λ denotes "wavelength of Cu-K α radiation".

Their combined effect is determined by a simple sum as follows:

$$\beta = \frac{k\lambda}{L\cos\theta} + 4\varepsilon \tan\theta$$

After multiplying the equation with $\cos\theta$, we get the following formula;

$$\beta \cos\theta = \frac{k\lambda}{L} + 4\varepsilon \sin\theta$$

On comparison with the straight-line equation: y = mx + c

Here we can assume; $x = 4\sin\theta$ and $y = \beta \cos\theta$

$$c (intercept) = \frac{k\lambda}{L}$$
, and $m (slope) = \varepsilon$,

On plotting the curve x vs. y, intercept gives size component, whereas slope is giving strain component. The obtained plot is known as the "Williamson-Hall plot". The "crystallite size" was estimated using the intercept value obtained from a linear fit on the "W-H plot" as depicted in Fig 3.2. Table 3.1 lists the estimated average crystallite size of ZMF nanoparticles.

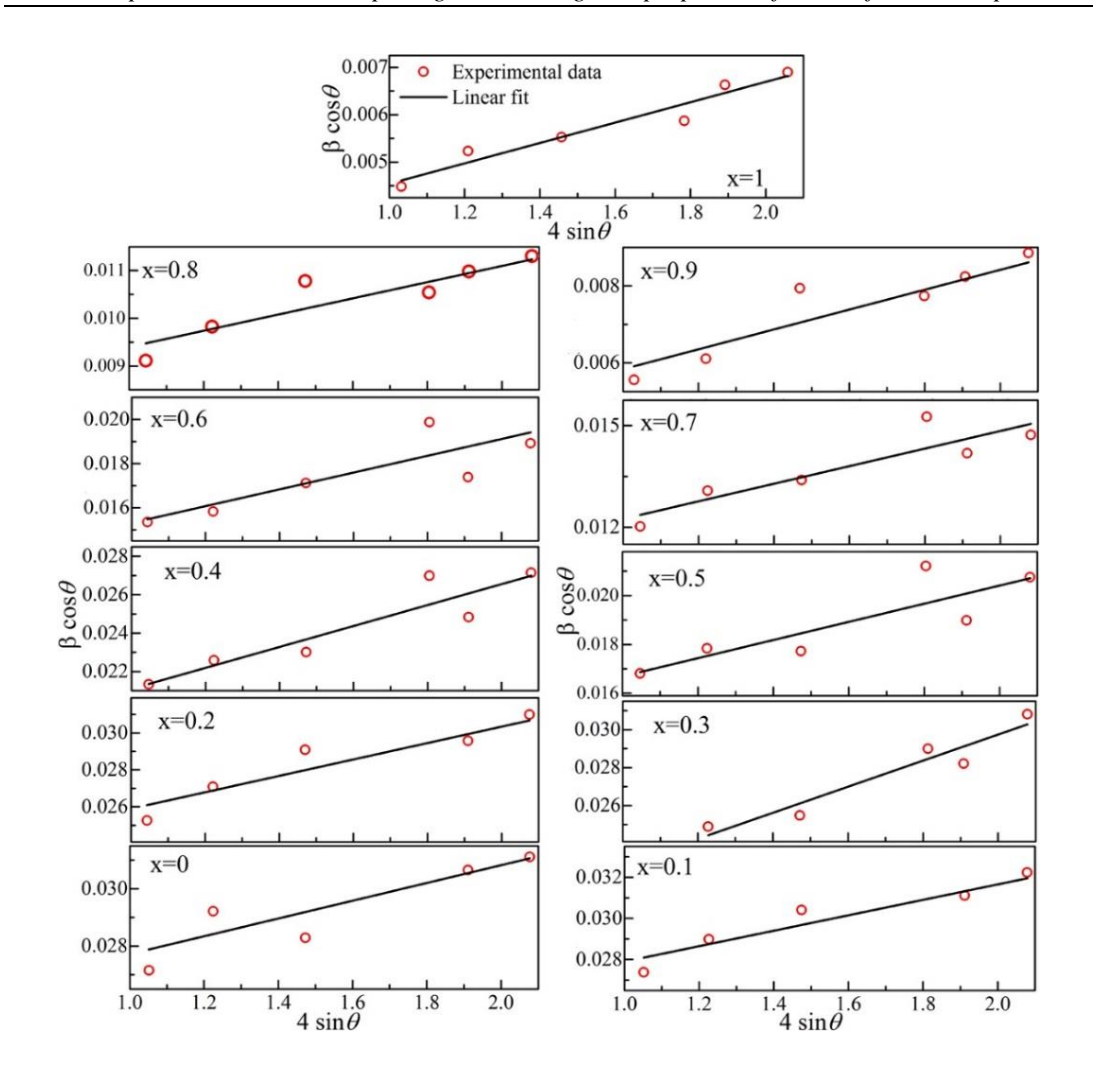


Figure 3.2. "W-H plot" of the ZMF nanoparticles.

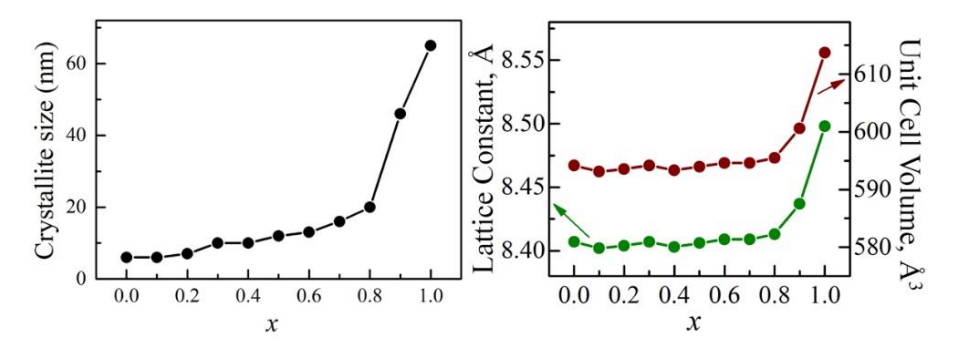


Figure 3.3. Structural parameters vs. x plots of the ZMF nanoparticles.

Since the broadness ("full-width at half maxima") of the XRD peak tells about the size and crystallinity of the samples. Therefore, a decrease in the broadness with Mndoping indicates an increase in the crystallite size on increasing Mn-doping. The compositional dependence of crystallite size, lattice constant (a), and unit-cell volume

is shown in Fig. 3.3. The variation of structural parameters with composition is non-linear. It is observed that the parameters are increasing gradually till x=0.6, and after this composition, parameters start increasing enormously. An increment in lattice constant on increasing Mn concentration is because of the larger ionic size of Mn^{2+} (83 pm) than that of Zn^{2+} (74 pm). Therefore, the expansion of lattice takes place, which leads to an increase in the crystallite size. With the increase in Mn-doping, the fraction of bigger ions become very large compared to the smaller ion, which allows more expansion in the lattice. Therefore, the highly doped samples show a sharp increment in the crystallite size than the less doped samples.

X	Average grain size from	Average crystallite	Lattice	χ^2
	FESEM histogram, (nm)	size from W-H plot,	constant, a	
		(nm)		
0	7	6	8.407	1.02
0.1	8	6	8.402	1.10
0.2	11	7	8.404	1.05
0.3	12	10	8.407	1.13
0.4	14	10	8.403	1.08
0.5	13	12	8.406	1.14
0.6	16	13	8.409	1.03
0.7	18	16	8.409	1.09
0.8	24	20	8.413	1.09
0.9	50	46	8.437	1.41
1.0	68	65	8.498	1.18

Table 3.1. "Structural parameters" of the ZMF nanoparticles.

3.2.2 RAMAN Analysis

Raman spectroscopy is a very sensitive tool that can differentiate into the chemical composition of the sample depending on phonon vibrations. The Raman spectra for the two phases differ from one another depending on the vibrational modes because the vibrational frequencies are specific to the molecule's chemical bonds and symmetry [17]. Fig. 3.4 shows the de-convoluted Raman spectra of all the ZMF nanoparticle samples, respectively. Lorentzian peak function was used to fit peaks to get the peak center value. The solid black line represents the fit, whereas the red circles show experimental data. Phonon modes related to the spinel structure are as follows:

$$A_{1g}(R)$$
, $E_g(R)$, T_{1g} , $3T_{2g}(R)$, $2A_{2u}$, $2E_u$, $4T_{1u}(IR)$ and $2T_{2u}$.

Among them, five phonon modes are Raman active (" $A_{1g}(R)$, E_g (R), $3T_{2g}$ (R)") whereas $4T_{1u}$ and $2T_{2u}$ are infrared (IR) active modes [10], [18-19]. Raman modes above 600 cm⁻¹ infer the modes of the tetrahedral group, which represents the local lattice effect in tetrahedral sublattice, whereas Raman modes below 600 cm⁻¹ infer the modes of the octahedral group which indicates the local lattice effect of the octahedral sublattice. All the samples show three maxima which correspond to the spinel ferrite. Hence, Raman's result also confirms the single-phase cubic spinel structure of the ZMF nanoparticles [17].

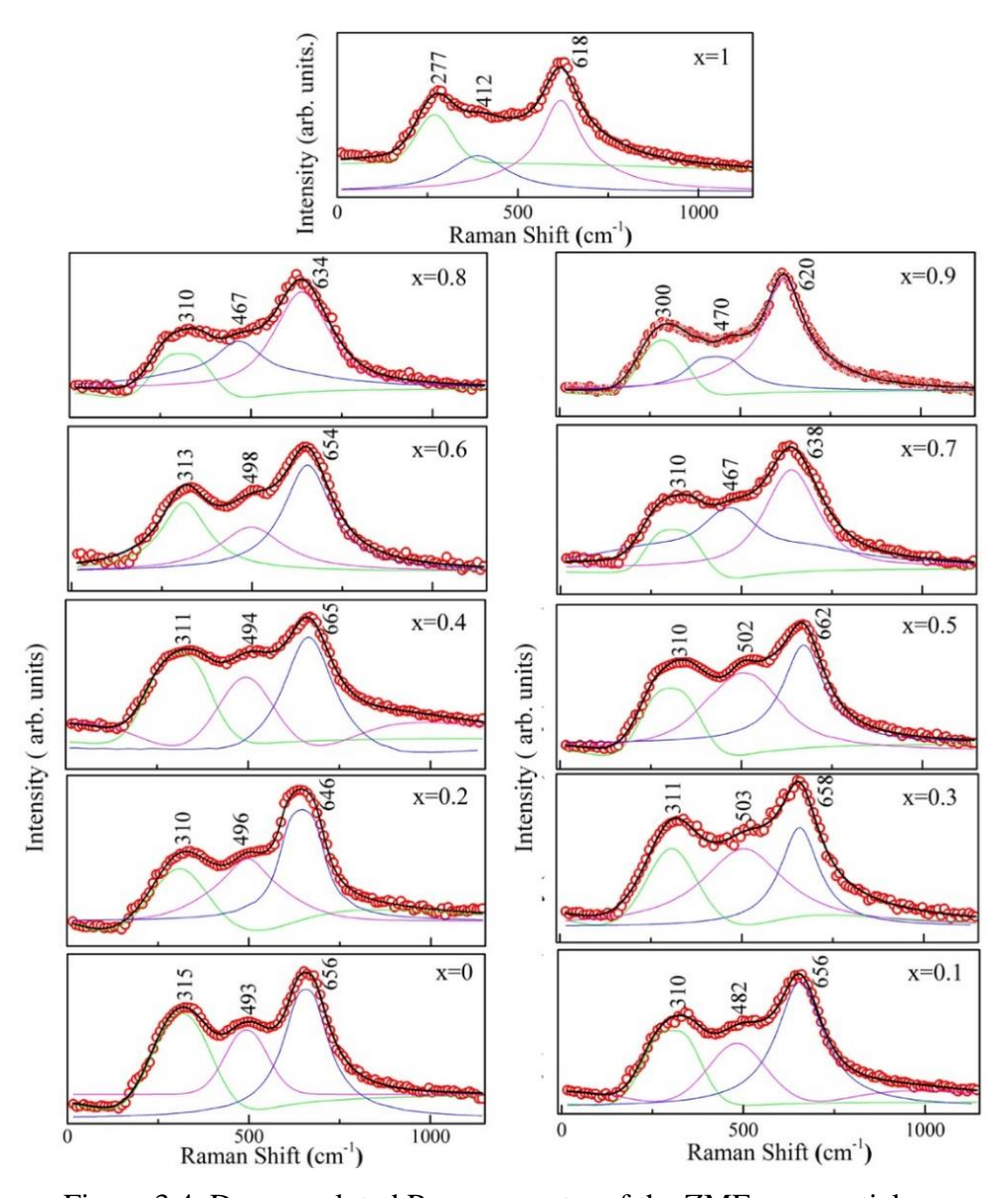


Figure 3.4. De-convoluted Raman spectra of the ZMF nanoparticles.

The variation in the peak values is attributed to the structural disorders present in the Mn-doped nanoparticle system. The Mn substitution alters the cation distribution between octahedral and tetrahedral sites of Zn-ferrite, which causes a change in symmetry of the crystal structure [17-20]. Therefore, an alteration in the vibrational modes takes place with Mn doping in the Zn-ferrite nanoparticles [20]. The increment in crystallite size with increasing Mn-doping indicates an expansion in the lattice, thereby show an increment in the bond length. Since the wavenumber is inversely proportional to the bond-length, therefore the Raman peaks shift towards lower wavelength side with increasing Mn-doping. This shifting of Raman-active modes upon doping of Mn^{+2} is associated with the bigger ionic radius of the Mn^{+2} compare to the Zn^{+2} ion [21]. Thus, the Raman analysis is supporting the conclusion drawn from the XRD analysis.

3.3 Morphological study

The morphological studies of the ZMF nanoparticles were done using FESEM analysis. This technique helps to estimate the average grain size, grain shape, composition and distribution of the prepared ZMF nanoparticles. Fig. 3.5 shows FESEM micrographs of all the ZMF nanoparticles. Spherical grains are observed in the FESEM micrograph. Agglomeration of ZMF nanoparticle is observed due to their magnetic nature [22]. Further, the histogram of particle count (N) is used to realize the "grain size distribution" of the ZMF nanoparticles. The histogram in Fig. 3.5 (inset) demonstrates the "grain size distribution" of nanoparticles and is well fitted with "Gaussian peak function" which indicates an almost narrow distribution of grains [10]. The obtained values of "average grain size" from the fits are tabulated in Table 3.1 and the values are matching with the result obtained from the XRD analysis.

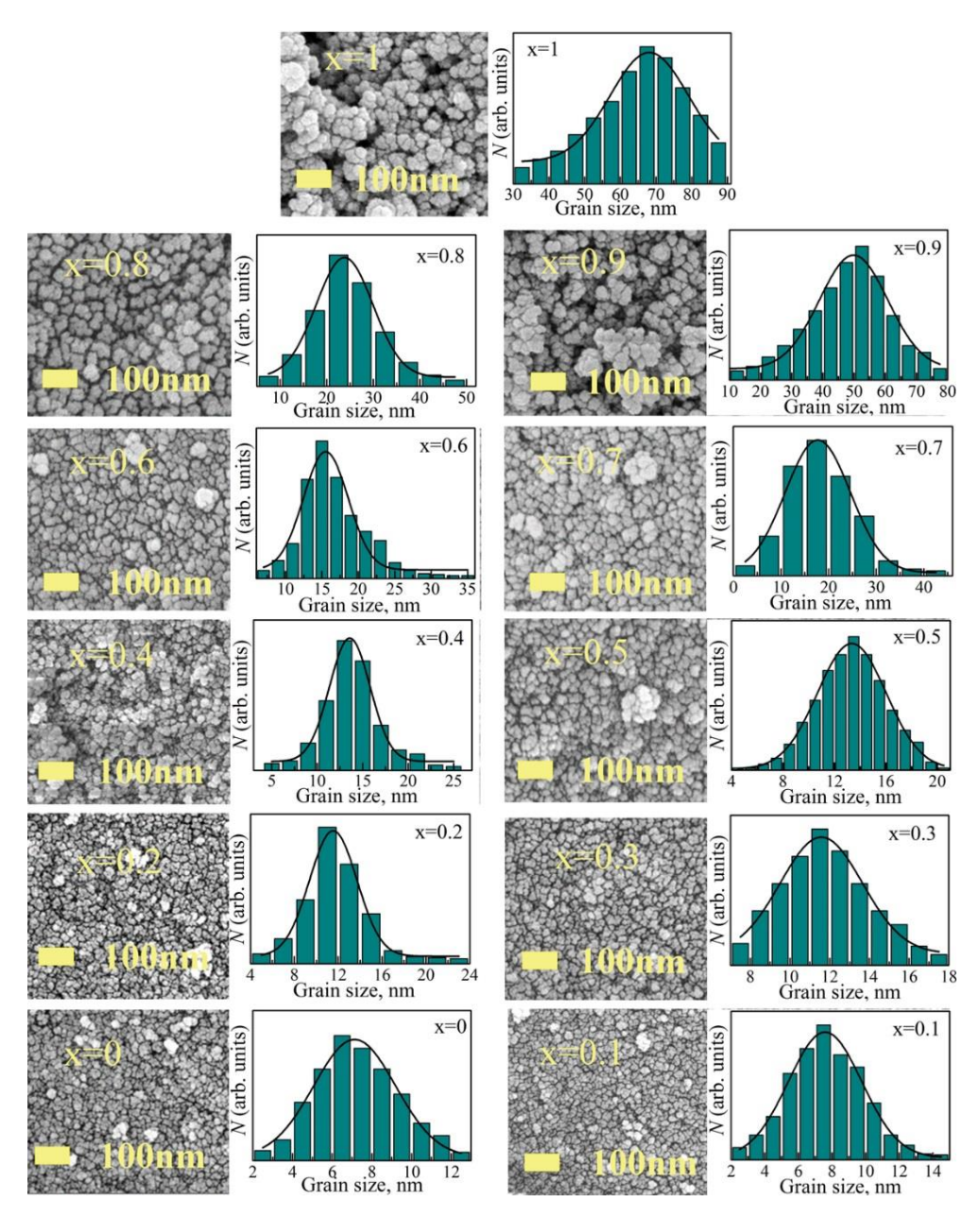


Figure 3.5. FESEM micrographs and grain size distribution histogram of the ZMF nanoparticles.

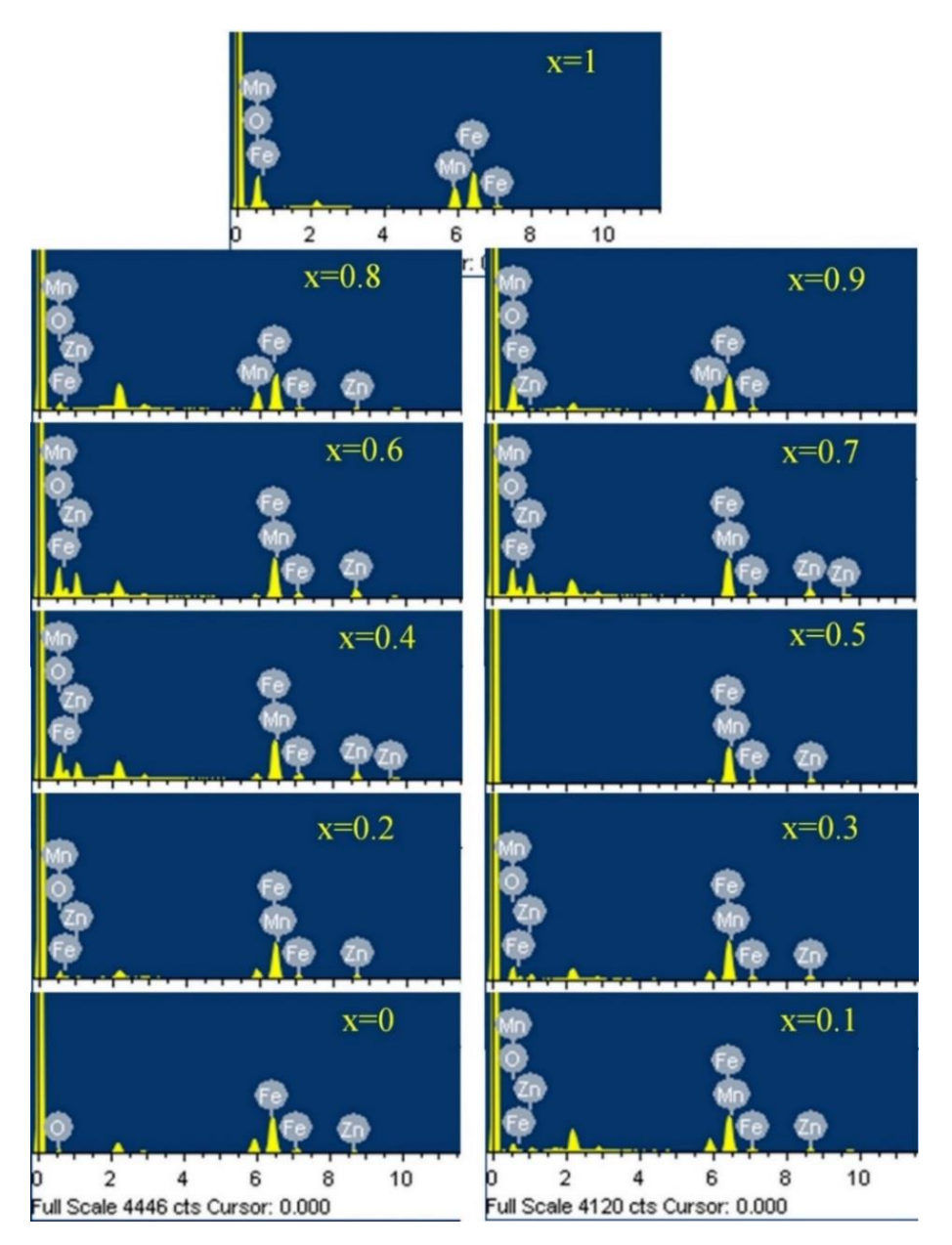


Figure 3.6. EDAX profile of the ZMF nanoparticles.

The characterization of the nanoparticles was complemented by the "energy dispersive X-ray (EDAX) analysis" (Fig. 3.6) that confirmed the concentration of Mn, Zn, Fe and O in all the nanoparticle samples. The EDAX analysis confirms the atomic weight percentage ratio of the atoms (elemental composition) for pure as well as for Mn-doped Zn ferrite nanoparticles and it is matching with the expected values as listed in Table 3.2.

Table 3.2. "Elemental parameters" of the ZMF nanoparticles.

X	Chemical	Ratio of the atom				
formula			(1-x)Zn/2Fe	xMn/2Fe	(1-x)Zn/xMn	
	ZnFe ₂ O ₄	Theoretical values	0.576	_	-	
0		Estimated values from EDAX	0.507			
0.1	$Mn_{0.1}Zn_{0.9}Fe_2O_4$	Theoretical values	0.52	0.049	10.55	
0.1	WIII0.1ZII0.9FE2O4	Estimated values	0.32	0.049	10.55	
		from EDAX	0.40	0.043	10.00	
0.2	$Mn_{0.2}Zn_{0.8}Fe_2O_4$	Theoretical values	0.46	0.098	4.69	
		Estimated values	0.41905	0.091	4.63	
		from EDAX				
0.3	$Mn_{0.3}Zn_{0.7}Fe_2O_4$	Theoretical values	0.404	0.148	2.73	
		Estimated values	0.4	0.176	2.28	
		from EDAX				
0.4	$Mn_{0.4}Zn_{0.6}Fe_2O_4$	Theoretical values	0.346	0.197	1.76	
		Estimated values	0.3	0.17	1.77	
		from EDAX				
0.5	$Mn_{0.5}Zn_{0.5}Fe_2O_4$	Theoretical values	0.288	0.246	1.17	
		Estimated values	0.25	0.2125	1.18	
		from EDAX				
0.6	$Mn_{0.6}Zn_{0.4}Fe_2O_4$	Theoretical values	0.231	0.295	0.781	
		Estimated values	0.2	0.255	0.784	
		from EDAX				
0.7	$Mn_{0.7}Zn_{0.3}Fe_2O_4$	Theoretical values	0.172	0.344	0.502	
		Estimated values	0.169	0.315	0.536	
		from EDAX				
0.8	$Mn_{0.8}Zn_{0.2}Fe_2O_4$	Theoretical values	0.12	0.394	0.293	
		Estimated values	0.1	0.34	0.294	
0.0		from EDAX	0.070	0.110	0.100	
0.9	$Mn_{0.9}Zn_{0.1}Fe_2O_4$	Theoretical values	0.058	0.443	0.130	
		Estimated values	0.053	0.405	0.129	
1.0)	from EDAX		0.402		
1.0	MnFe ₂ O ₄	Theoretical values	-	0.492	-	
		Estimated values		0.477		
		from EDAX				

3.4 Magnetization study

The ZMF is a cubic spinel soft ferrimagnetic material. On reduction of particle size below the critical size limit, ZMF nanoparticles show superparamagnetism. Soft ferrimagnetic and superparamagnetic nanoparticles show high initial permeability, which makes them useful in magnetic sensors, magnetic amplifiers, and other applications. The magnetic field-dependent and temperature-dependent dc magnetization studies were done for the ZMF nanoparticles. Depending upon the magnetic behavior, the prepared ZMF nanoparticles are divided into two types; ferrimagnetic and superparamagnetic.

3.4.3 Magnetic field-dependent magnetization study of ZMF nanoparticles

The magnetic field dependent hysteresis loop tells about the behavior of the material, whether they are ferromagnetic, paramagnetic or superparamagnetic. The coercivity of a magnetic hysteresis loop is directly connected to the nature of the ferrite. Therefore, the hysteresis loop is also helpful in differentiating between soft and hard ferrite [23]. The shape of a hysteresis loop depends on so many factors like non-saturation effects, random distribution of particles, cationic stoichiometry, occupancy of specific sites by cation, surface spin canting, etc. For ferromagnetic/ferrimagnetic materials, the movement of the domain wall is responsible for the magnetic properties because domain walls carry large anisotropy energy. Therefore, the formation of domain occurs in ferromagnetic material to minimize the magnetostatic energy [12], [15], [24-26].

Detailed field dependence magnetization is investigated for the prepared ZMF nanoparticles at 300 and 100 K. Here, the nanoparticles of the composition x=0 and 0.1 show superparamagnetic behavior because of their extremely nano size, which is around 6 nm. From x=0.2 the ferrimagnetic behavior starts dominating over superparamagnetic behavior due to the significant increment in the "crystallite size". As the "crystallite size" is increasing the sample starts showing more ferrimagnetic behavior.

To get the detailed information about the magnetic behavior and magnetic parameters of the samples, the following equation was used to fit the M(H) curves [27-28];

$$M(H) = \left[2\frac{M_s}{\pi} \tan^{-1} \left\{ \left(\frac{H \pm H_c}{H_c}\right) \tan \left(\frac{\pi M_r}{2M_s}\right) \right\} \right] + \chi H$$
 3.1

Here, M_S is "saturation magnetization", M_r refers "remanent magnetization", H_c denotes "coercivity", χ refers "magnetic susceptibility for the paramagnetic part", M_c represents "measured magnetization" and H_c denotes "applied magnetic field". The first term in the eq. 3.1 represents the ferromagnetic/ferrimagnetic contribution, whereas the second term represents the paramagnetic part. M_c data for all the samples fitted well with the eq. 3.1 except x=0 and 0.1 at 300 K. The M_c curves for x=0 and 0.1 did not fit well with eq. 3.1. Therefore for these two M_c plots, we tried Langevin fit (eq. 3.2) of "superparamagnetic nanoparticles". The used Langevin function is as follows [29]:

$$L = M_S * \left[\coth(A * x) - \frac{1}{A * x} \right]$$
 , $x = \mu_0 H / K_B T$ 3.2

Here, A contains information about "average particle magnetic moment", M_S is "saturation magnetization", K_B is "Boltzmann constant", and T represents "temperature" at which measurement was executed.

Fig. 3.7 and 3.8 depict the fitted M(H) curves for the ZMF nanoparticles at 300 and 100 K, respectively. Magnetic parameters obtained from the fitting of M(H) plots are listed in Table 3.3. The experimental saturation magnetization, M_s , is estimated from the intercept on the y-axis by extrapolating the straight line drawn on M vs. H plots. The fitted values are close to the experimental values except for x=0 and x= 0.1 at 300 K because these two samples show superparamagnetic dominance. The lower values of the coercivity (H_c) and remanence (M_R) indicates that all the samples belong to the family of soft ferrites. The M_s -value is increasing with an increase in Mn content.

The increment in magnetization on increasing Mn-content can be ascribed to the following reason;

- (i) Increase in the "average crystallite size" due to the doping of bigger ion (Mn⁺²) as discussed in the XRD analysis. The substitution of bigger size ions changes the bond length and bond angle, which leads to an expansion in the lattice. With the increase in crystallite size, the surface spin effect (dead surface layer) decreases, which leads to an increment in the magnetization [15].
- (ii) Alteration in the cation distribution of spinel structure with Mn substitution in the Zn ferrite [9-10].

It is well known that the "spinel structure" has two sub-lattices: one "tetrahedral" and another "octahedral" sub-lattices and the coupling between these two sub-lattices causes the net magnetization [20]. Since nonmagnetic Zn²+ ions have a strong tendency to occupy the "tetrahedral site", therefore, zinc ferrite exhibits the normal spinel structure. But it is well known that Mn²+ cations can partially occupy both the sub-lattices. Therefore, the substitution of Mn²+ ions in place of Zn²+ ions causes the migration of some Fe³+ ions from "octahedral sites" to "tetrahedral sites". Migration of ions causes an alteration in the magnetic moment on tetrahedral and octahedral sub-lattice, which alters the net M₅ of Mn-doped samples. Increasing the number of Mn²+ ions forces more number of Fe³+ ions to migrate from the octahedral sites to the tetrahedral sites, which ensures more ferrimagnetic behavior of Mn-rich nanoparticle samples.

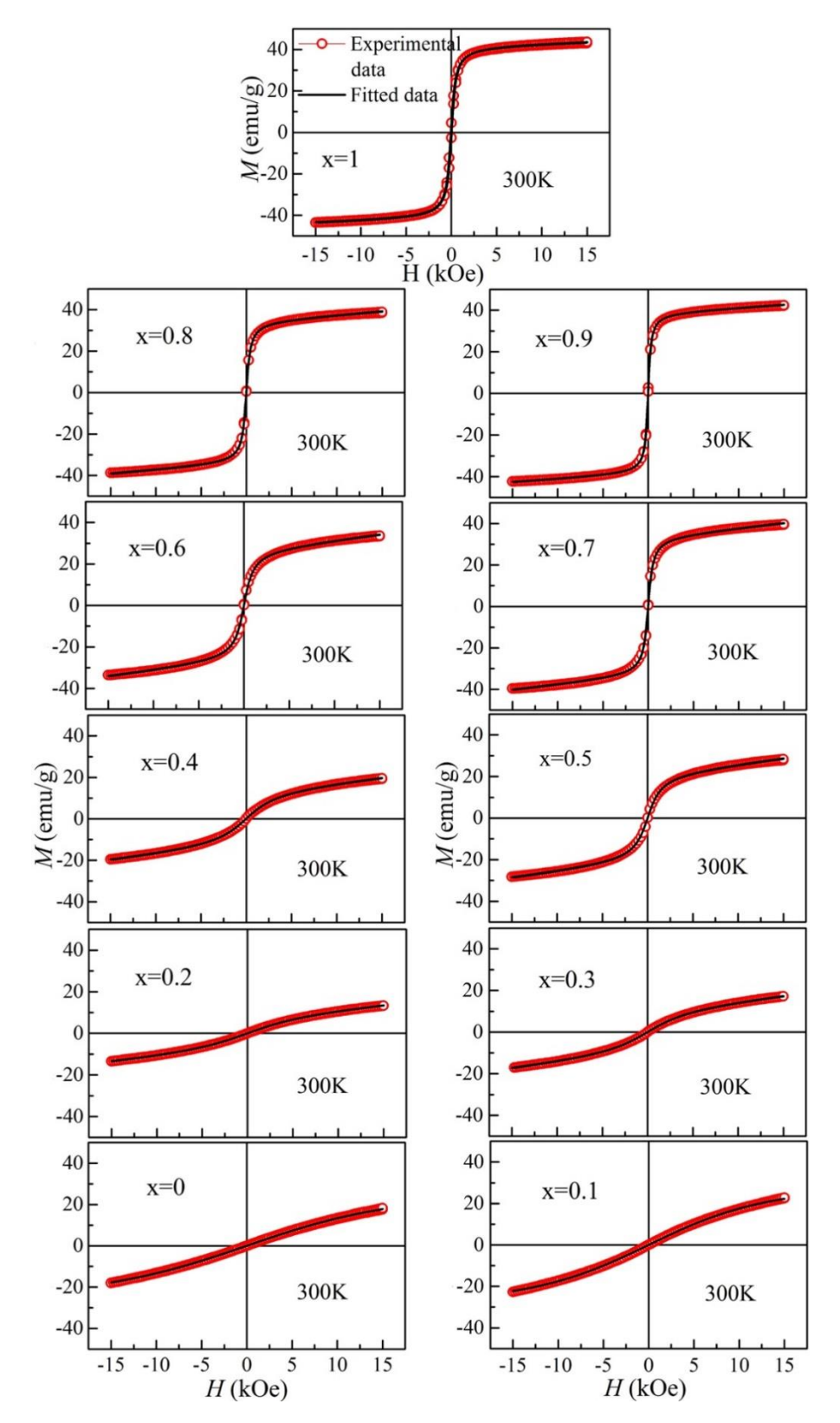


Figure 3.7. Fitted M vs. H plots of the ZMF nanoparticles at 300 K.

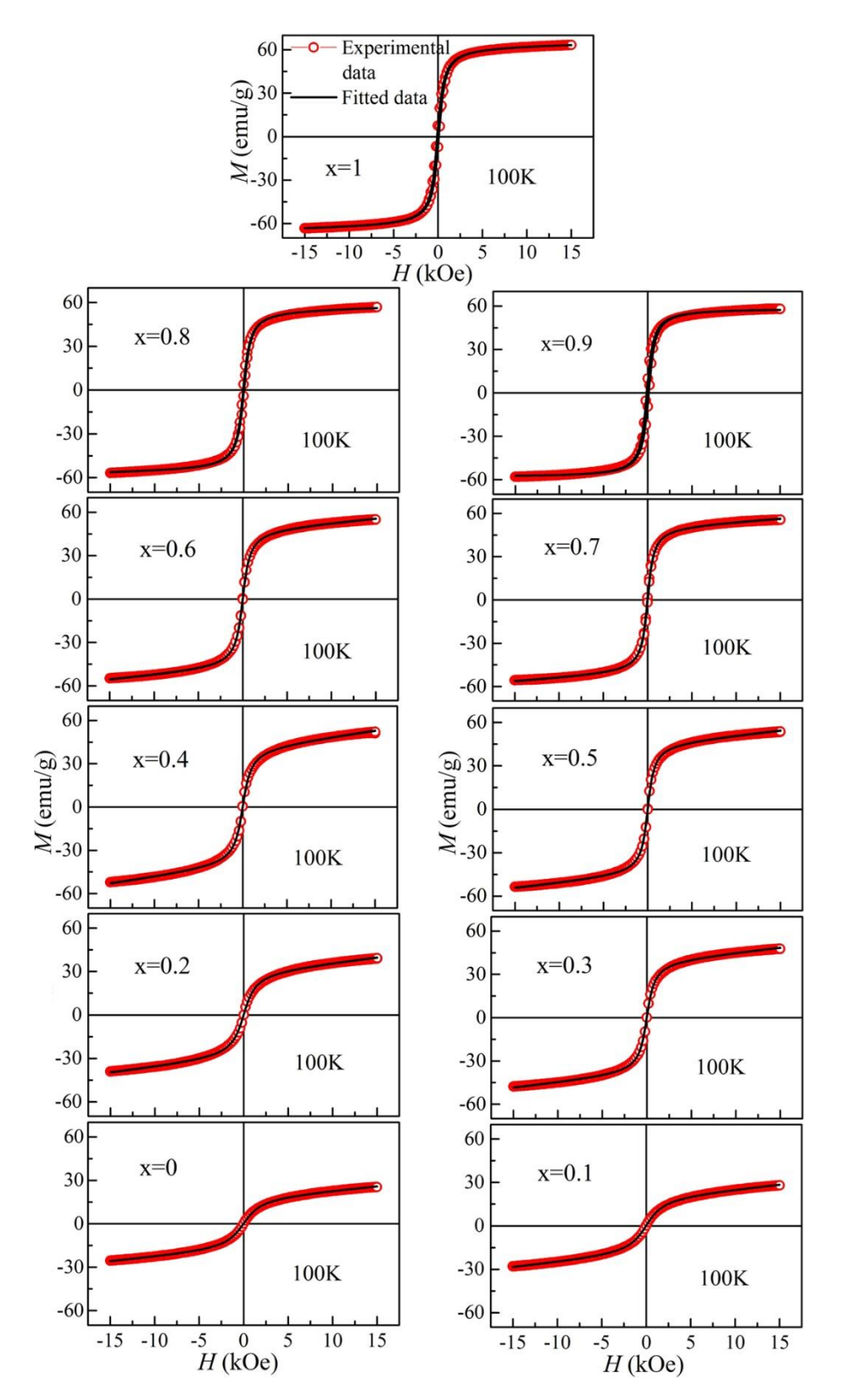


Figure 3.8. Fitted M vs. H plots of the ZMF nanoparticles at 100 K.

The experimentally calculated magnetic parameters $(M_r, H_c, and M_s)$ were also plotted as a function of Mn-doping (x) as demonstrated in Fig. 3.9.

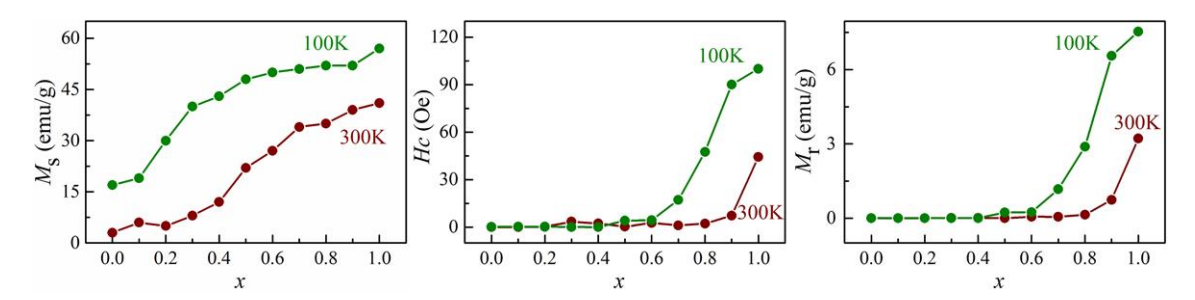


Figure 3.9 M_s vs. x, H_c vs. x, and M_r vs. x plots of ZMF nanoparticles at 300 and 100 K.

X	$M_{\rm s}$	M_s	H _c	$M_{\rm r}$	$M_{\rm s}$	$M_{\rm s}$	H_{c}	$M_{\rm r}$
	(emu/g)	(emu/g)	(Oe)	(emu/	(emu/g)	(emu/g)	(Oe)	(emu/g)
	At 300K	At	At	g)	At 100K	At	At	At
	Experim	300K	300K	At	Experim	100K	100	100K
	ental	Fitted		300K	ental	Fitted	K	
	Value	Value			Value	Value		
0	3	32	0.62	0.003	17	19	0.18	0.001
0.1	6	35	0.78	0.002	19	21	0.29	0.002
0.2	5	9	0.25	0.001	30	30	0.32	0.005
0.3	8	11	3.5	0.007	40	39	0.09	0.005
0.4	12	14	2.4	0.009	43	41	0.01	0.005
0.5	22	22	0.29	0.019	48	49	4.1	0.24
0.6	27	27	2.7	0.058	50	52	4.4	0.24
0.7	34	34	1.1	0.054	51	54	17	1.2
0.8	35	35	2.2	0.14	52	54	48	2.9
0.9	39	39	7	0.74	52	56	111	6.6
1.0	41	42	44	3.2	57	60	90	7.5

Table 3.3. "Magnetic parameters" of M(H) plots of the ZMF nanoparticles.

Further, it is found that H_c increases on increasing Mn content. This variation is attributed to the increase in magnetic anisotropy due to an increase in grain size with increasing Mn content. Moreover, the coercivity values strongly depend on microstructural factors such as grain boundaries [30]. The grain boundaries create pinning centers in the magnetic domain walls due to the defects formed at the interface of the boundaries [31]. Therefore the variation in coercivity may be due to the pinning of magnetic spins at grain boundaries. At 100 K, magnetization, coercivity, and remanence magnetization are increasing as compared to the room temperature values for all the samples due to the formation of ferrimagnetic (FM)

clusters at lower temperatures [7]. As the temperature decreases, the magnetic spins start freezing which leads to the formation of FM clusters. The FM cluster formation is related to the magnetic spin concentration in some regions and their organization of the FM microphase.

3.4.2 Temperature dependent magnetization study of the ZMF nanoparticles

Temperature-dependent magnetization plots M(T) in the temperature range of 100 to 400 K were recorded in "zero field cooled (ZFC)" and "field cooled (FC)" mode at 500 Oe for ZMF nanoparticles. Fig. 3.10 depicts the M(T) plot of the ZMF nanoparticles.

In ZFC mode, the samples were cooled up to 100 K in the absence of the magnetic field and then the magnetization was measured at 500 Oe as a function of temperature. In FC mode, samples were cooled in the field of 500 Oe and then the magnetization measurement was performed as a function of temperature. The ZFC and FC curves overlap each other at high temperature. But with a decrement in temperature, ZFC and FC plots split into different trajectories at low temperatures. The temperature at which the two curves start splitting is known as bifurcation (irreversible) temperature (T_{irr}). This divergence of the ZFC-FC curve is due to magnetic frustration in the This magnetic frustration may be either due to co-existing sample. ferromagnetic/ferrimagnetic and anti-ferromagnetic phases or because of the noninteracting superparamagnetic particles. Moreover, the bifurcation of ZFC and FC curves also depends on the applied magnetic field. The existence of bifurcation confirms the ferrimagnetic or spin-glass behavior of ZMF nanoparticles [32]. The bifurcation temperature (T_{irr}) is increasing with Mn-doping and shows the higher value for higher Mn doping as shown in Fig. 3.11. This change in T_{irr} may be due to the alteration in "crystallite size" and "cation distribution" with Mn-doping. We have also plotted the difference between M(FC) and M(ZFC) as a function of Mn-doping content (x) to get a clear picture of the difference between these two curves. This curve clearly shows that the difference between M(FC) and M(ZFC) is increasing with x, similar to the T_{irr} vs. x plots.

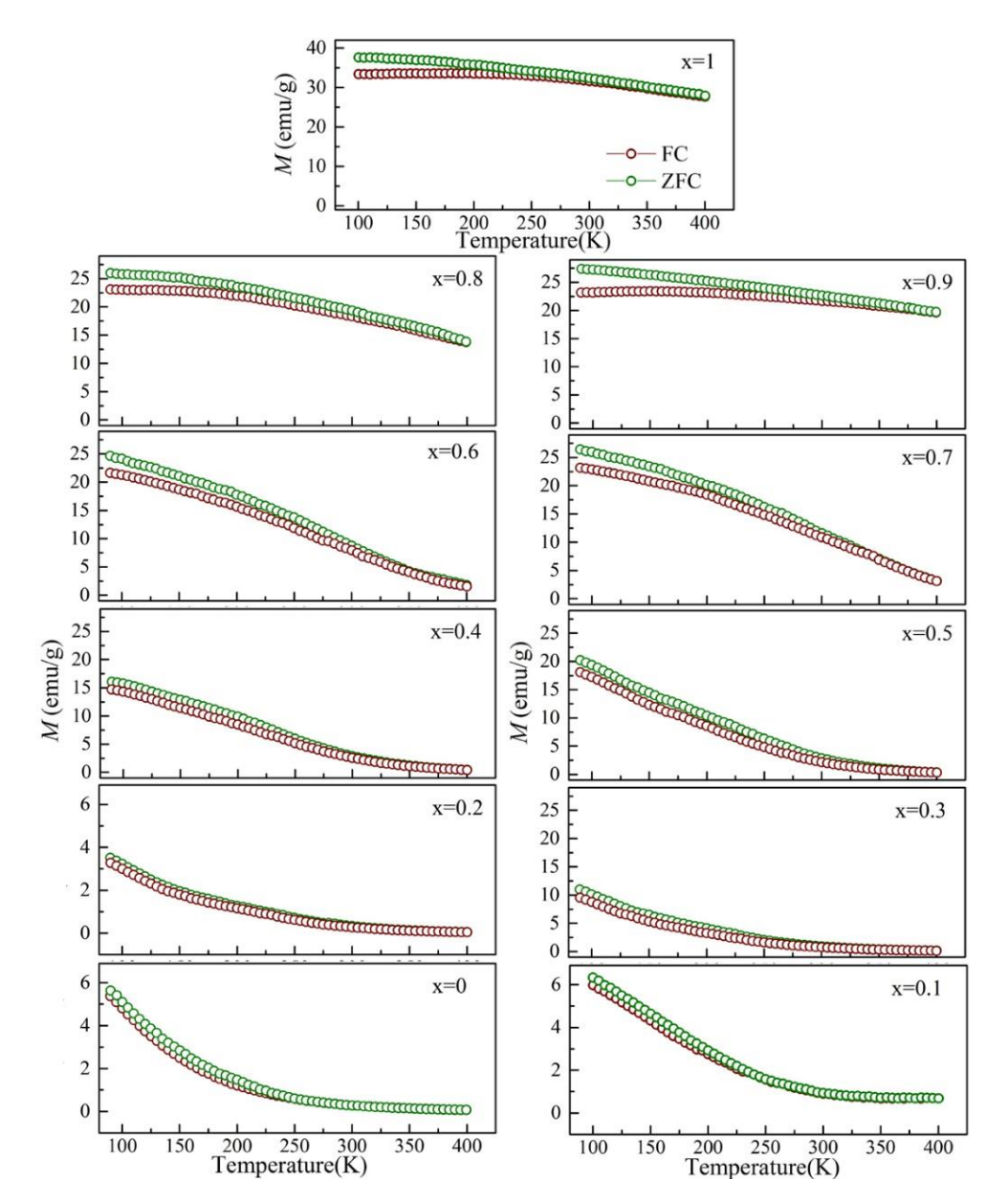


Figure 3.10. M vs. T plots of the ZMF nanoparticles at 500 Oe.

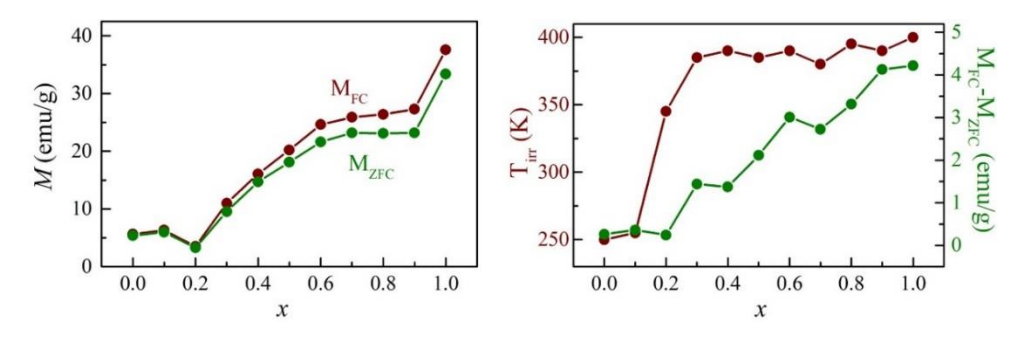


Figure 3.11. M vs. x, T_{irr} vs. x and $(M_{FC}-M_{ZFC})$ vs. x plots of the ZMF nanoparticles.

3.5 FMR Study

The ferromagnetic resonance (FMR) spectroscopy is a very relevant technique to understand the magnetic interaction and magnetic anisotropy present in the magnetic system related to intrinsic as well as extrinsic mechanisms influenced by structural inhomogeneities [32-33]. The FMR lineshape depends on the magnetic resonances of the system. Symmetric lineshape defines paramagnetic interaction, while asymmetric lineshape arises due to multiple resonances which ensures the ferrimagnetic nature of ferrite. We can get a clear picture of magnetic interaction by effective g-value. For paramagnetic material g-value is 2, for antiferromagnetic it is less than 2 and for ferromagnetic/ferrimagnetic material, it is greater than 2. Therefore this technique is used to investigate the magnetic interaction present in the ZMF nanoparticles.

The FMR spectra give information about the superexchange between the sublattices of spinel ferrite. Therefore, variation in the magnetic interaction due to the Fe⁺³ distribution among octahedral and tetrahedral sublattice can be investigated by the FMR spectra of the ZMF nanoparticles. Fig. 3.12 shows FMR spectra for the ZMF nanoparticles at room temperature. It can be seen that FMR spectra (lineshape) are becoming more asymmetric with increasing Mn-doping, which indicates that ferrimagnetic interaction is more in Mn-rich samples. Shifting of FMR spectra is also observed from Fig. 3.12, FMR spectra is shifting towards the lower magnetic field with increasing Mn-doping. To understand this variation we have calculated the resonance field (H_r), g-value and linewidth (D) from the FMR spectra and plotted as a function of Mn-doping content (x) which is demonstrated in Fig. 3.13.

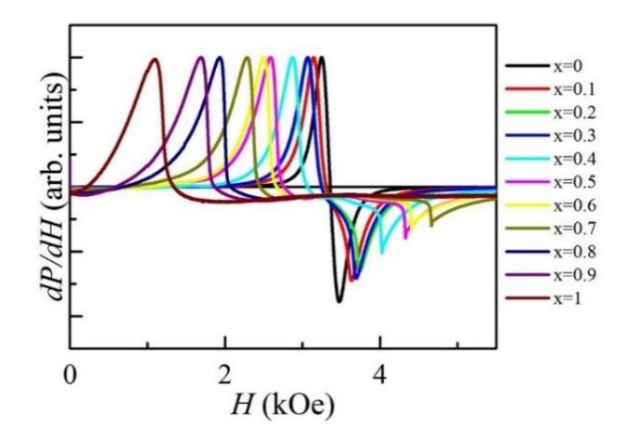


Figure 3.12. FMR spectra of the ZMF nanoparticles at 300 K.

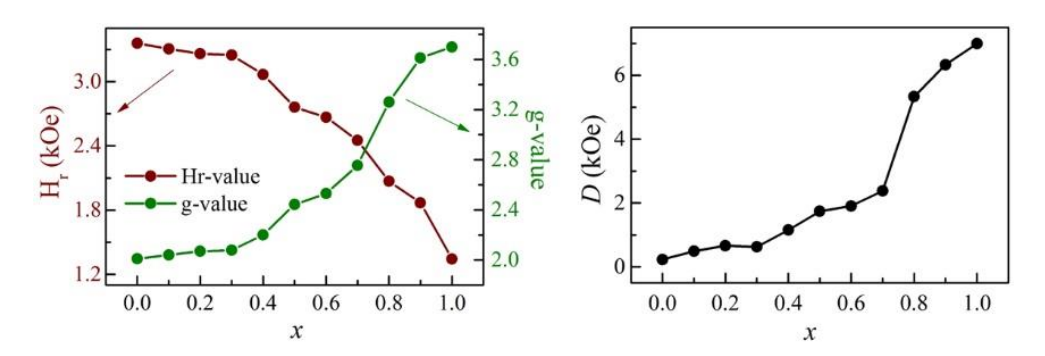


Figure 3.13. H_r vs. x, g-value vs. x, and D vs. x plots of the ZMF nanoparticles at 300 K.

The change of Hr-value is linked with the internal field ferromagnetic/ferrimagnetic sample [32]. Therefore, the decrease in Hr-value can be related to the increase in the internal magnetic field. The H_r- value decreases monotonically with an increase of "average crystallite size" of the ZMF nanoparticles. This shows an increment in ferrimagnetic interactions as particle size increases. Further, a monotonic increase in D and g-value with increasing Mn-doping also indicates that ferrimagnetic interaction is more for Mn-rich samples. The FMR spectra show that the ZMF nanoparticles are more ferrimagnetic with increasing Mndoping similar to the field-dependent magnetization results [34-35]. This can be attributed to the short-range antiferromagnetic order with increasing size. Hence, FMR data supports magnetization results.

3.6 Chapter Summary

In summary, we report the single-phase cubic spinel ZMF nanoparticle formation via the co-precipitation route. Rietveld analysis confirms the single-phase cubic spinel structure with the Fd-3m space group without any detectable impurity phase. The lattice constant and crystallite size are increasing with an increase in Mn content. Microstructural and Raman studies complement the XRD results. Ferrimagnetic ordering is confirmed via the magnetic hysteresis loop. It is found that the substitution of Mn²⁺ ion at the tetrahedral site in Zn-ferrite enhanced the ferrimagnetic (FM) interactions in the final material. These results confirm that the magnetic properties rely on the cation distribution of the prepared samples, microstructure and crystallite size of the nanoparticles. M(T) and FMR studies also support the M-H results.

References

- 1. J. Smit, Magnetic Properties of Materials, McGraw Hill, New York (1971).
- 2. L. G. Van Uitert, Proc. IRE. 44, 1294-1303 (1956).
- 3. H. F. Cheng, J. Appl. Phys. 55, 1831-1837 (1984).
- 4. A. Figuerola, R. D. Corato, L. Manna and T. Pellegrino, *Pharmacol. Res.* **62**, 1126-1143 (2010).
- C. Rath, K. K. Sahu, S. Anand, S. K. Date, N. C. Mishra and R. P. Das, *J. Magn. Mag. Mater.* 202, 77-84 (1999).
- 6. O. Kaman, J. Kuličková, V. Herynek, J. Koktan, M. Maryško, T. Dědourková, K. Knížek and Z. Jirák, *J. Magn. Mag. Mater.* **427**, 251-257 (2017).
- 7. A. Farheen and R. Singh, AIP Conf. Proceed. 1953, 120067 (2018).
- 8. A. Farheen and R. Singh, *Mater. Res. Express* **6**, 114001 (2019).
- 9. A. Farheen and R. Singh, IOP Conf. Ser.: Mater. Sci. Eng. 577, 012057 (2019).
- 10. A. Farheen and R. Singh, *Integrated Ferroelectrics* **203**, 91-96 (2019).
- 11. E. W. Gorter, *Philips. Res. Rep.* **9**, 295 (1954).
- 12. F. Liu, Y. Hou, and S. Gao, Chem. Soc. Rev. 43, 8098-8113 (2014).
- 13. H. Y. Deng and H. L. Huang, J. Magn. Magn. Mater. 209, 37-41 (2000).
- 14. R. Valenzuela, F. Herbst and S. Ammar, *J. Magn. Magn. Mater.* **324**, 3398-3401 (2012).
- 15. G. Thirupathi and R. Singh, *IEEE Transactions on Magnetics* **48**, 3630–3633 (2012).
- 16. G. K. Williamson and W. H. Hall, *Acta Mater.* **1**, 22 (1952).
- 17. Z. Wang, P. Lazor, S. K. Saxena and H. St. C. O'Neill, *Material Research Bulletin* 37, 1589-1602 (2002).
- 18. O. N. Shebanova and P. Lazor, *J. Solid State Chemistry* **174**, 424-430 (2003).
- 19. P. Chandramohan, M. P. Srinivasan, S. Velmurugan and S.V. Narasimhan, *J. Solid State Chemistry* **184**, 89-96 (2011).
- 20. J. Smit and H. P. T. Wijn, *Ferrites*, Philips' tech. Library, Eindhoven (Holland) (1959).
- 21. L. Malavasi, P. Galinetto, M. C. Mozzati, C. B. Azzoni and G. Flor, *Physical Chemistry Chemical Physics* **4**, 3876-3880 (2002).

- 22. A. Goldman, *Modem Ferrite Technology*, 2nd Ed. Springer Science, New York (2006).
- 23. P. K. Manna, S. M. Yusuf, M. Basu, and T. Pal, *J. Physics: Condensed Matter* **23**, 506004 (2011).
- 24. Timothy E. *Kidd*, *Dopant Driven Electron Beam Lithography*, *INTECH* Open Access Publisher (2012).
- 25. K. Velmurugan, V. S. K. Venkatachalapathy, and S. Sendhilnathan, *Materials Research* **12**, 529-534 (2009).
- 26. K. C. George, S. Kurien, and J. Mathew, J. Nanosci Nanotechnol 7, 2016-2019 (2007).
- 27. S. Duhalde and et al, *Phys. Rev. B* **72**, 161313 (2005).
- 28. M. B. Stearns and Y. Cheng, J. Appl. Phys. 75, 6894 (1994).
- 29. C. P. Bean and J. D. Livingston, J. Appl. Phys. 30, 120-S (1959).
- 30. F. Li, J. Sun, X. Wang, and J. Wang, *IEICE Trans. Electron.* **E90-C**, 1561-1564 (2007).
- 31. J. Sun, Z. Wang, Y. Wang, C. Yao, K. Wei, T. Shen and F. Li, *Vacuum* **86**, 461-465 (2011).
- 32. A. Farheen and R. Singh, J. Superconductivity and Novel Magnetism 32 (2019).
- 33. V. Castel, J. Ben Youssef, and C. Brosseau, J. Nanomaterials 2007, 27437 (2007).
- 34. B. Aktas, L. Tagirov, and F. Mikailov, *Nanostructured Magnetic Materials and their Applications*, Springer Science & Business Media, Berlin (2013).
- 35. M. Bohra, S. Prasad, N. Venkataramani, N. Kumar, S. C. Sahoo, and R. Krishnan, *IEEE Transactions on Magnetics* **47**, 345-348 (2011).

Chapter 4

Structural, optical and magnetic properties of Mn-Zn ferrite thin films

This chapter consists of an elaborated study of structure, morphology, optical and magnetization behavior of spinel $Mn_{0.5}Zn_{0.5}Fe_2O_4$ (MZF) thin films deposited via RF sputtering under different conditions.

4.1. Introduction

Spinel structured ferrite thin films are well known for their high-frequency applications [1-2] due to their low conductivity than metal films. The tuning of material properties according to specific applications is an important activity in recent years. Several efforts to obtain enhanced frequency with low-loss materials for electronics and communication applications allowed the Mn-Zn ferrites to be one of the most cited magnetic materials. Mn-Zn ferrites possess a mixed spinel structure and give high magnetization when deposited in an argon environment [3-4]. The study of the Mn-Zn ferrite thin films is of great interest due to the fundamental differences in their magnetic and electronic properties from the bulk counterparts. These films have the potential to replace the bulk external magnets in current devices [5-6].

4.2 Selection of target composition for thin film deposition

As discussed in chapter third we have made a series of Mn-doped Zn-ferrite nanoparticles. To make the thin film, we have selected $Mn_{0.5}Zn_{0.5}Fe_2O_4$ out of all the prepared composition. The selection of the target composition was based on the XRD result of the sintered nanoparticles. The $Mn_xZn_{1-x}Fe_2O_4$ (x = 0 to 1) nanoparticles mixed with approximately 1wt % polyvinyl alcohol (PVA) were ground and pressed into pellets using a "cold uniaxial hydraulic press". Then the pressed pellets were sintered in a furnace at $1200^{\circ}C$ for 6 hours in an air environment. To check the phase

formation, the XRD measurement on the sintered nanoparticles was performed which evidences the third phase formation after x=0.6 as shown in Fig. 4.1, that can be attributed to the different valence state of iron and manganese ions at high sintering temperature.

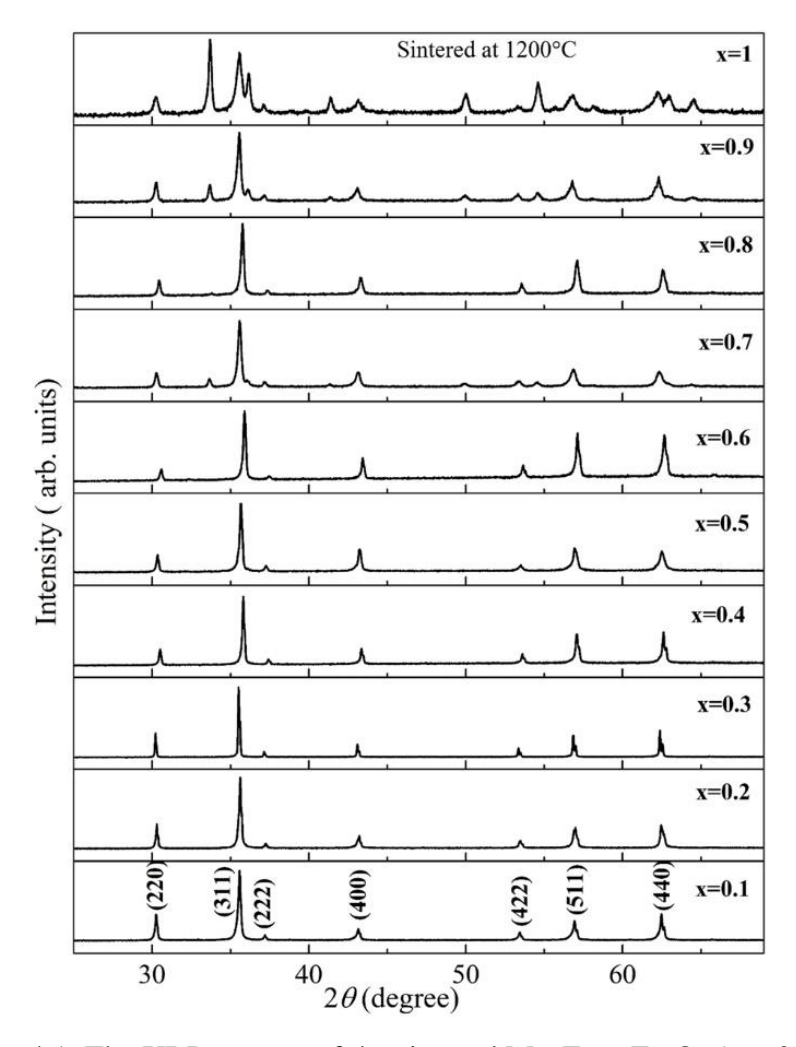


Figure 4.1. The XRD pattern of the sintered Mn_xZn_1 -xFe₂O₄ (x = 0 to 1).

Therefore, to avoid the third phase formation in the thin films we have not selected the composition from x=0.6. The magnetization vs. applied field (M(H)) plot of the $Mn_{0.5}Zn_{0.5}Fe_2O_4$ (MZF) target is shown in Fig 4.2. A well-defined hysteresis loop confirms the soft ferrimagnetic nature of the target material with a magnetization value of 40 emu/g.

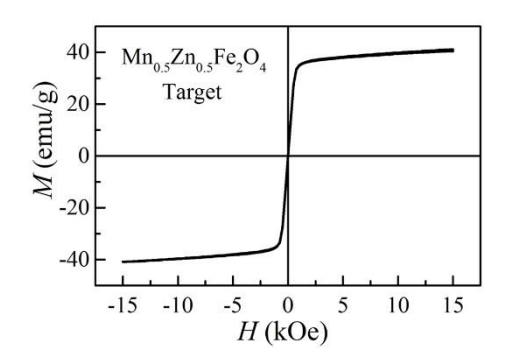


Figure 4.2. The M(H) plot of the Mn_{0.5}Zn_{0.5}Fe₂O₄ target.

The MZF thin films were deposited by RF-magnetron sputtering on 0.5 mm thick quartz substrates under different conditions in an argon gas environment using a 2-inch circular MZF target synthesized via the co-precipitation method as described in chapter 2. The substrate was kept at room temperature during the deposition of all the MZF films. The distance between the target and substrate was kept ~ 6 cm. We have deposited three sets of thin films by varying deposition parameters (such as argon gas pressure, RF power, and deposition duration) which are as follows;

- 1. MZF thin films deposited at different argon gas pressure (i.e. 8, 10, 12, 14, 16 and 18 mTorr) using 50 Watt RF power for 60 minutes.
- 2. MZF thin films deposited at different RF power (i.e. 50, 75, and 100 Watt) in an argon gas pressure of 10 mTorr for 60 minutes.
- 3. MZF thin films deposited for different deposition duration (i.e. 20, 30, 40, 50, and 60 minutes) in an argon gas pressure of 10 mTorr using RF power of 100 Watt.

The structure and morphology of all the as-deposited MZF films were well investigated. The magnetization measurements and FMR studies were done at room temperature to understand the magnetic behavior and anisotropy present in the as-deposited MZF films.

4.3 Structural Study of MZF films

The XRD patterns of the MZF film deposited under different conditions in an argon gas environment are shown in Fig. 4.3. The pattern shows weak peaks corresponding to the cubic spinel structure according to the "Joint Committee on Powder Diffraction Spectra (JCPDS, Pack No. 742402)". The significant amorphous background is

introduced by the quartz substrate [4]. To confirm this, we have also performed XRD for blank quartz substrate and target material which are also shown in Fig. 4.3.

As we can see, the XRD pattern of the substrate is completely amorphous whereas the target's XRD pattern depicts the peaks of the cubic spinel structure [7]. These results confirm that the observed peaks in the XRD pattern of the MZF thin films are related to the target material. The broadness ("full-width at half maxima") and intensity of the XRD peak tell about the size and crystallinity of the samples. Therefore, a small improvement in the intensity of XRD peaks is the evidence of an increase in the crystallinity of the film with increasing RF power as well as with increasing deposition duration. However, when we are increasing argon gas pressure a decrease in the peak intensity is observed due to back diffusion [8]. The sputtering rate increases on increasing chamber pressure due to the increase in the ion density at chamber up to a certain pressure but further increase in the chamber pressure leads to back diffusion and collisions with argon ions.

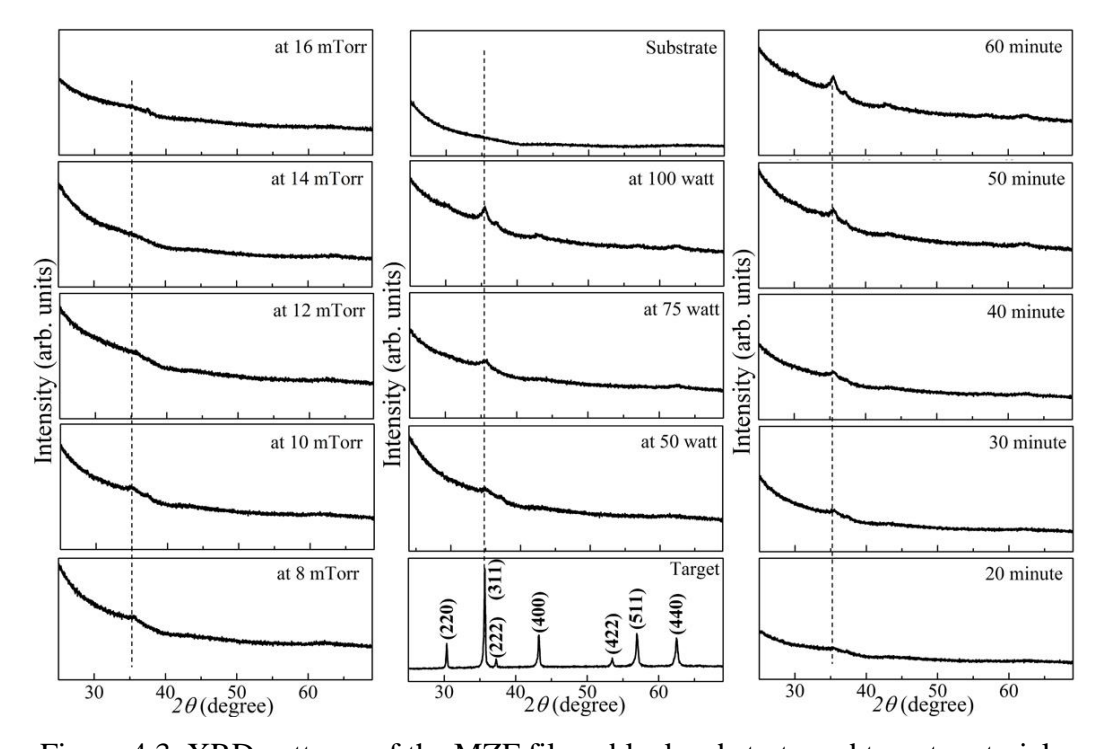


Figure 4.3. XRD patterns of the MZF films, blank substrate and target material.

Since the XRD peaks are not sharp and well defined, the estimation of lattice parameters is not very accurate but for comparison between different films, we have approximated the values from the XRD data. The "Debye-Scherer formula" was used to calculate the "average crystallite size" of the MZF films [3, 9];

$$D = \frac{0.9\lambda}{\beta \cos \phi} \tag{4.1}$$

Here, λ represents "X-ray source wavelength", ϕ denotes "Bragg's diffraction angle" and β refers to "full width at half maximum".

The lattice parameters were calculated using "Bragg's law" $n\lambda = 2dsin\phi$, and $\frac{1}{d^2} = \frac{1}{a^2} + \frac{1}{b^2} + \frac{1}{c^2}$ formula [3]. Here, λ is "X-ray source wavelength" (1.5406 Å for Cu source), ϕ is "Bragg's diffraction angle", d is "distance between two adjacent planes", h, k, l are "miller indices" and a, b, c are the "lattice constants". Here for cubic structure, a=b=c is considered. The estimated lattice parameters of all the samples are listed in Table 4.1. The structural parameters vs. deposition conditions plots of asgrown MZF films under different conditions are depicted in Fig. 4.4. After 10 mTorr argon gas pressure, the XRD pattern did not show clear peaks, therefore, we were not able to calculate the structural parameters of the films deposited in argon gas at 12, 14 and 16 mTorr chamber pressure.

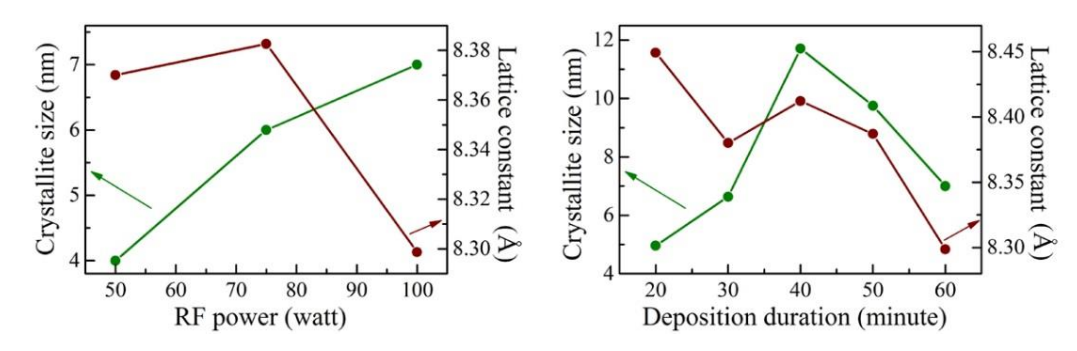


Figure 4.4. Structural parameters vs. deposition conditions plots of all the MZF films.

As expected, the estimated crystallite size and lattice constants are nearly the same for all the MZF films. The calculated lattice constants are in the range of 8.3-8.6 Å. The average crystallite size is in the range of 5-12 nm for all the as-grown films. These values evidence the nanocrystalline nature of the MZF films. The broad XRD

peaks confirm the nanosize of crystallite present in the films similar to the calculated values. It is found that the lattice parameters are not systematic with argon gas pressure, RF power and deposition duration. The oscillatory behavior of lattice parameters with increasing power, pressure and deposition duration gives a hint that the unit cell is going through lattice distortions with a change in the deposition conditions.

Table 4.1. "Crystallographic parameters", "film thickness" and "optical parameters" of the MZF film deposited under different conditions.

Deposition parameter	Average crystallite size (nm) (XRD)	Average grain size from FESEM histogram (nm)	Lattice constant, a (Å)	Film thickness (nm) FESEM	Film thickness (nm) Optical	Optical bandgap (eV)			
Deposited at various argon gas pressure at 50 Watt for 60 minutes.									
8 mTorr	5	7	8.56	315	322	2.9			
10 mTorr	4	6	8.37	350	331	2.8			
12 mTorr	-	7	-	380	369	3.0			
14 mTorr	-	8	-	410	398	2.7			
16 mTorr	-	8	-	398	380	2.7			
Deposited i	n an argon g	as pressure of	10 mTorr fo	or 60 minutes	s at various F	RF power.			
50 watt	4	6	8.37	354	331	2.8			
75 watt	6	8	8.38	459	416	2.7			
100 watt	6	8	8.29	560	553	2.7			
Deposited in an argon gas pressure of 10 mTorr at 100 Watt for different duration.									
20 minute	5	6	8.45	243	- 1	3.1			
30 minute	7	8	8.38	300	351	3.1			
40 minute	12	13	8.41	456	489	2.6			
50 minute	10	11	8.37	500	521	2.7			
60 minute	6	8	8.29	560	553	2.7			

4.4 Microstructural Study of MZF films

The morphological studies of the MZF thin films were done using "field emission scanning electron microscopy (FESEM)". Fig. 4.5, 4.6, and 4.7 show FESEM micrographs in surface and cross-sectional view of all the as-deposited MZF films deposited under different conditions. Surface micrographs show the small nanocluster formation with a change in cluster size on changing deposition conditions. The deposition rate changes due to the change in argon gas pressure and RF power.

The growth of the film is affected by several factors such as internal stresses, preferential alignment of nanocrystalline grains and nucleation rate during the deposition, etc. [10]. The morphology of the films is also affected by the pressure of the gas used, solidification process and nucleation rate during the deposition. This causes an extra anisotropy in the grain's shape.

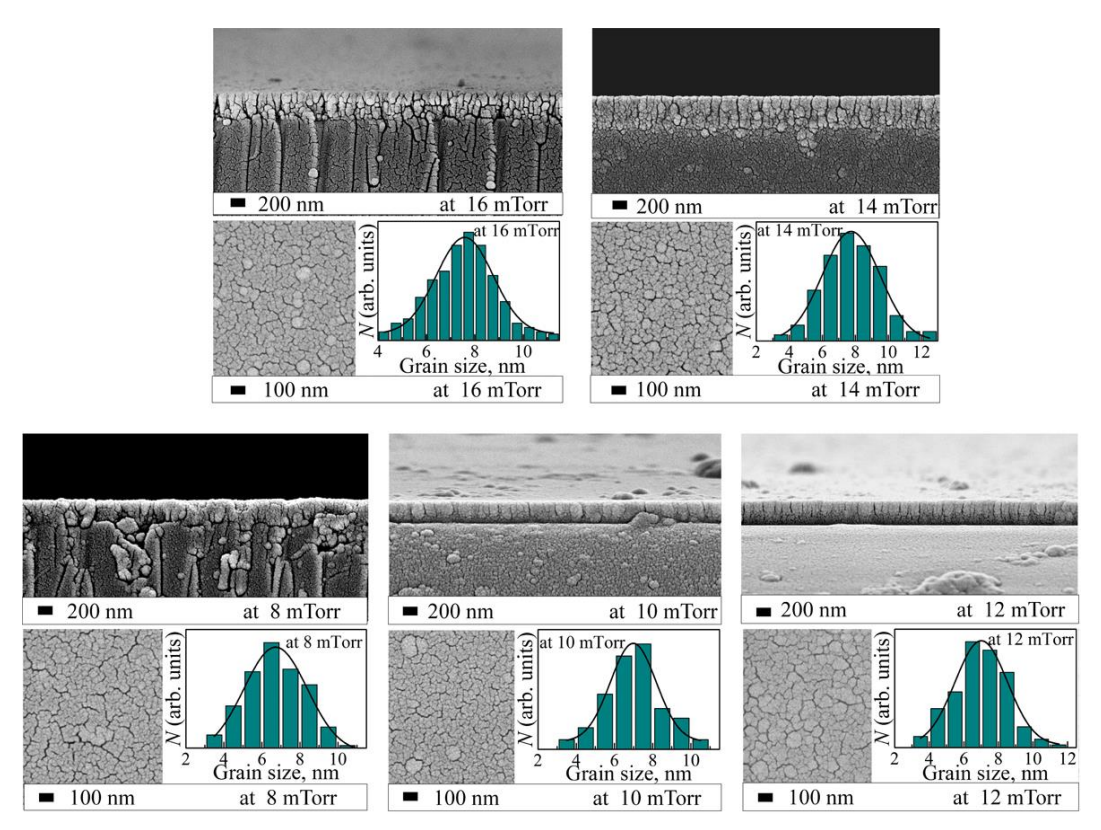


Figure 4.5. FESEM micrographs in cross-section and surface view of MZF films deposited under different argon pressure.

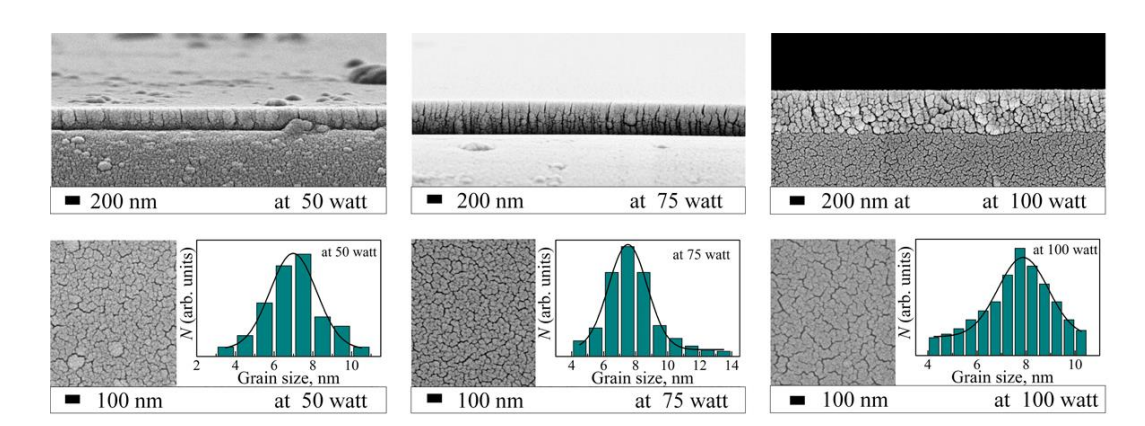


Figure 4.6. FESEM micrographs in cross-section and surface view of MZF films deposited at different RF power.

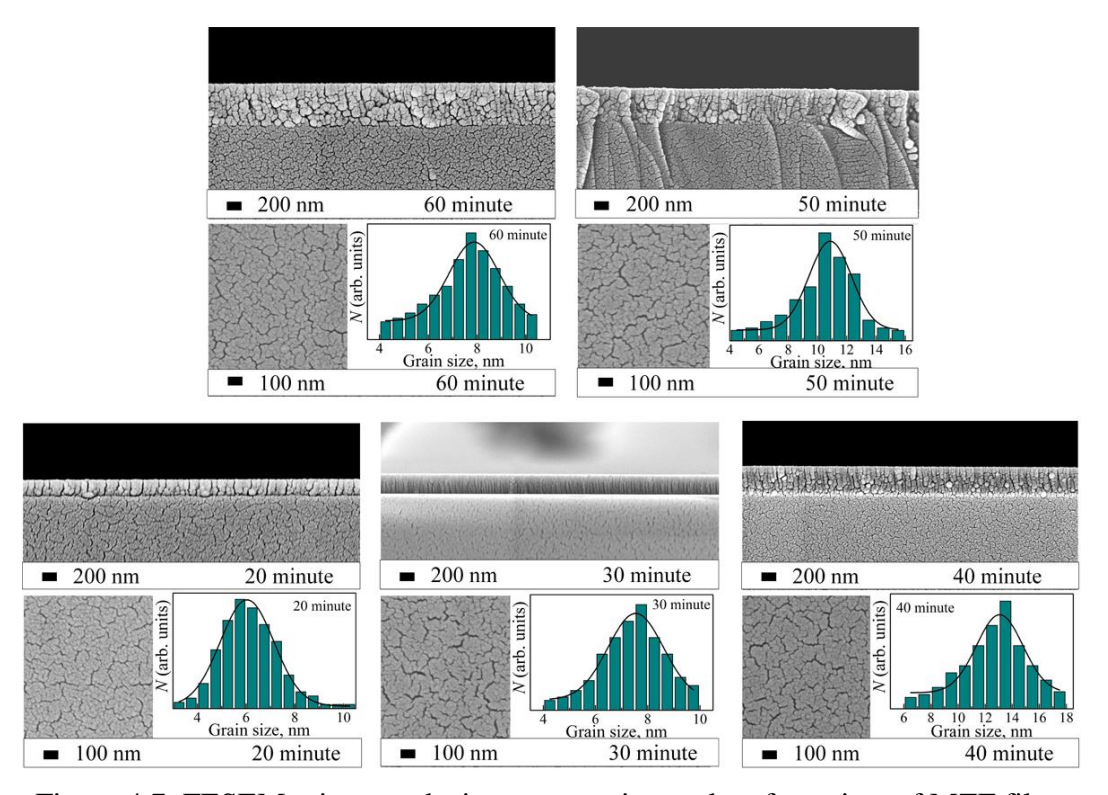


Figure 4.7. FESEM micrographs in cross-section and surface view of MZF films deposited for different duration.

The columnar growth is observed in all the as-deposited MZF films from the cross-sectional images. The thickness of the films is also estimated from the cross-sectional micrographs and listed in Table 4.1. Film thickness is increasing with an increase in argon gas pressure, RF power and deposition duration. But for the films deposited under different argon pressure, film thickness variation is less compare to the other films deposited under different RF power and duration.

The histogram of particle count (N) is plotted to realize the "grain size distribution" of the grains in the MZF films as shown in Fig. 4.5, 4.6, and 4.7 (inset). The histogram is well fitted with "Gaussian peak function" which indicates an almost narrow distribution of grains. The obtained values of "average grain size" from the fits are tabulated in Table 4.1 and are matching with the values obtained from the XRD analysis. The "average grain size" and "film thickness" are plotted as a function of deposition conditions for all the MZF films as shown in Fig 4.8. The variation of "average grain size" is non-systematic and confirms the nanocrystalline nature of the as-deposited MZF films.

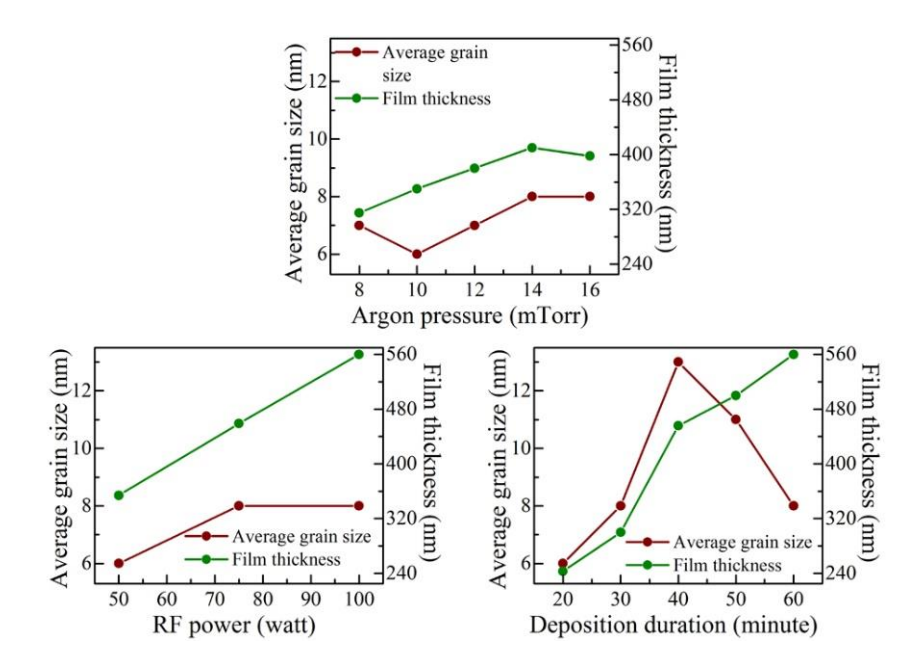


Figure 4.8. Average grain size and film thickness vs. deposition condition plots of the MZF films.

4.5 Optical Study of MZF films

The analysis of the optical transmission spectra is important to understand the dependence of optical constants and optical bandgap on the structure of the films. The thickness of the thin films can also be calculated using the transmission spectra. The "optical constants" of the films rely on the deposition condition [11-12] therefore, we have analyzed the influence of the deposition condition on the optical behavior of the MZF films.

Transmittance spectra: Fig. 4.9, 4.10, and 4.11 show the "optical transmission spectra" in the wavelength range of 200-2500 nm of various MZF films. The strong band edge absorption is observed for the films in the wavelength region of below 500 nm. The fringes appear in the "transmission spectra" due to the interference of the incident light on the "air-film", "film-substrate", and "substrate-air interfaces".

All the spectra show complete absorption in the "UV region", transmittance above 50% in the "visible region" and transmittance up to 90% in the "IR region". About 40-90% transmission is observed above the band edge. It is observed that the number of fringes is increasing with an increase in RF power and deposition duration. This clearly indicates an increase in the film thickness with the increase in deposition duration and RF power which supports the FESEM results. Whereas for the films deposited under different argon pressure, transmittance spectra are not changing much which shows less variation in film thickness. Hence, the optical transmittance data complements the FESEM result.

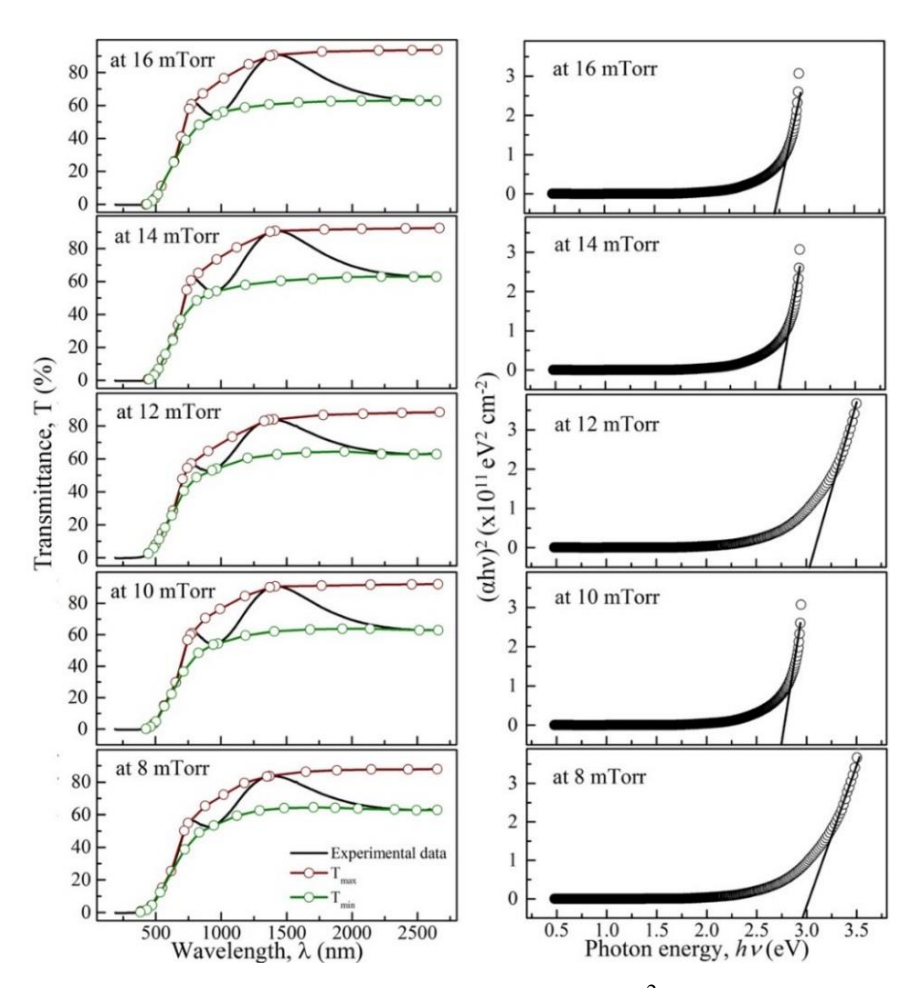


Figure 4.9. The transmittance spectra and $(\alpha h v)^2$ vs. hv plots of the MZF films deposited under different argon pressure.

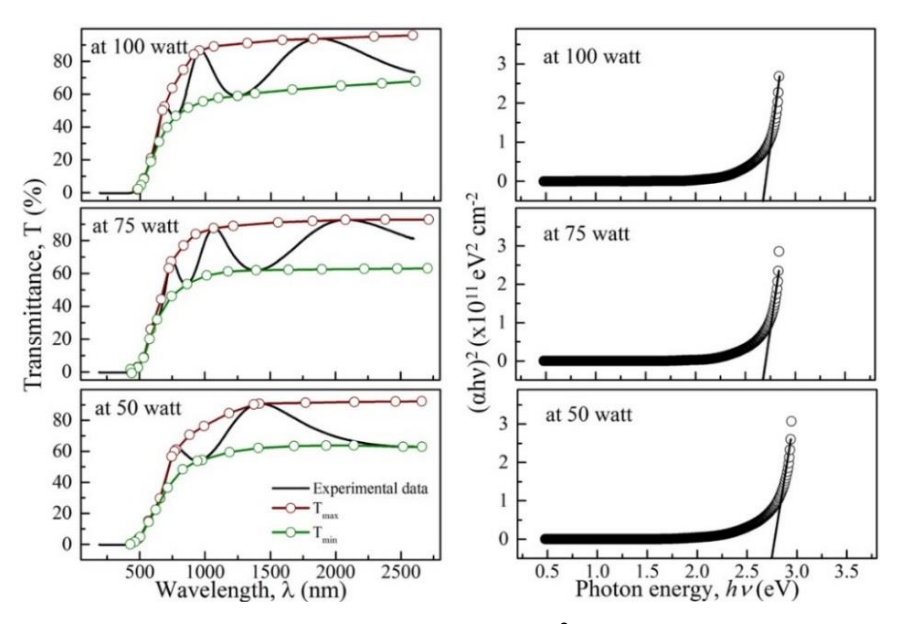


Figure 4.10. The transmittance spectra and $(\alpha h v)^2$ vs. hv plots of the MZF films deposited at different RF power.

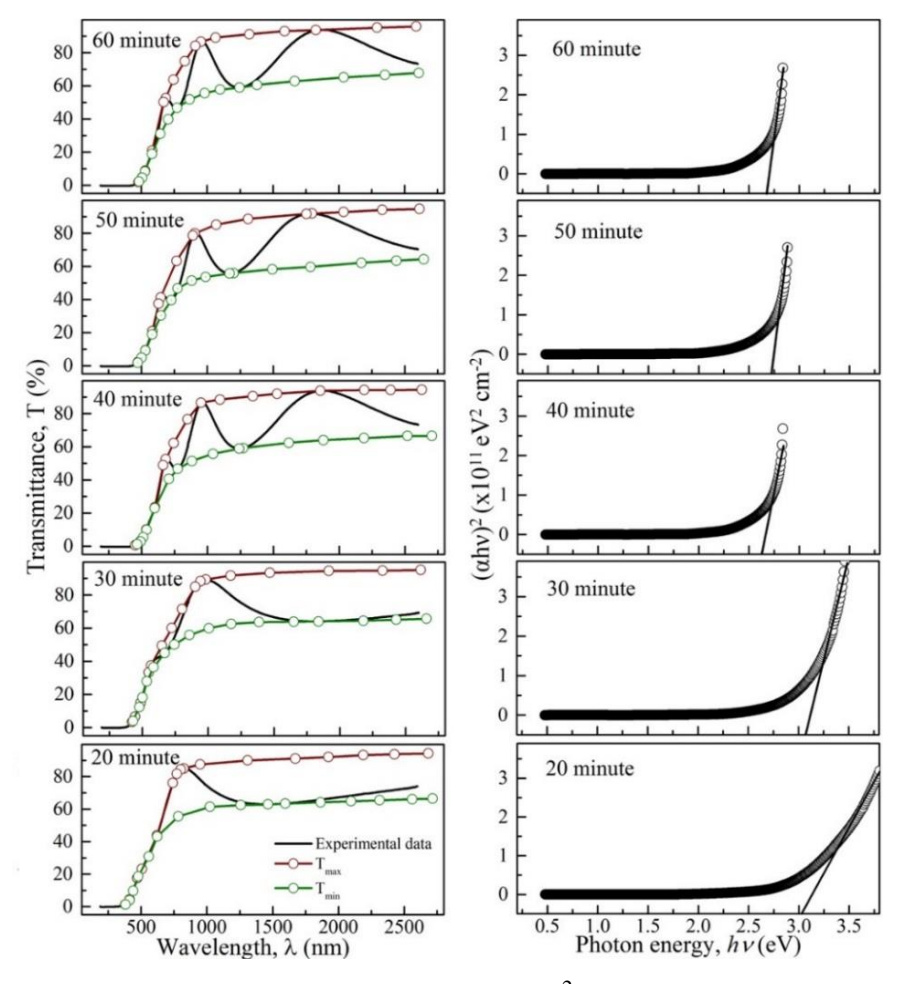


Figure 4.11. The transmittance spectra and $(\alpha h v)^2$ vs. hv plots of the MZF films deposited for different duration.

Film thickness calculation from the optical data: The thickness of the film was calculated from the interference fringes using the envelope method developed by "Swanepole" [13], which uses T_{max} and T_{min} in the transmittance pattern to calculate the "refractive index (n)" at that point corresponding to certain wavelength (λ) given by the relation,

$$n = \left[N + \sqrt{N^2 - n_s^2}\right]^{\frac{1}{2}} \tag{4.2}$$

Where,

$$N = 2n_s \left[\frac{T_{max} - T_{min}}{T_{max} T_{min}} \right] + \frac{n_s^2 + 1}{2}$$
 (4.3)

Here, n_s is the "refractive index of the substrate" (for quartz n_s =1.52). The MZF thin film thickness (d) was calculated by estimating the "refractive index of the thin film" for two consecutive maxima/minima using the following equation;

$$d = \frac{\lambda_1 \lambda_2}{2[n(\lambda_1)\lambda_2 - n(\lambda_2)\lambda_1]} \tag{4.4}$$

Here, " $n(\lambda_1)$ " and " $n(\lambda_2)$ " are "refractive indices in two consecutive maxima (or minima)" and " λ_1 " and " λ_2 " are the "corresponding wavelengths" [14]. The calculated thickness using the above method is given in Table 4.1. These are close to the values evaluated from cross-sectional FESEM images. In the case of the film deposited for 20 minutes, there are only one maxima in the transmittance plot, therefore we were unable to calculate the thickness of this film. But this kind of spectra confirms that the film deposited for 20 minutes is the thinnest film among all the MZF films.

Bandgap: The optical bandgap was calculated by estimating the "absorption coefficient (α)" using the below equation;

$$\alpha = \frac{-1}{d} \left(\ln(T) \right) \tag{4.5}$$

Here, d represents "thickness of the film" and T refers to "transmittance". The "optical band gap (E_g) " was calculated from "Tauc's equation" [15];

$$\alpha h \nu = C \left(h \nu - E_q \right)^m \tag{4.6}$$

Here α and hv are "absorption coefficient" and "energy of incident photon" respectively. The constant C depends on the "transition probability" and the

"exponent m" tells about the "nature of the band transition". m = 1/2 and 3/2 corresponds to "direct allowed and direct forbidden transitions" and m = 2 and 3 corresponds to "indirect allowed and indirect forbidden transitions". The best fit is obtained in the "Tauc's region" for m = 1/2, which is expected for a direct allowed transition. The intersection of linear fits of $(\alpha h v)^{1/m}$ vs. h v plots for m = 1/2 on the x-axis gives direct bandgaps [14-15] as shown in Fig. 4.9, 4.10, and 4.11 for all the different films. The calculated optical bandgap varies in the range of 2.6 to 3.1 eV as tabulated in Table 4.1. The obtained values of the optical bandgap are in agreement with our earlier reports [3-4]. The optical bandgap relies on the "grain size" and "chemical composition" of the film. As the grain size increases, the bandgap of the material decreases. The less variation in the bandgap of the present films is due to similar composition and less change in the average grain size.

Refractive index: The "refractive index (n)" is the material's inherent parameter and it was calculated using eq. 4.2.

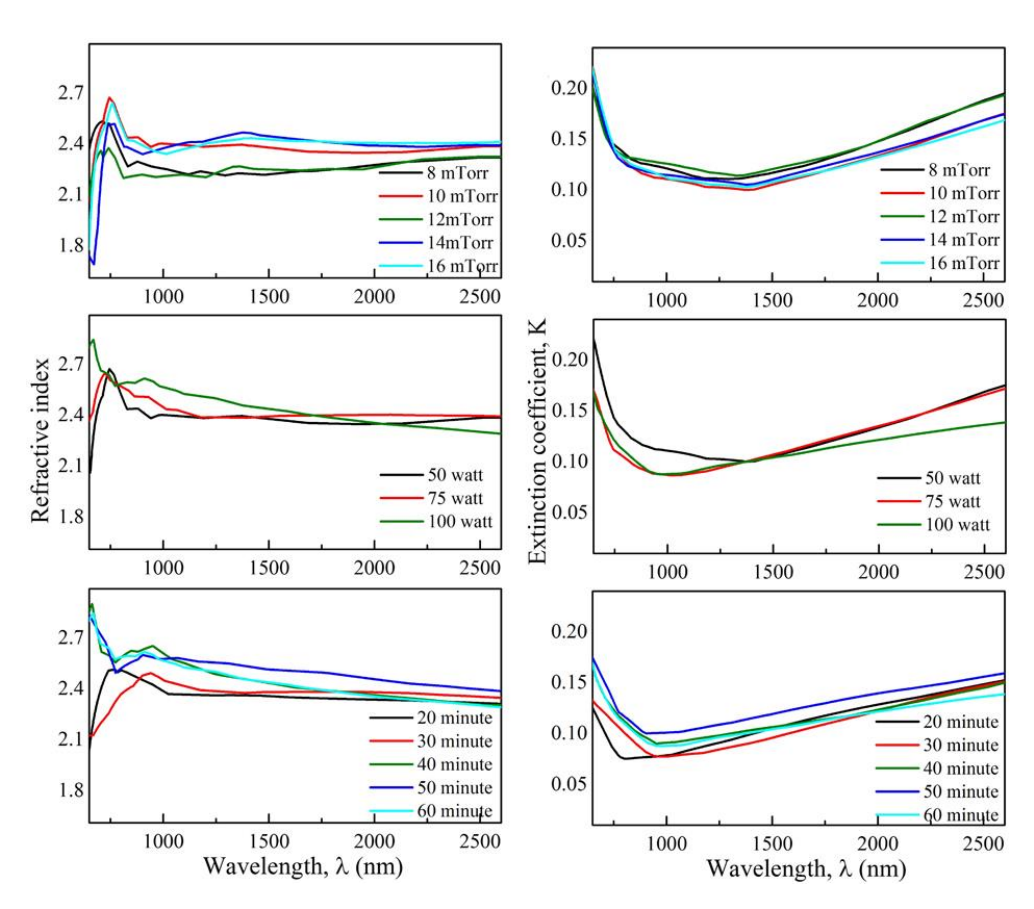


Figure 4.12. The refractive index and extinction coefficient vs. wavelength plots of the different MZF films.

The dependence of the "refractive index" and "extinction coefficient (K)" on the wavelength (λ) of the MZF thin-films deposited under different conditions are shown in Fig. 4.12. The estimated "refractive index" of MZF films is in the range of 1.7 to 2.8 and it saturates at higher wavelengths. A decrease in the refractive index at a higher wavelength is due to normal dispersion. The observed fringes at lower wavelengths are due to interference between the waves of incident electromagnetic radiation and electrons in the material.

The value of K was determined by the following relation;

$$K = \frac{\alpha \lambda}{4\pi} \tag{4.7}$$

Here α represents the "absorption coefficient" and λ denotes the "incident photon wavelength". The estimated "extinction coefficient" of MZF films is in the range of 0.07 to 0.23. K tells about the light lost because of the absorption and scattering at the grain boundaries. Therefore, the observed low value of K indicates the good surface smoothness of the MZF thin-films [15]. Also, K is nearly constant in the higher wavelength region.

4.6 Magnetization Study of MZF films

The study of microstructurally influenced magnetization behavior is important in the realization of planar ferrite devices [16]. Therefore, detailed field dependence magnetization is investigated in parallel and perpendicular directions at 300 K for the MZF thin films deposited under different conditions. The magnetic field dependent hysteresis loop tells about the behavior of the material whether they are ferromagnetic, paramagnetic or superparamagnetic. Whereas, the coercivity of the magnetic hysteresis loop is directly connected to the nature of the ferrite (i.e. soft and hard ferrite) [17].

Fig. 4.13, 4.14, and 4.15 shows M(H) plots in parallel ($\theta = 0^{\circ}$) and perpendicular ($\theta = 0^{\circ}$) orientation of MZF films deposited under different conditions. Here, the angle between the external magnetic field and film plane is denoted as θ . A well-defined hysteresis loop for all the MZF thin film indicates the existence of ferrimagnetic ordering in the film with strong magnetic anisotropy for all the samples. The saturation magnetization, M_s , is estimated from the intercept on the y-axis by

extrapolating the straight line drawn on M vs. H plots. For all the as-deposited films, the magnetization curves are saturating in $\theta = 0^{\circ}$ configuration whereas for $\theta = 90^{\circ}$ saturation is not observed. This shows that higher applied magnetic fields are required to get saturation in the perpendicular direction [18]. This is attributed to the preferred orientation of magnetic clusters present in the as-grown film along with an easy axis of magnetization.

For the MZF films, saturation in magnetization is happening at $\theta = 0^{\circ}$ configuration, therefore we can say that the easy axis of magnetization lies parallel to the film and the hard axis of magnetization lies perpendicular to the film plane. The strong angular dependence of M(H) plots confirms the presence of magnetic anisotropy in the MZF films. This can be attributed to the uniaxial anisotropy induced during deposition. A similar trend is reported in our earlier reports [3-4].

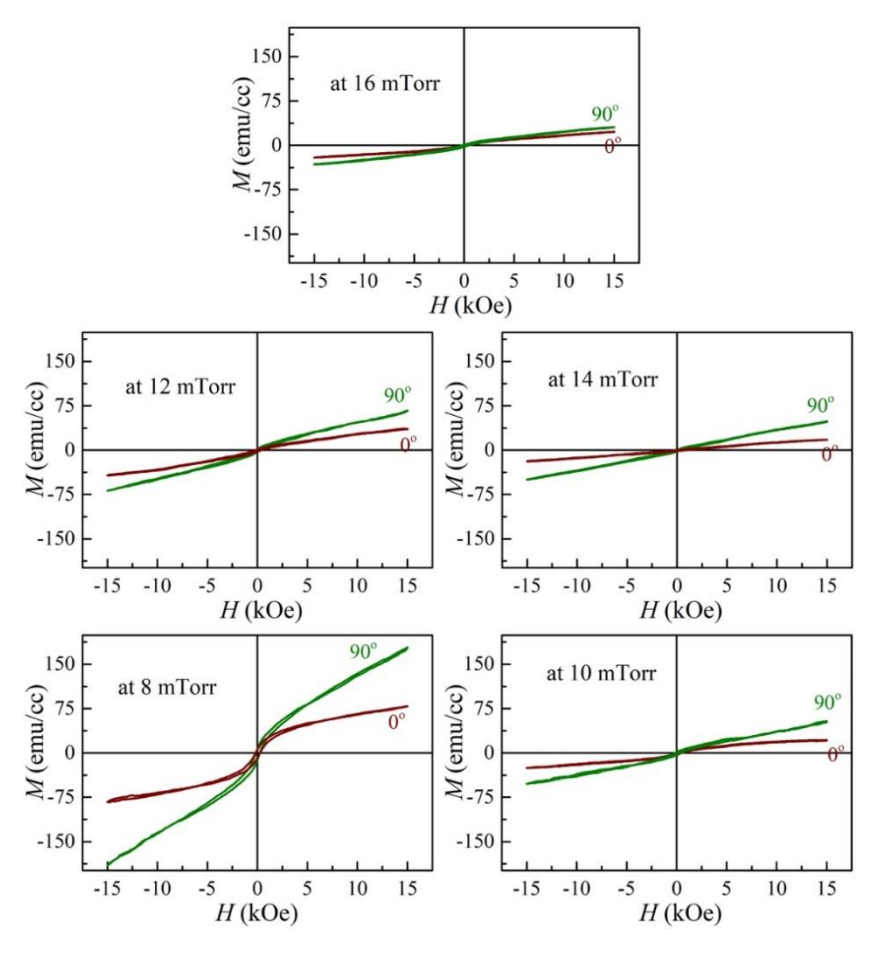


Figure 4.13. Angle dependent M(H) plots of MZF films deposited under different argon pressure.

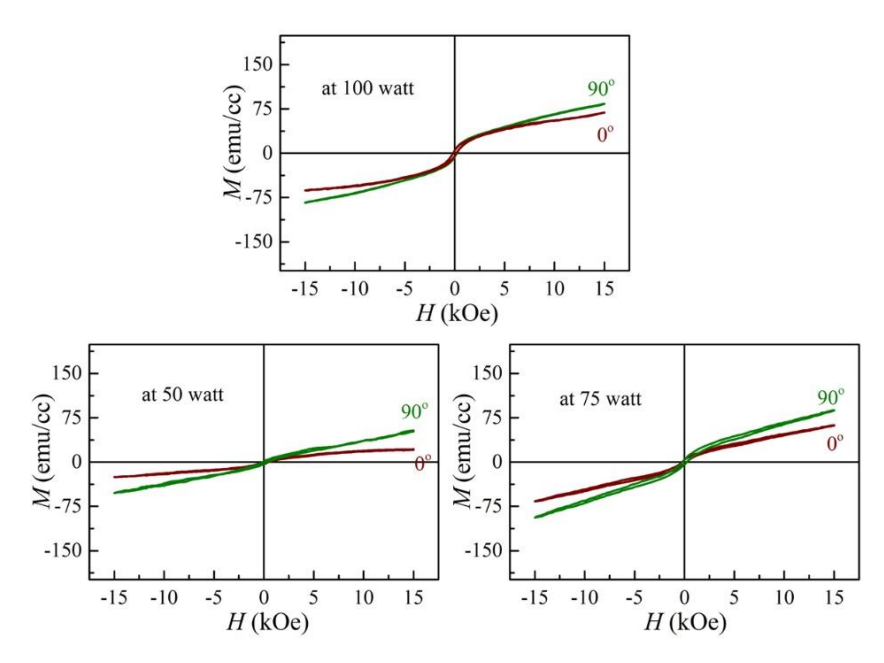


Figure 4.14. Angle dependent M(H) plots of MZF films deposited at different RF power.

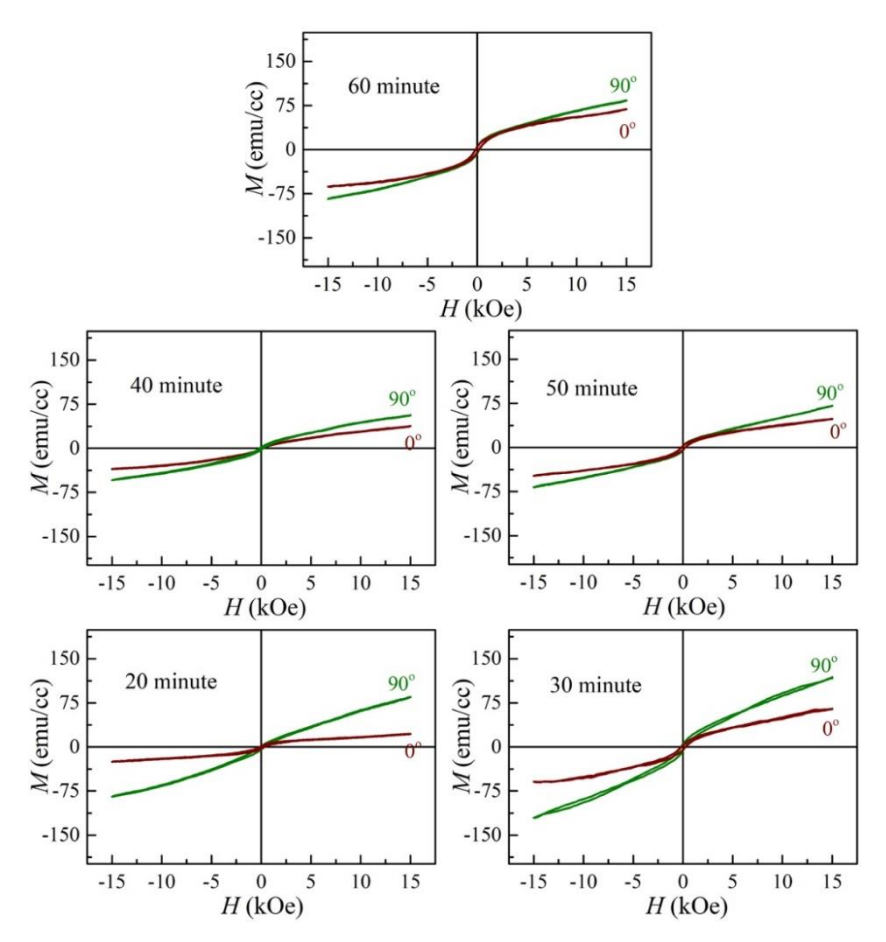


Figure 4.15. Angle dependent M(H) plots of MZF films deposited for different duration.

The saturation magnetization (M_s) , coercivity (H_c) , and remanence magnetization (M_r) of all the MZF films are listed in Table 4.2. The magnetic parameters are showing oscillatory behavior as shown in Fig. 4.16. This non-systematic behavior of the magnetic parameters is correlated with the oscillatory trend of crystallite size as evaluated from XRD and FESEM analysis.

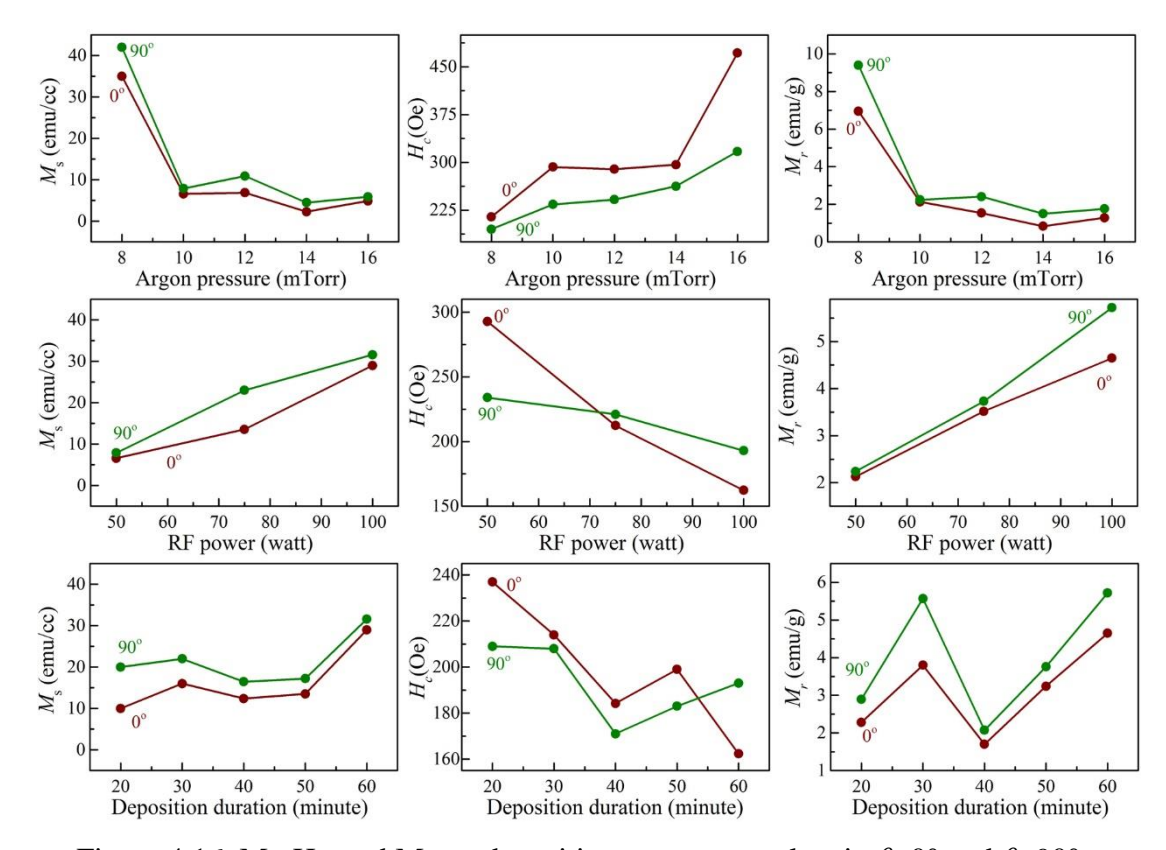


Figure 4.16. M_s , H_c , and M_r vs. deposition parameters plots in θ =0° and θ =90° configuration for MZF films at 300 K.

Also, the M_s-values show some increment with increasing RF power and deposition duration due to an increase in the film thickness. But in case of high argon gas pressure, M_s-values are decreased which may be due to the more amorphous nature of these films. The H_c-values of MZF films strongly depend on microstructural factors such as grain boundaries, surface roughness and interface of the film, etc. [2]. The grain boundaries create pinning centers in the magnetic domain walls due to the defects formed during film deposition [1]. Therefore the variation in coercivity can be related to the different microstructure of the MZF films [19-21].

Table 4.2. "Magnetic parameters" of the MZF films deposited under different conditions.

Deposition	Film thickness	Magnetic parameters at 300 K							
parameter	(nm)	M _s (emu/cc)		H _c ((Oe)	M _r (emu/cc)			
	(FESEM)	0°	90°	0°	90°	0°	90°		
Deposited at various argon pressure at 50 Watt for 60 minutes.									
8 mTorr	315	35	42	214	195	6.9	9.4		
10 mTorr	350	7	8	292	234	2.1	2.2		
12 mTorr	380	7	11	289	242	1.5	2.4		
14 mTorr	487	2	5	289	262	0.8	1.5		
16 mTorr	445	5	6	472	317	1.3	1.8		
Deposited in an argon gas pressure of 10 mTorr for 60 minutes at various RF									
power.									
50 watt	354	7	8	293	234	2.1	2.2		
75 watt	459	14	23	212	215	3.5	3.7		
100 watt	560	29	32	162	193	4.7	5.7		
Deposited in an argon gas pressure of 10 mTorr at 100 Watt for different duration.									
20 minute	243	10	20	237	209	2.3	2.9		
30 minute	300	18	29	214	208	3.8	5.6		
40 minute	456	12	17	184	171	1.7	2.1		
50 minute	500	14	17	199	183	3.2	3.8		
60 minute	560	29	32	162	193	4.7	5.7		

4.7 FMR Study of the MZF films

Ferromagnetic resonance (FMR) spectroscopy is a useful technique to study the magnetic anisotropies at the atomic level present in thin films due to the structural inhomogeneity [4], [22-24]. In ferromagnetic/ferrimagnetic samples, the ferromagnetic resonance changes according to the internal field of the samples. The out of plane angular dependence of the FMR spectra were recorded at a different angle (θ) between the applied magnetic field and film plane for all the MZF films.

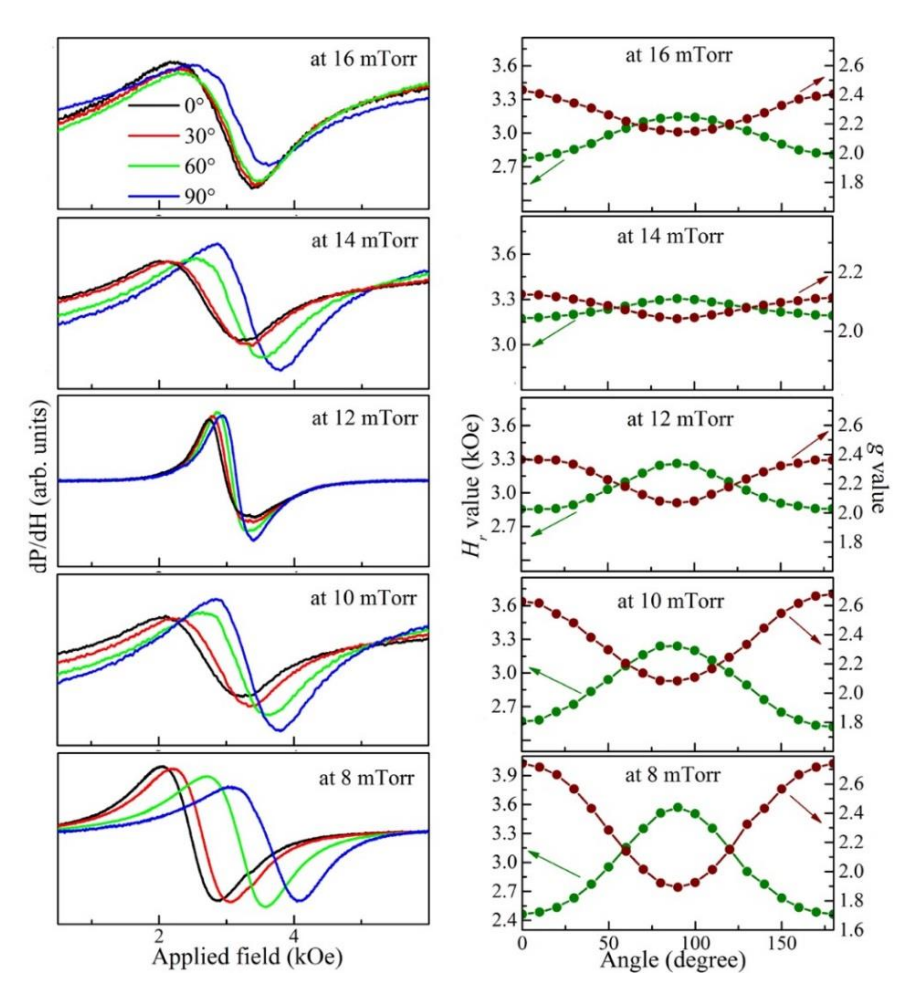


Figure 4.17. The FMR spectra, H_r vs. θ and g-value vs. θ plots at 300 K of the MZF film deposited under different argon gas pressure.

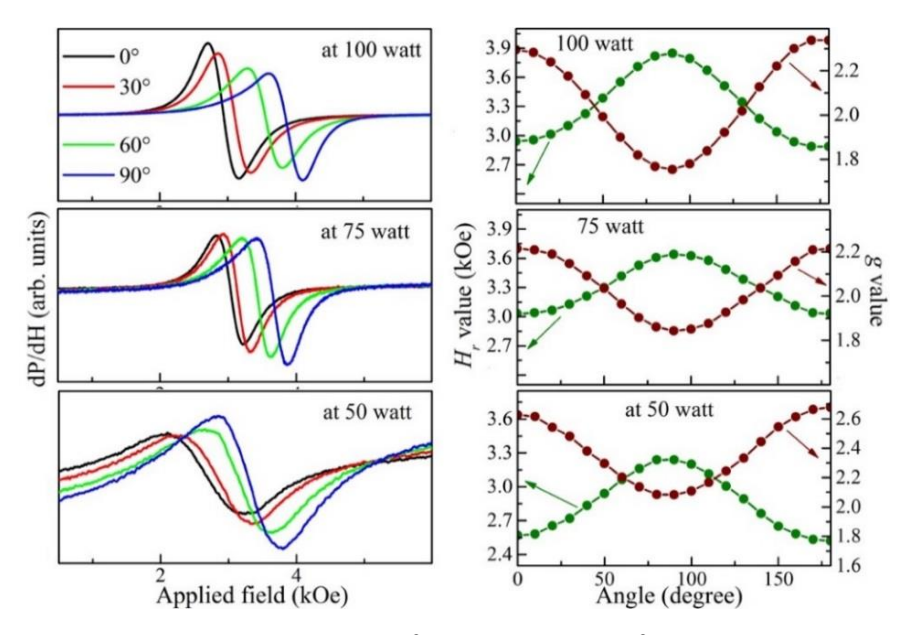


Figure 4.18. The FMR spectra, H_r vs. θ and g-value vs. θ plots at 300 K of the MZF film deposited at different RF power.

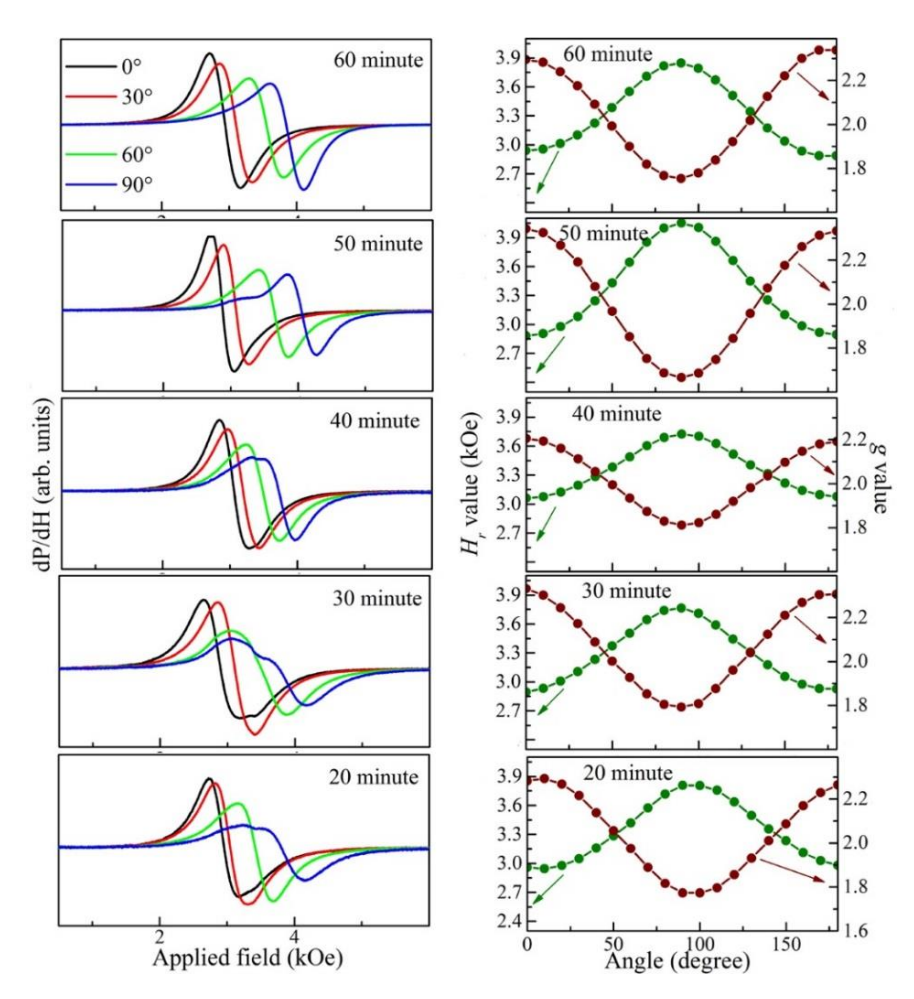


Figure 4.19. The FMR spectra, H_r vs. θ and g-value vs. θ plots at 300 K of the MZF film deposited for the different duration.

Fig 4.17, 4.18, and 4.19 show the derivative of microwave absorption (dP/dH) vs. applied magnetic field (FMR spectra) in $\theta = 0$, 30, 60 and 90° orientations at 300 K of the MZF films deposited under different conditions. For all the samples, FMR spectra shift towards higher fields and the resonance field (Hr) increases as θ changes from 0 to 90° at 300 K. The change of H_r -value is directly connected to the internal field of the ferromagnetic/ferrimagnetic sample. The increase in H_r -value is related to the decrease in the internal magnetic field of the sample which indicates the decrease in the ferrimagnetic interaction in the MZF film with angle θ .

Further, the strong angular dependence of the FMR spectra reveals the presence of the uniaxial anisotropy created in the film during deposition [4], [22-24]. The film possesses anisotropy in the system due to the several factors such as geometrical shape anisotropy of the grains, internal stresses and orientation of atoms/ions during the growth process of the film, etc. [25]. In other words, the magnetic anisotropy of the film is related to the variation in the microstructure with the film orientation which comes from the shape anisotropy. The produced strain due to the lattice mismatch affects the magnetic properties of the MZF films. For the MZF films, the FMR signal becomes slightly asymmetric, broad and progressively splits into two unresolved peaks as the angle θ increases from 0 to 90° due to the presence of out-of-plane magnetic anisotropy in the MZF films. The FMR spectra of some of the MZF films have one shoulder peak (multiple resonances) at 90°. The occurrence of multiple resonances can be attributed to more than one magnetic interaction (magnetic phases) present in the MZF films. Also, it indicates the axial anisotropy due to structural disorders present in the films [26-27]. The peak broadening in the FMR spectrum in $\theta = 90^{\circ}$ configuration is attributed to the removal of preferred orientation of magnetic clusters and creating randomly oriented clusters (increased disorder) in the MZF films in the perpendicular orientation similar to the magnetization results.

Fig. 4.20 shows the change in H_r -value and g-value as a function of the different deposition conditions at $\theta = 0$ and 90° for all the MZF films. FMR parameters vs. deposition condition plots are not following systematic trends due to the oscillatory nature of the size of crystallite present in the MZF films. The FMR parameters of the as-deposited MZF thin film for both parallel and perpendicular configurations are listed in Table 4.3.

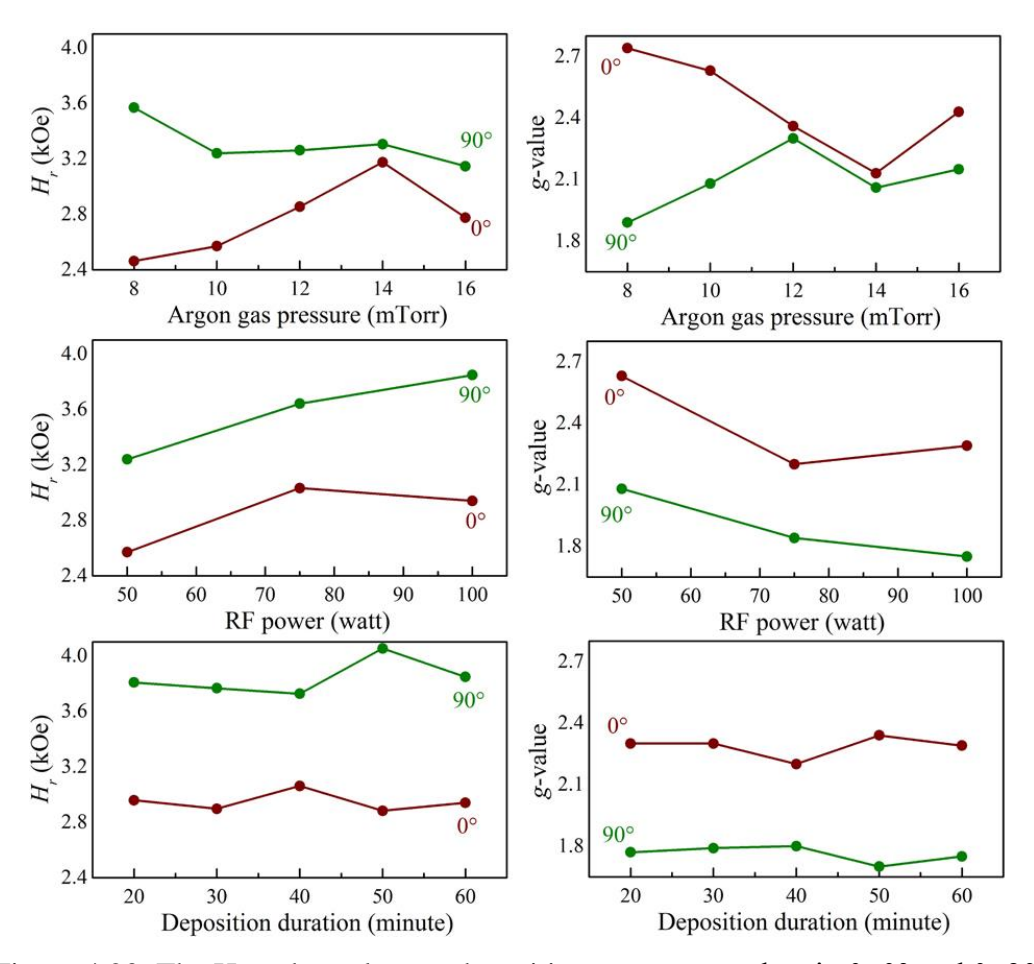


Figure 4.20. The H_r and g-value vs. deposition parameters plots in θ =0° and θ =90° configuration for MZF films at 300 K.

Further, "Kittel's equation" [28] was used to calculate the "perpendicular magnetic anisotropy field" (H_K);

For out of plane configuration,

$$\left(\frac{\omega}{\gamma}\right) = H_{\perp} - 4\pi M_{eff} \tag{4.8}$$

and for in-plane configuration,

$$\left(\frac{\omega}{\gamma}\right)^2 = H_{\parallel} \left(H_{\parallel} + 4\pi M_{eff}\right) \tag{4.9}$$

Here, H_1 and H_2 are the "resonance field in parallel and perpendicular geometries" respectively. The "applied wave frequency" is denoted as ω and M_{eff} is the "effective magnetization" and γ represents the "gyromagnetic ratio". Effective magnetization and H_r -value depend on the internal field. The effective magnetization gives a major

contribution to the perpendicular anisotropy. The following equation was used to calculate the perpendicular anisotropy in the films.

$$H_K = 4\pi M_S - 4\pi M_{eff} (4.10)$$

Here,

$$H_K = \frac{2K}{M_S}$$

 H_k is the "perpendicular anisotropy field" and K represents the "first-order perpendicular anisotropy energy per unit volume". The "saturation magnetization (M_s) " was estimated from the M(H) plots. The obtained H_K -values and K values are listed in Table 4.3 [29-30]. The perpendicular uniaxial anisotropy energy (K) that controls the spin alignment in the thin films. The oscillatory variation in H_K and K values also support the magnetization results.

Table 4.3. "FMR parameters" of the MZF thin films deposited under different deposition conditions.

Deposition	Film	FMR p	arame	eters at 300 l	$H_{\rm K}$ -value	<i>K</i> -value		
parameter	thickness (nm)				(Oe)	(erg/cm ³)		
	(FESEM)	0° 90°						
		H _r (kOe)	g	H _r (kOe)	g			
Deposited under different argon gas pressure at 50 Watt for 60 minutes.								
8 mTorr	315	2.4	2.7	3.5	1.9	-223	-4678	
10 mTorr	350	2.6	2.6	3.2	2	-304	-1217	
12 mTorr	380	2.9	2.4	3.2	2.3	-63	-346	
14 mTorr	487	3.2	2.1	3.3	2.1	-4	-10	
16 mTorr	445	2.8	2.4	3.1	2.2	-126	-377	
Deposited in an argon gas pressure of 10 mTorr for 60 minutes at various RF							rious RF	
	power.							
50 watt	354	2.6	2.6	3.2	2	-304	-1217	
75 watt	459	3.0	2.2	3.6	1.8	-116	-1327	
100 watt	560	2.9	2.3	3.8	1.8	-208	-3324	
Deposited in an argon gas pressure of 10 mTorr at 100 Watt for different duration.								
20 minute	243	3.0	2.3	3.8	1.8	-290	-2895	
30 minute	300	2.9	2.3	3.7	1.8	-176	-2563	
40 minute	456	3.1	2.2	3.7	1.8	-190	-1620	
50 minute	500	2.9	2.3	4.0	1.7	-534	-4539	
60 minute	560	2.9	2.3	3.8	1.8	-208	-3324	

4.8 Chapter Summary

The MZF thin films were fabricated by RF-magnetron sputtering on quartz substrates under different deposition conditions. The detailed study of the structure, optical bandgap, magnetization and FMR for the as-deposited films was undertaken. The XRD pattern shows weak peaks corresponding to the cubic spinel structure of the target. The FESEM micrographs show the small nano-cluster formation with columnar growth in all the MZF films. The magnetization versus field plots reveals the soft ferrimagnetic behavior of the MZF films. Strong angular dependence of the M-H curves confirms the presence of magnetic anisotropy in the MZF films. The resonance field in the FMR spectra shifts towards the higher magnetic field when the angle between the applied field and film plane is changed from 0 to 90°. Hence the FMR analysis also indicates the existence of magnetic anisotropy in the MZF films similar to the magnetization results. These results confirm that the magnetic and optical parameters of the prepared thin films are related to the crystallographic parameters and deposition conditions.

References

- 1. J. R. Sun, Z. G. Wang, Y. Y. Wang, C. F. Yao, K. F. Wei, T. L. Shen and F. S. Li, *Advanced Materials Research* **213**, 325-329 (2011).
- 2. F. Li, J. R. Sun, X. Wang, and J. Wang, *IEICE Trans. Electron.* **E90–C**, 1561-1564 (2007).
- 3. A. Farheen and R. Singh, *Material research express* **6** (2019).
- 4. A. Farheen and R. Singh, J. Superconductivity and Novel Magnetism 32 (2019).
- 5. B. D. Cullity and C. D. Graham, *Introduction to magnetic materials*, Wiley: John Wiley & Sons publications, Inc., Hoboken, New Jersey, 505-515 (2009).
- 6. K. H. J. Buschow, G. J. Long and F. Grandjean, *High Density Digital Recording*, Springer Science & Business Media, 429-444 (2012).
 - 7. A. Farheen and R. Singh, AIP Conference Proceedings 1953, 120067 (2018).
- 8. M. Farooq, *J. Korean Physical Society* **40**, 511 (2002).
- 9. B. D. Cullity, *Elements of X-ray diffraction*, Second Edition, Addison-Wesley Publishing Company Inc., United States of America, 32-85 (1978).
- 10. R. F. Soohoo, Magnetic Thin Films (New York: Harper & Row), 119 (1965).
- 11. F. Yakuphanoglu Yakuphano, M. Sekerci and A. Balaban, *Opt. Mater.* **27**, 1369–72 (2005).
- 12. M. Suchea, S. Christoulakis, M. Katharakis, N. Vidakis and E. Koudoumas, *Thin Solid Films* **517**, 4303–6 (2009).
- 13. R. J. Swanepoel, *J. Phys. E: Sci. Instrum.* **16**, 1214 (1983).
- 14. M. Sultan and R. Singh, *J. Appl. Phys.* **105** 07A512 (2009).
- 15. J. Tauc, Amorphous and Liquid Semiconductors. Springer, Berlin (1974).
- 16. O. F. Caltun, J. Optoelectronics and Advanced Materials 6, 935–938 (2004).
- 17. P. K. Manna, S. M. Yusuf, M. Basu and T. Pal, *J. Physics: Condensed Matter.* **23**, 506004 (2011).
- 18. K. Khazen and et al., *Physical Review B* **74**, 245330 (2006).
- J. P. Chen, C. M. Sorensen, K. J. Klabunde, G. C. Hadjipanayis, E. Delvin, and A. Kostikas, *Phys. Rev. B* 54, 9288–9296 (1996).

- M. Pal, P. Brahma, D. Chakravorty, D. Bhattacharyya, and H.S. Maiti, *J. Magn. Magn. Mater.* 164, 256–260 (1996).
- 21. J. M. D. Coey, Phys. Rev. Lett. 27, 1140–1142 (1971).
- 22. J. Kaur, G. Thirupathi and R. Singh, *J. Superconductivity and Novel Magnetism* **30**, 2615-2620 (2017).
- 23. J. Kaur, G. Thirupathi and R. Singh, *AIP Advances* **6**, 055906 (2016).
- 24. R. Singh and S. Saipriya, *FMR Studies of [SnO2/Cu-Zn Ferrite] Multilayers: Ferromagnetic Resonance Theory and Applications*, Dr. O. Yalcin (Editor), InTech, Europe (2013).
- 25. M. Sultan and R. Singh, *J. Physics D: Applied Physics* **42**, 115306 (2009).
- 26. D. S. Schmool, and et al., *J. Optoelectronics and Advanced Materials* **6**, 541–550 (2004).
- 27. J. Pelzl, R. Meckenstock, D. Spoddig, F. Schreiber, J. Pflaum and Z. Frait, *J. Physics: Condensed Matter* **15**, S541 (2003).
- 28. C. Kittel, Phys. Rev. 73 (1948).
- 29. X. Zuo, A. Yang, S. D. Yoon, J. A. Christodoulides, V. G. Harris and C. Vittoria, J. Appl. Phys. Lett. 87, 1-4 (2005).
- 30. M. Belmeguenai, F. Zighem, G. Woltersdorf, Y. Roussigné, S.M. Chérif, K. Westerholt, and G. Bayreuther, *J. Magn. Magn. Mater.* **321**, 750-753 (2009).

Chapter 5

Structural, magnetic and electrical properties of $Mn_{0.5}Zn_{0.5}Fe_2O_4$ - $BaTiO_3$ composites

This chapter contains an introduction of the composite multiferroic. Further, we have discussed their structural, magnetic and ferroelectric properties.

5.1 Composite multiferroic

The simultaneous existence of ferroelectricity and magnetic ordering in multiferroic materials is gaining special interest due to their promising applications in various multifunctional devices [1-2]. In general, a combination of both ferroelectric (FE) and ferrimagnetic (FM) phases may lead to novel functionalities that are not present in either state alone as demonstrated in Fig. 5.1. Therefore, the composites are essential for the development of magneto-electronic devices in different frequency regions [1], [2-7].

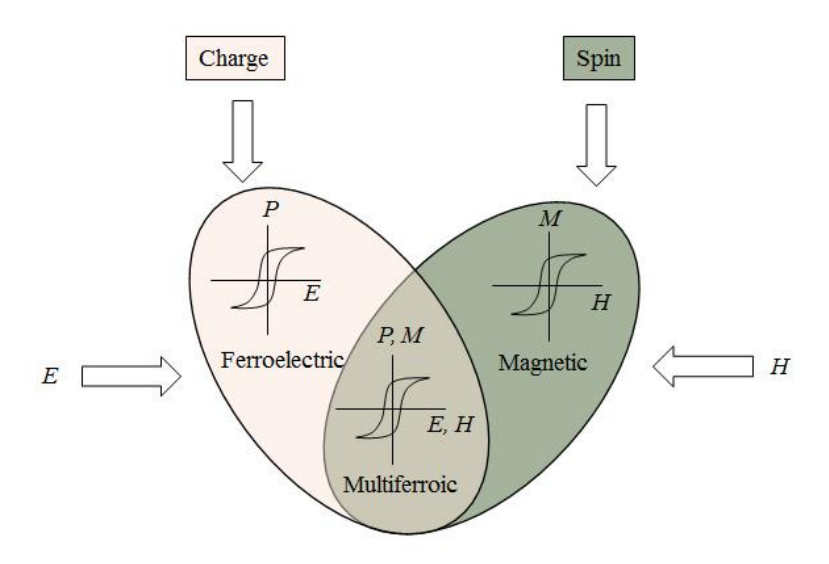


Figure 5.1. Graphical demonstration of the magnetic-ferroelectric multiferroic composite.

Moreover, the single-phase multiferroic systems are rare in nature which leads to the necessity of the preparation of FM-FE composite materials [8-15]. The magneto-electric behavior of FM-FE composites is due to the magnetic-mechanical-electric interaction between the FM and FE sublattices. In other words, the product of magnetostriction and piezoelectric effect in their respective phase causes a magneto-electric effect [9]. To get higher magneto-electric coupling: high magnetostriction, good piezoelectric coefficient and strong mechanical interaction between the phases are required. [4], [12]. Hence, for the preparation of the multiferroic composite, we have chosen the Mn-Zn ferrite as ferrimagnetic and BaTiO₃ (BTO) as the ferroelectric component due to their fascinating magnetostriction and piezoelectric properties, respectively [16-18]. BTO has a "perovskite structure" with lattice constants "a = 3.994 Å" and "c = 4.033 Å (XRD PDF) pack No. 831880"). Whereas, Mn_{0.5}Zn_{0.5}Fe₂O₄ (ZMF) has a "cubic spinel structure" with lattice constant "a = 8.453 Å (XRD PDF pack No. 7423398"). Almost double value of the lattice parameter of ZMF than BTO insures the well interface matching between ferrite and ferroelectric phase [17], [19]. Moreover, the good interface matching is important for the efficient interface coupling between ZMF and BTO. The strong coupling between ZMF and BTO grains improves the magnetoelectric effect. In particular, the optimization of ferrite percentage is crucial because their resistivity is not good enough to use for high voltage. Since higher ferrite content may lead to a significant decrease in the electrical properties of the composite, therefore we have used only up to 20% of ferrite [17], [19].

In order to prepare composite, ZMF and BTO were used as a base material [20-22]. The composites of composition (1-x) BaTiO₃ + (x) Mn_{0.5}Zn_{0.5}Fe₂O₄ (x=0, 0.05, 0.10, 0.15, 0.20 and 1) were synthesized via solid-state route. The disc-shaped sintered pellets were coated with silver paste on both sides for making electrodes, which gives the metal-insulator-metal structure to the pellets which are ready for electrical measurements. Pure ZMF and BTO nanoparticles were also sintered in the pellet form under the similar conditions for reference. The structural and morphological properties of base material and composite were well investigated. The magnetization and electrical measurements

of $Mn_{0.5}Zn_{0.5}Fe_2O_4$ – $BaTiO_3$ composites were studied to confirm the multiferroic behavior of the prepared composites with different ZMF fraction.

5.2 Structural study of composites

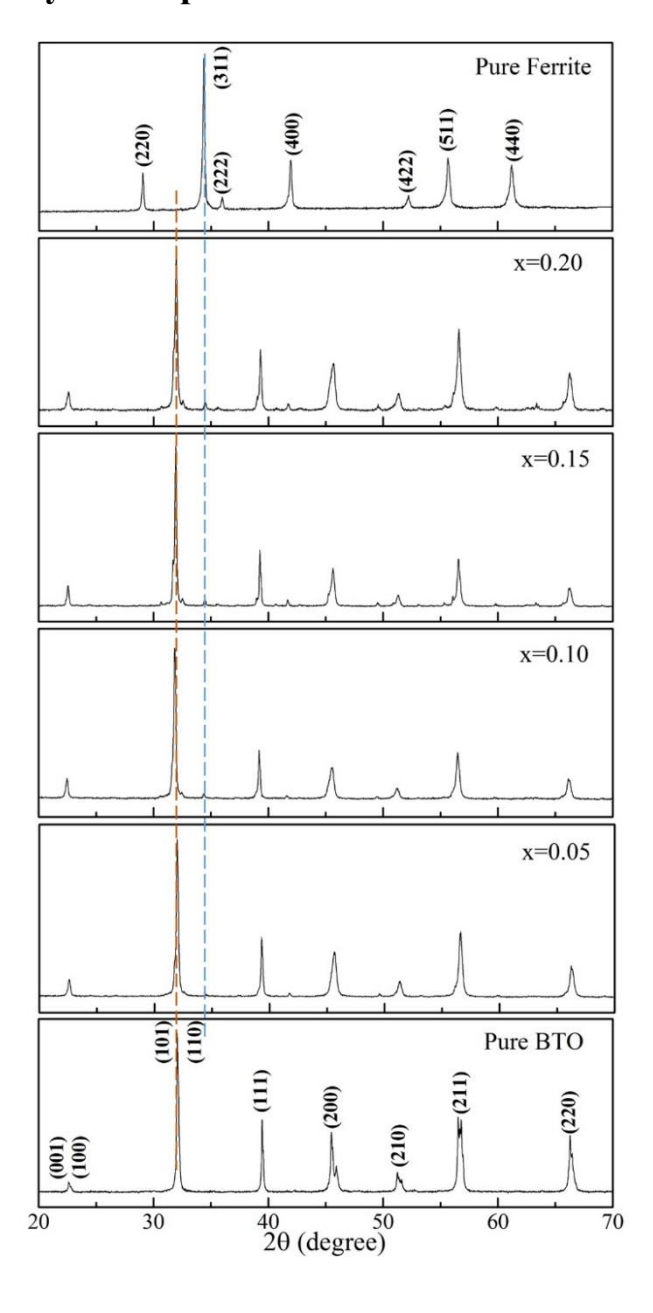


Figure 5.2. XRD pattern of FM-FE composites and base materials.

Fig. 5.2 depicts the XRD pattern of ZMF, BTO and composites samples. The red dotted line represents BTO's main peak whereas the blue dotted line represents ZMF's main peak.

The crystal structure of pure ZMF is a "cubic spinel with Fd-3m space group" whereas for pure BTO the structure is "tetragonal with P4mm space group" as confirmed from XRD analysis reported in the earlier work [17], [22-23]. Moreover, splitting of the XRD peaks at a higher angle also ensures the tetragonal structure of pure BTO [24]. All the peaks depicted in the XRD pattern of the composites are associated to the ZMF and BTO phases with no other detectable third phase. Any chemical reaction between the ZMF and BTO phases degrades their magnetic and electric properties. But the XRD analysis ensures that the BTO and ZMF phases are in co-existence in the composite samples without any chemical reaction between them during sintering. The average crystallite size and lattice parameters were calculated using Scherrer's formula and Bragg's law as we have discussed in chapter 4 [25-26].

Table 5.1. "Crystallographic parameters" for composites and base materials.

Sample	X	Lattice constant (Å)		Average	Unit cell	c/a
				crystallite	volume	
				size (nm)	(\mathring{A}^3)	
BTO	0	a=b=3.95, c=4.07		55	64	1.03
(0.95)BTO+(0.05)ZMF	0.05	BTO	a=b=3.97, c=4.05	47	64	1.02
		ZMF	a=b=c=8.59	46	636	
(0.9)BTO+(0.10)ZMF	0.10	BTO	a=b=3.98, c=4.03	49	64	1.01
		ZMF	a=b=c=8.64	49	645	
(0.85)BTO+(0.15)ZMF	0.15	BTO	a=b=3.97, c=4.04	56	64	1.01
		ZMF	a=b=c=8.62	50	640	
(0.8)BTO+(0.2)ZMF	0.20	BTO	a=b=3.97, c=4.04	50	64	1.02
		ZMF	a=b=c=8.61	50	640	
ZMF	1		a=b=c=8.65	53	645	_

The estimated "average crystallite size" and "lattice parameters" of all the composites are tabulated in Table 5.1. The calculated "average crystallite size" and "lattice parameters" of the composite samples are in agreement with the lattice parameters of the base material when present as particular phases as shown in Table 5.1. The intensity of

major peaks, (101) for BTO and (311) for ZMF represent the percentages of the particular phase present in the composite. The intensity of (101) peak is more than the (311) peak because ferrite percentage is low in the composites.

5.3 Morphological study of composites

The FESEM images of the composites and base materials are shown in Fig. 5.3. Two kinds of grains are present in the composite samples in which one corresponds to ZMF grains while the second one corresponds to the BTO grains.

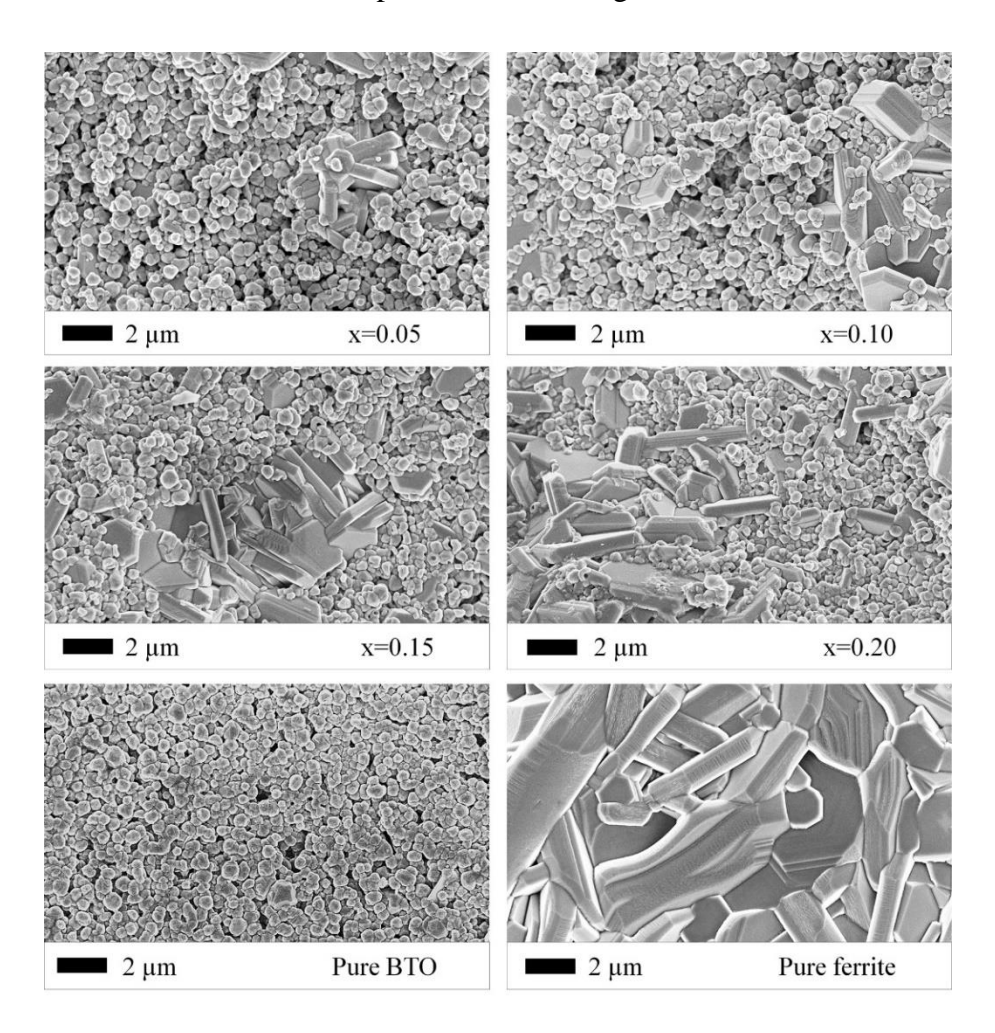


Figure 5.3. FESEM micrographs of different FM-FE composites and base material.

The observed non-uniform distribution of ZMF and BTO grains is due to the different growth rates of ZMF and BTO in composites [21]. The observed clear boundaries between the ZMF and BTO grains ensures that there is no chemical reaction between the two phases similar to the XRD results. The small spherical particles correspond to BTO whereas the disc-shaped bigger particles correspond to ZMF as confirmed from EDAX.

5.4 Magnetization study of composites

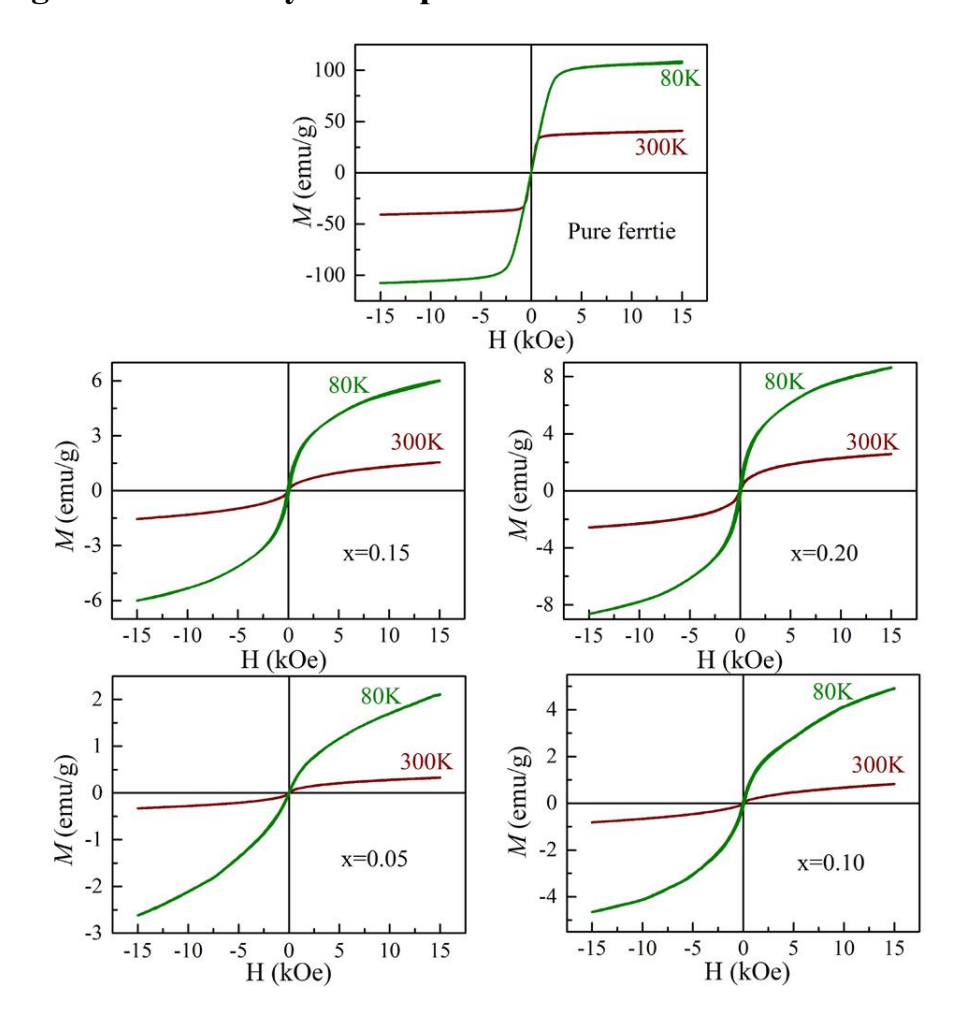


Figure 5.4. The M(H) plots at 300 and 80 K for FM-FE composites and pure ferrite.

Fig. 5.4 shows the magnetization vs. magnetic field (M(H)) plots of the ZMF (inset) and composite samples at 300 and 80 K, respectively. The composite samples exhibit soft ferrimagnetic behavior with very low coercivity value. It is expected that the intrinsic

magnetic property of the ferrite phase should not change in the composite with the presence of the FE phase. The simultaneous existence of the FE phase dilutes the magnetic moment due to the reducing amount of the ferrite phase. As expected, the observed magnetization value of composites is less than the ZMF sample because of the dilution of the FM phase with the existence of non-magnetic BTO phase (as shown in the Fig. 5.5) [27]. Since the ferrite (ZMF) grains are in the matrix of ferroelectric material (BTO), therefore ferrite grains are separated by BTO grains. This separation alters the distribution of magnetic ions and their spin orientation, as a result, the magnetic coupling among the ferrite particles are influenced [28]. Further, the magnetization values are higher at 80 K than the values at 300 K due to the ferrimagnetic cluster formation (randomly frozen spin) at low temperatures [22], [27].

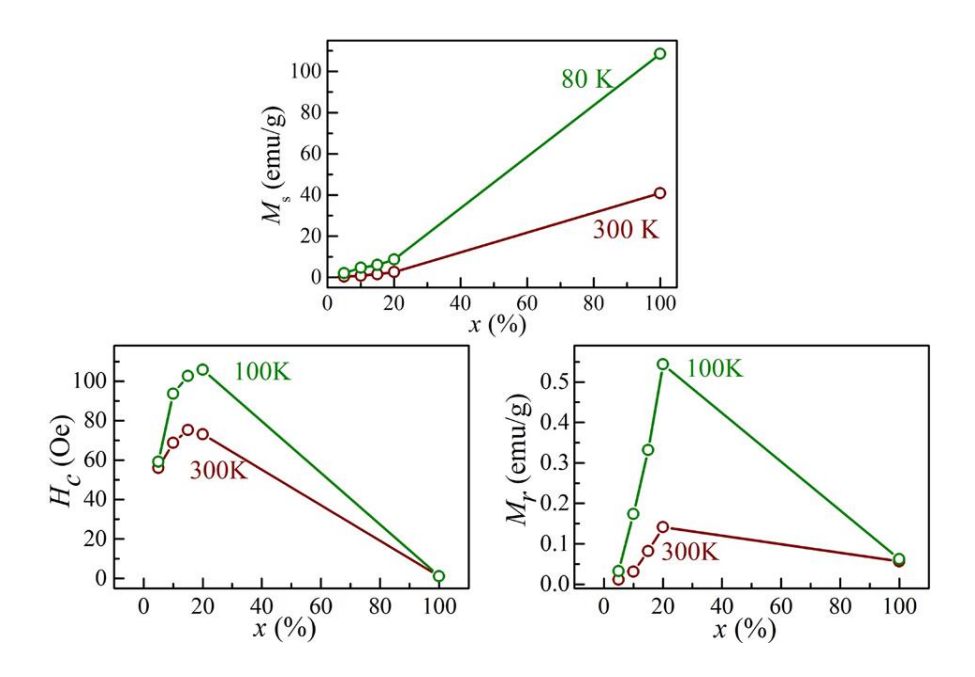


Figure 5.5. The M_s , H_c , and M_r vs. x(%) plot for FM-FE composites and pure ferrite.

Fig. 5.5 depicts the change of "saturation magnetization (M_s)", "coercivity (H_c)", and "remanence magnetization (M_r)" with respect to the ZMF percentage (x %) for all the samples at 300 and 80 K respectively. The gradual increment in M_s -values of composites is observed at 300 and 80 K with an increase of ZMF percentage as expected. This indicates that the M_s -values for the composite samples follow the mixture rule (sum

property) [6] [27]. As we can see, the magnetic response of composites depends on the ZMF percentage [28]. Since the ZMF has a mixed cubic spinel structure, the magnetization nature of ZMF can be explained as cation distribution between octahedral and tetrahedral sublattices [22], [29]. The H_c -values and M_r -values are increasing with an increase in ZMF percentage at 300 and 80 K but have lower values for the pure ferrite. These variations can be attributed to the lattice distortion at the interfaces of ZMF and BTO grains.

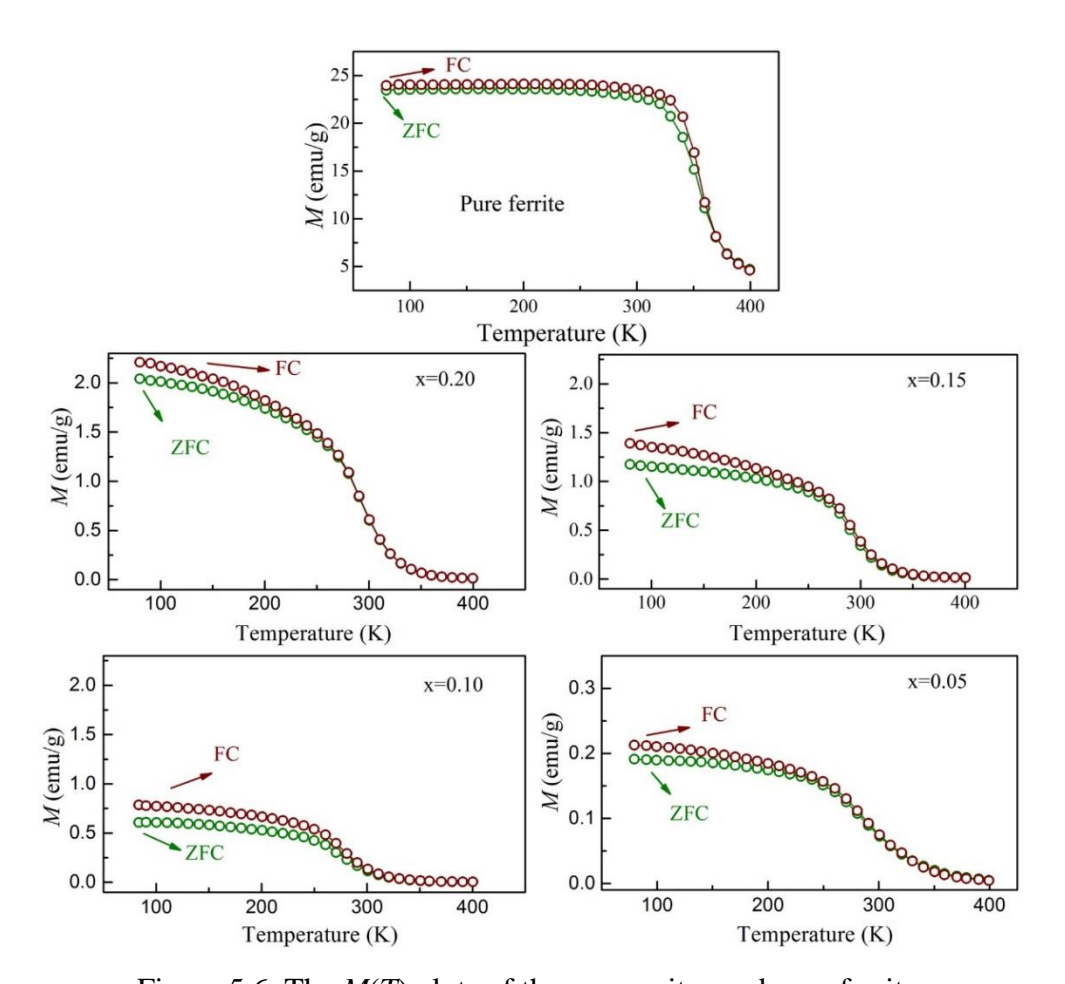


Figure 5.6. The M(T) plots of the composites and pure ferrite.

Fig. 5.6 shows the magnetization vs. temperature (M(T)) plots recorded from 80 to 400 K temperature-range in zero field cooled (ZFC) and field cooled (FC) mode at 500 Oe for the samples. In ZFC mode, first, the samples were cooled up to 80 K in the absence of a magnetic field and then the magnetization was measured at 500 Oe as a function of

temperature. In FC mode, samples were cooled in the field of 500 Oe and then the magnetization measurement was performed as a function of temperature.

Initially, the M(ZFC) increases sharply with decrease in temperature followed by almost saturation with a further decrease in temperature whereas M(FC) continues to rise slowly on decreasing temperature and splits from the ZFC curve which confirms the ferrimagnetic nature of the composites [22]. Moreover, the splitting (bifurcation) of ZFC and FC curves also depends on the applied magnetic field. It is found that the bifurcation temperature is nearly the same for all the composite samples which clear that bifurcation temperature relies on ferrite. An increase in magnetization is observed as indicated by M(T) plots with increasing ZMF percentage. Also, the long-range magnetic order is decreased as compared to pure ZMF due to the ferroelectric phase inclusion in the composite samples [17].

5.5 Electrical study of composites

Since BaTiO₃ is a constituent of multiferroic composite in the present study and it has ferroelectric nature, therefore, dielectric and polarization studies of the composites sample were done. The dielectric property tells about the suitability of the material for various applications whereas polarization loop tells about the multiferroic nature of the composite.

5.5.1 Dielectric study

The response of the material in an electric field provides information about dielectric properties. The variation of the real part of dielectric constant (ϵ ') and dielectric loss (tan δ) of FM-FE composites from 10 Hz to 1 MHz frequency range at room temperature are shown in Fig. 5.7. The FM-FE composites show a decrease in ϵ '-value with an increase in loss with increasing MZF percentage. It is observed that the dielectric constant and loss decreases with increasing frequency and approaches to a lower saturation value at higher frequencies. The variation of ϵ '-value with frequency is attributed to the fact that the electric dipoles are unable to follow the alternating electric field oscillations at higher frequencies.

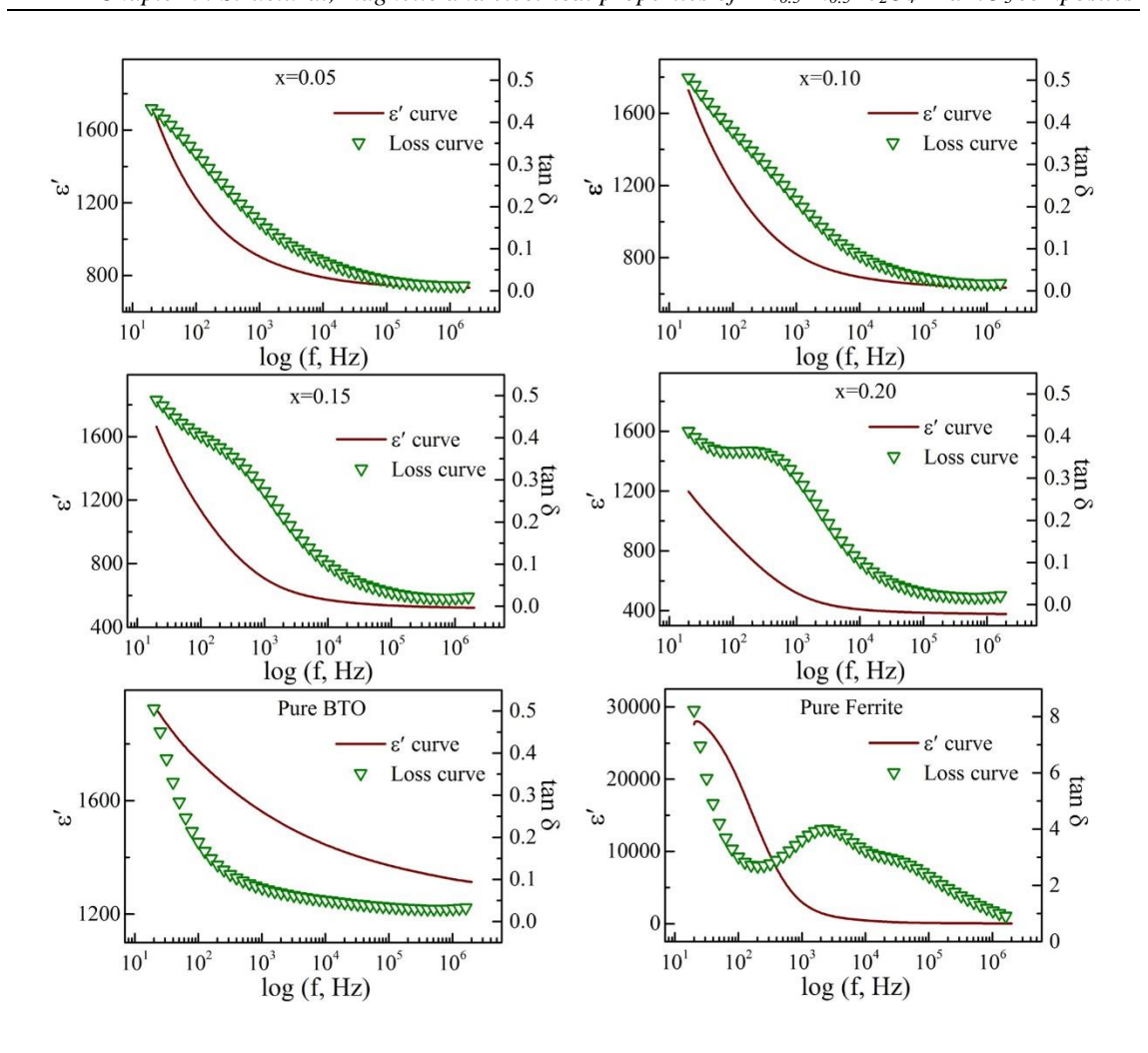


Figure 5.7. The frequency-dependent dielectric constant (ϵ ') and loss (tan δ) plots of the FM-FE composites and base materials.

At lower frequencies, the composites have higher ε' and loss values. The variation of ε' and loss with frequency can be understood by Maxwell–Wagner type interfacial polarization and Koop's phenomenological theory [12], [30]. In other words, at lower frequencies the high value of ε' is due to the space charge polarization and interfacial polarization which is attributed to the heterogeneity of the FM-FE composites. Since in the composites, the ferroelectric grains are surrounded by the ferrite grains or vice versa, the FM-FE phase distribution makes two types of inter grain connectivity which imply two types of ionic relaxations in the low-frequency region as confirmed from the FESEM micrographs (Fig. 5.3) [21], [31]. The loss curve shows more abnormal behavior with

increasing ZMF fraction which may be due to different valence states of iron ions in the composites caused by high sintering temperature.

Further, the electric modulus analysis is also used to interpret the electrical response of materials. The complex electric modulus (M*) is defined as M*=1/ ϵ * where ϵ * is the complex dielectric constant. The real part of electric modulus (M') (Fig 5.8) saturates at high frequency and tends to attain zero value at low frequency indicating the negligible presence of electrode polarization [15].

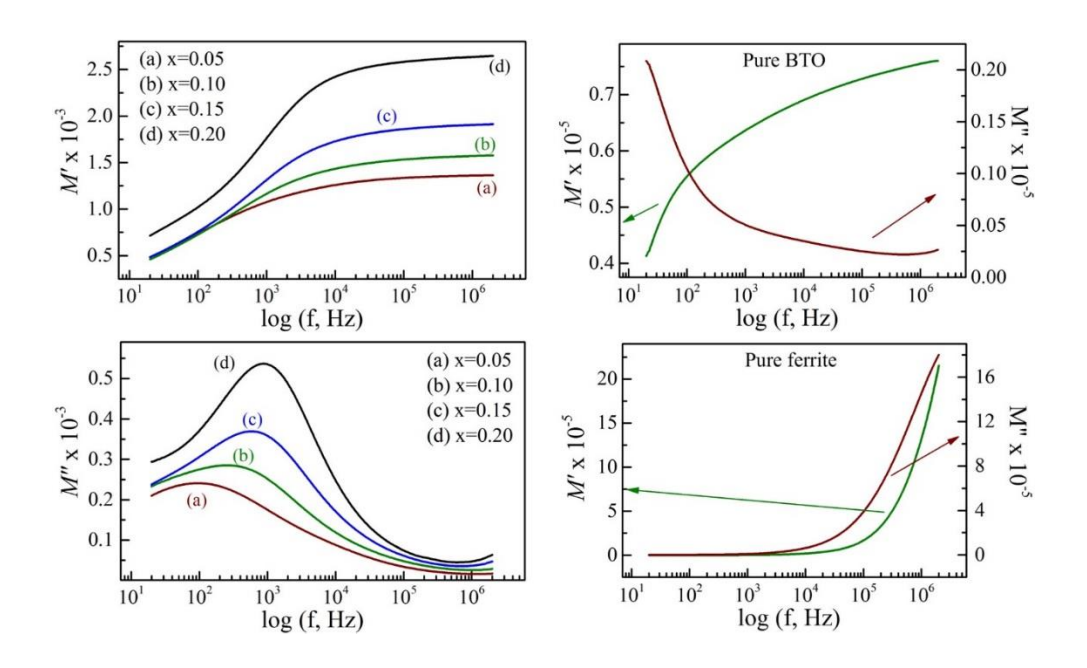


Figure 5.8. The M' and M" vs. frequency plots of the FM-FE composites and base materials.

The presence of maxima in imaginary electric modulus (M") vs. frequency plots (Fig 5.8) confirms the hopping mechanism of electrical conduction in the composites. The region near the peak suggests the transition from long to short-range mobility of charge carriers [31]. The asymmetric and broad peak indicates the existence of non-Debye relaxations similar to the dielectric spectra [13], [15], [21]. The non-Debye relaxation is attributed to the non-uniform microstructure and diffusive motion of the charge carriers in the composite [32]. The maxima of M" vs. frequency plots is shifting towards higher frequencies with an increase in ferrite content confirming that the conductivity of the

composite is increasing with an increase in ferrite content. Because for pure BTO maxima is along the lower frequency whereas for pure ferrite maxima is toward higher frequency.

5.5.2 Polarization study

The domain size, structure and wall movement are the major reasons for the ferroelectric properties of the composites. In common, the ferrite domains are bigger than the ferroelectric domains which cause strong magneto-electric coupling at the domain walls and give rise to the interesting multiferroics property [17].

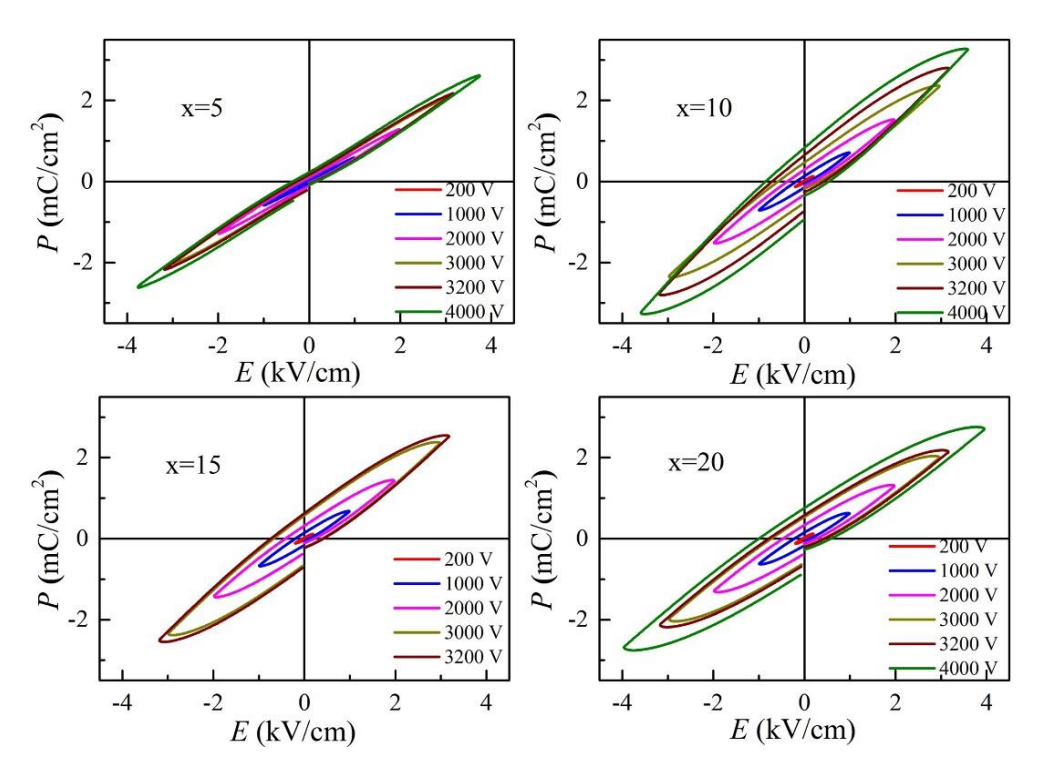


Figure 5.9 The polarization vs. electric field (P(E)) loop of the FM-FE composites.

Fig. 5.9 demonstrates the "ferroelectric hysteresis loop (P(E)) loop)" with various electric fields at room temperature for all the composites samples. The ferroelectric hysteresis loops show linear dielectric behavior at the lower electric field for all the composite samples. Whereas P(E) loops with positive curvature are obtained as the electric field is increased enough. The P(E) loop of positive curvature with an increase

in the electric field indicates the ferroelectric nature of composite samples with a high coercive field at room temperatures. Hence, the shape of the P(E) hysteresis loop confirms the ferroelectric ordering of the composites at room temperature. The positive curvature of the P(E) loop clears that the leakage current contribution is less. Generally, the leakage current contribution comes from the ferrite content due to the comparably low resistivity of ferrite. Because the iron ions (Fe³⁺ and Fe²⁺) creates the oxygen vacancy in ferrite which introduced the conductivity in the composite system [33].

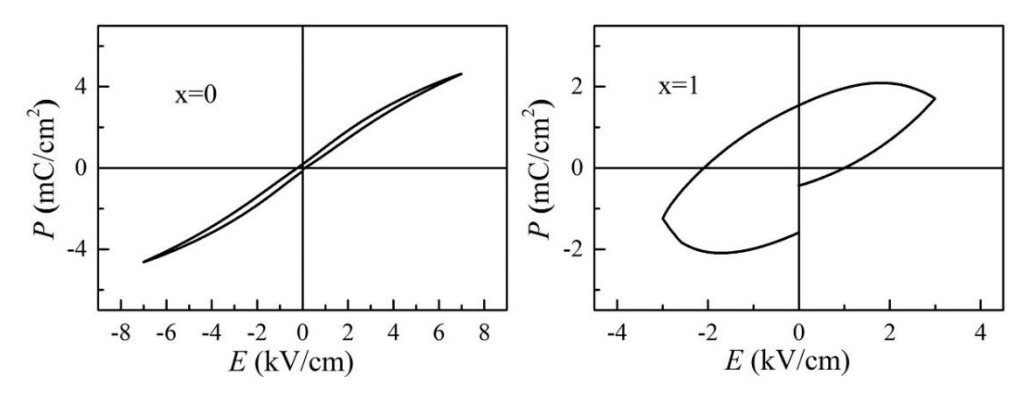


Figure 5.10 The P(E) loop of BTO (x=0) and ZMF (x=1).

Fig. 5.10 shows the P(E) loop of pure BTO and ZMF samples. A narrow loop is observed for pure BTO whereas for ZMF the loop is broad. The abnormal and broad hysteresis loop of pure ZMF sample indicates lossy behavior due to more conductivity of ZMF compare to BTO [34-35]. The polarization value of BTO is lower due to the porosity present in the system which is supported by the micrograph analysis [21]. Also, it is found that the P(E) loop shows a loop opening which may be due to the retention feature of the BTO ceramics [36-37].

Fig. 5.11 shows Ps vs. x (%), E_c vs. x (%), P_r vs. x (%), and E_s vs. x plots, respectively. All the values are calculated just before the breakdown voltage. The remnant polarization and coercive field increases with an increase of ZMF percentage with a lower value than pure BTO. Whereas a decrease of saturation polarization (P_s) and saturation field (E_s) is observed with an increase in ZMF content. The heterogeneous microstructure may be a possible reason for alteration in the interaction among the internal poles of the composite samples [38]. Generally, the coercive field is very much related to grain connectivity or

diffusivity at the grain boundaries of ZMF and BTO which depends on the relative theoretical density of the system. In this case, the composition of composite is affecting not only the relative density also it is changing the distance between the ferroelectric ions [17], [21]. This alters the interaction between the ferroelectric ions in the composite because the ferroelectric region is surrounded by the ferrite region. The grain boundaries create pinning centers in the magnetic domain walls of ZMF grains due to the defects formed at the interface of the boundaries, therefore the increase of E_c values with an increase of ZMF content in the composite is attributed to the pinning effect at grain boundaries [39-41].

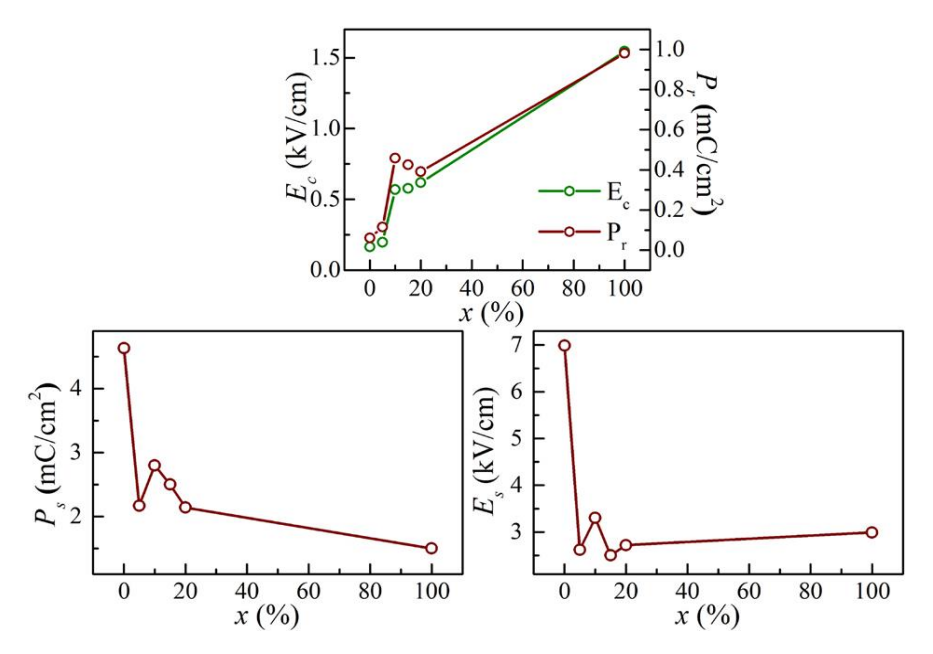


Figure 5.11 P_s, E_s, E_c, and P_r vs. x (%) plots for composites and base materials.

It is clear from Fig. 5.9 that all the P-E hysteresis loop becomes more saturated and the P_s increases gradually with an increase of electric field for all composites. Therefore to get a clear picture of this variation we have plotted P_s vs. x, E_c vs. x and P_r vs. x plots of FM-FE composites samples at different applied voltages as shown in Fig. 5.12. These plots clearly show that the saturation polarization (P_s), remnant polarization (P_r) and coercive field (E_c) increases with an increase of drive voltage.

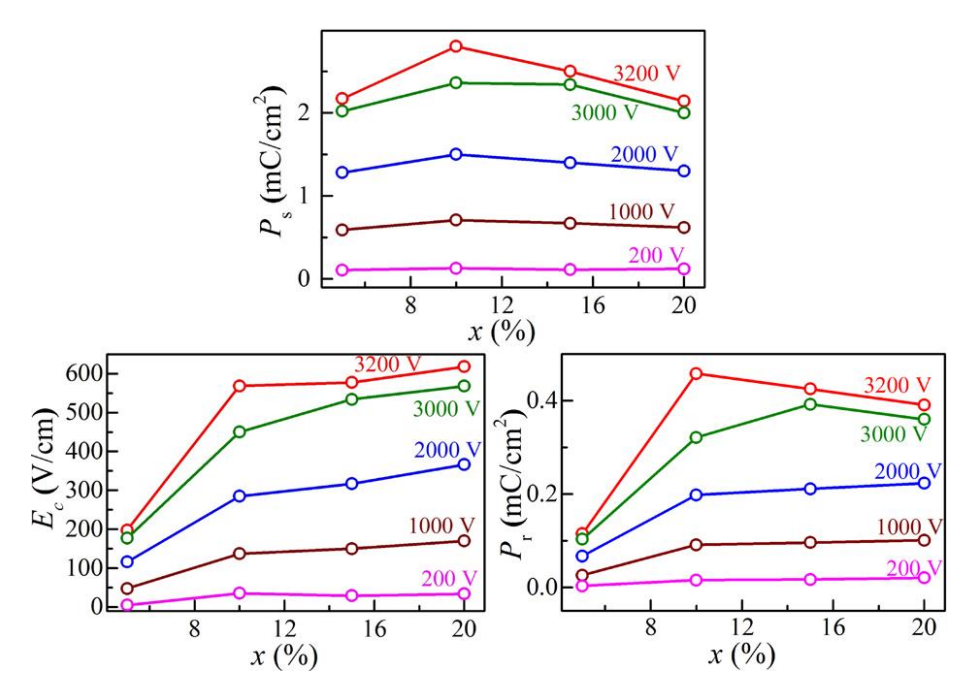


Figure 5.12. The P_s, E_c, and P_r vs. x (%) plots of composites at different applied voltages.

5.6 Chapter Summary

The composites were synthesized using the nanoparticles of $Mn_{0.5}Zn_{0.5}Fe_2O_4$ and $BaTiO_3$ via solid-state route. In summary, the multiferroic behavior of FM-FE composites by studying structure, magnetic, P-E loop, and dielectric properties is reported. The XRD and FESEM images confirm the coexistence of ZMF and BTO phases in the composites. The magnetization is found to increase through the inclusion of ferrite because of the mixture rule. The existence of a "magnetic hysteresis loop" and "P-E hysteresis loop" is an indication of magnetic and electric ordering in the FM-FE composites. The M(T) and dielectric properties also suggest the existence of FM and FE phases simultaneously. The FM-FE composites show a decrease in dielectric constant value with an increase in the dielectric loss by increasing ferrite-content. It is clear from the results that magnetic, electric and dielectric properties of composites strongly depend on the microstructure of the sample and ferrite percentage.

References

- 1. H. Schmid, Ferroelectrics **162**, 317-338 (1994).
- 2. N. A. Spaldin and M. Fiebig, *Science*, **309**, 391-392 (2005).
- 3. S. W. Cheong and M. Mostovoy, *Nature materials* **6**, 13 (2007).
- 4. C. W. Nan, *Phys. Rev. B* **50**, 6082-6088 (1994).
- 5. J. V. Suchtelen, *Philips Res. Repts.* **27**, 28-37 (1972).
- C. W. Nan, M. I. Bichurin, S. Dong, D. Viehland and G. Srinivasan, *J. Appl. Phys.* 103, 031101 (2008).
- 7. T. Kimura, T. Goto, H. Shintani, K. Ishizaka, T. Arima and Y. Tokura, *Nature* **426**, 55-58 (2003).
- 8. N. A. Hill, *J. Phys. Chem. B* **104**, no. 29 (2000).
- 9. J. Ryu, S. Priya, K. Uchino and H. E. Kim, J. Electroceramics 8, 107-119 (2002).
- 10. N. Ortega, A. Kumar, J. F. Scott and R. Katiyar, *J. Phys.; Condens. Matter.* **27**, 504002, 23 (2005).
- 11. M. Fiebig, J. Phys. D; Appl. Phys. 38, R123-R152 (2005).
- 12. J. V. Boomgaard and R. A. J. Born, *J. Mater. Sci.* **13**, 1538-1548 (1978).
- 13. J. Nie, G. Xu, Y. Yang and C. Cheng, *Mater. Chem. Phys.* **115**, 400-403 (2009).
- R. F. Zhang, C. Y. Deng, L. Ren, Z. Li and J. P. Zhou, *Mater. Res. Bull.* 48, 4100-4104 (2013).
- 15. J. Zhai, N. Cai, Z. Shi, Y. Lin and C. W. Nan, *J. Phys. D: Appl. Phys.* **37**, 823-827 (2004).
- 16. J. Ma, J.Hu, Z. Li, and C. W. Nan, *Adv. Mater.* **23**, 1062-1087 (2011).
- 17. A. Farheen, T. Gadipelly and R. Singh, Ferroelectrics **516**, 1-8 (2017).
- 18. R. W. McCallum, K. W. Dennis, D. C. Jiles, J. E. Snyder and Y. H. Chen, *Low Temp. Phys.* **27**, 266 (2001).
- 19. J. P. Zhou, L. Lv, Q. Liu, Y. X. Zhang and P. Liu, *Sci. Technol. Adv. Mater.* **13**, 045001, 12 (2012).
- 20. A. Farheen, T. Gadipelly and R. Singh, AIP Conf. Proceed. 832, 040019 (2017).

- 21. A. Farheen and R. Singh, *Integrated Ferroelectrics* **193**, 31-35 (2018).
- 22. A. Farheen and R. Singh, AIP Conf. Proceed. 1953, 120067 (2018).
- 23. S. K. Tripathy, T. Sahoo, M. Mohapatra, S. Anand and R. P. Das, *Mater. Lett.* **59,** 3543 (2005).
- 24. Z. Wang, W. Li, R. Chu, J. Hao, Z. Xu, G. Li, *Mater. Res. Bull.* **97**, 334-342 (2018).
- 25. B. D. Cullity, *Elements of X-ray diffraction*, Second Edition, Addison-Wesley Publishing Company Inc., United states of America, 32-85 (1978).
- 26. A. Farheen and R. Singh, *Material research express* **6**, 114001 (2019).
- 27. S. Y. Tan, S. R. Shannigrahi, S. H. Tan, and F. E. H. Tay, *J. App. Phys.* **103**, 094105 (2008).
- 28. L. P. Curecheriu, M. T. Buscaglia, V. Buscaglia, L. Mitoseriu, P. Postolach A. Ianculescu, and P. Nanni, *J. Appl. Phys.* **107**, 104106 (2010).
- 29. J. Smit and H. P. T. Wijn, *Ferrites*, Philips' tech. Library, Eindhoven (Holland) (1959).
- 30. C. G. Koops, *Phys. Rev.* **83**, 121 (1951).
- 31. V. Mohanty, R. Cheruku, L. Vijayan and G. Govindaraj, *J. Mater. Sci. Technol.* **30** (4), 335e341 (2014).
- 32. C. Liu, W. Wan, S. Gong, H. Zhang and W. Guo, Scientific reports 3856 (2017).
- C. E. Ciomaga, A. M. Neagu, M. V. Pop, M. Airimioaei, S. Tascu, G. Schileo,
 C. Galassi, and L. Mitoseriu, *J. Appl. Phys.* 113, 074103 (2013).
- 34. J. F. Scott, J. Phys.: Condens. Matter. 20 021001 (2008).
- 35. D. K. Pradhan, S. K. Barik, S. Sahoo, V. S. Puli, and R. S. Katiyar, *J. Appl. Phys.* **113**, 144104 (2013).
- 36. Y. P. Mao, S. Y. Mao, Z. G. Ye, Z. X. Xie, and L. S. Zheng, *J. Appl. Phys.* **108**, 014102 (2010).
- 37. S. K. Das, R. N. Mishra, and B. K. Roul, *Solid State Commun.* **191**, 19-24 (2014).

- 38. A. S. Dzunuzovic, M.M. V. Petrovic, , J. D. Bobic, N. I. Ilic, M. Ivanov, R. Grigalaitis, J. Banys and B. D. Stojanovic, *Ceramics International* **44**, 683-694 (2018).
- 39. M. Tyagi, M. Kumari, R. Chatterjee, and P. Sharma, *Appl. Phys. Lett.* **106**, 202904 (2015).
- 40. F. Li, J. Sun, X. Wang, and J. Wang, *IEICE Trans. Electron.* **E90–C**, 1561-1564 (2007).
- 41. J. Sun, Z. Wang, Y. Wang, C. Yao, K. Wei, T. Shen and F. Li, *Vacuum* **86**, 461-465 (2011).

Chapter 6

Summary and further scope

This chapter provides a summary of the work included in the thesis and main conclusions. The further scope of the work is also included in the chapter.

6.1 Summary of the present work

Magnetic nanoparticles, thin films and ferrimagnetic-ferroelectric (FM-FE) composites have several applications. The study of such systems is important and challenging to find improved material characteristics for research and development. Ferrite nanoparticles have the size up to nanometers dimensions, therefore surface-to-volume ratio of the particle increases which leads the alteration in physical and chemical properties of the ferrite. Therefore, nanoparticles of ferrites offer great advantages over bulk material and found to be useful in the field of medicine and biology such as magnetically targeted drug delivery, MRI, spintronics etc.

The study of the Mn-Zn ferrites thin films is of great interest due to the fundamental differences in their magnetic and electronic properties from the bulk counterparts. These films have the potential to replace the bulk external magnets in current devices. Ferrite thin films have been extensively investigated for use as a data storage medium in magneto-optic or magneto-recording systems. Ferrite thin films show high electric resistivity than the bulk counterpart. The difference in the properties of films compare to bulk arises because of large surface-to-volume ratio, less thickness, and unique microstructure of the films.

The FM-FE composite multiferroics offer a way to attain magnetic and ferroelectric ordering simultaneously. The simultaneous existence of ferroelectricity and magnetic ordering in multiferroic materials may lead to novel functionalities which are not present in either state alone. Therefore, the composites are essential for the development of magneto-electronic devices in different frequency regions. Moreover, the rarity of single-phase multiferroic systems leads to the necessity of preparing FM-FE composite materials. Therefore, the present thesis work covers

material properties in all three dimensions: (i) ferrite nanoparticles, (ii) ferrite thin film, and (iii) ferrite and BaTiO₃ composites ceramics.

A brief discussion about the materials which are used in the preparation of nanoparticles, thin films and composites is covered in the present thesis. The preparation method of ferrite nanoparticles, BaTiO₃ nanoparticles, thin-film and composites is also explained in the thesis. It covers the structural, microstructural, and magnetic behavior of Mn-Zn ferrite nanoparticles and thin films. Electrical behavior of the composites is also studied in the present work. The summary of the work included in the thesis is as follows:

- 1. The single-phase cubic spinel structure $Zn_xMn_{1-x}Fe_2O_4$ (ZMF) (x=0 to 1 with a step size of 0.1) nanoparticles were prepared by co-precipitation method. Phase formation was confirmed by XRD analysis. Rietveld analysis confirms the single phase cubic spinel structure with Fd-3m space group without any detectable impurity phase. Structural study also confirms the formation of nanosize ferrite nanoparticles ranging from 5 to 70 nm.
- 2. The crystallite size and lattice parameter of the ZMF nanoparticle increases with increasing Mn content.
- Microstructural and Raman studies complement the XRD results. EDAX
 analysis confirms the element present in the ZMF nanoparticles close to the
 starting composition.
- 4. Ferrimagnetic ordering of the ZMF nanoparticles is confirmed via magnetic hysteresis loop. It is found that the substitution of Mn²⁺ ion at tetrahedral site in Zn-ferrite enhances the ferrimagnetic interactions of the samples. These results confirm that magnetic properties rely on the cation distribution among lattice sites, microstructure and crystallite size of the nanoparticles. Variation in M(T) plots and FMR spectra also supports the M-H results.
- 5. In FMR spectra of ZMF nanoparticles, the resonance field decreases monotonically with an increment in the crystallite size of ZMF nanoparticles. This indicates an increment in ferrimagnetic interactions as the particle size increases. Further, a monotonic increase in linewidth and g-value with increasing Mn-doping also indicates that ferrimagnetic interaction is more for Mn-rich samples.

- 6. The Mn_{0.5}Zn_{0.5}Fe₂O₄ (MZF) films were fabricated by RF-magnetron sputtering on quartz substrates under different deposition conditions. The XRD pattern shows weak peaks which correspond to the cubic spinel structure of the target material.
- 7. The FESEM surface micrographs show the small nano-cluster formation in all the films. The columnar growth is also observed in all the films from the cross-sectional FESEM images.
- 8. The magnetization versus field (*M-H*) plots of the MZF films reveals the soft ferrimagnetic behavior of the films. Angular dependence of M-H plots also confirms the presence of anisotropy in thin films.
- 9. The resonance field (H_r) of the FMR spectra shifts towards a higher magnetic field when angle between applied field and thin-film plane is changed from 0 to 90°. This indicates the existence of uniaxial anisotropy in the MZF film. The FMR data complements the magnetization results.
- 10. The composites "(x) Mn_{0.5}Zn_{0.5}Fe₂O₄ + (1-x) BaTiO₃ (x=0.05, 0.10, 0.15, 0.20)" were synthesized using the nanoparticles of Mn_{0.5}Zn_{0.5}Fe₂O₄ and BaTiO₃ (BTO) via solid-state reaction process. The XRD and FESEM images confirm the coexistence of ferrite and BTO phases in the composites. All the peaks in the XRD pattern of the composites are assigned to ZMF and BTO phases with no other detectable third phase.
- 11. The existence of ferrimagnetic and ferroelectric phase is also confirmed by EDAX. The small spherical particles correspond to BTO whereas the disc-shaped bigger particles correspond to ZMF.
- 12. BaTiO₃ (BTO) has "perovskite structure" with lattice constants "a = 3.994 Å" and "c = 4.033 Å" ("XRD PDF pack No. 831880"). Whereas, Mn_{0.5}Zn_{0.5}Fe₂O₄ has "cubic spinel structure" with lattice constant "a = 8.453 Å (XRD PDF pack No. 7423398"). Almost double value of lattice constant of ferrite than BTO ensures good interface matching between ferrite and ferroelectric phases.
- 13. In particular, the optimization of ferrite percentage in composite is crucial because their resistivity is not good enough to use at high voltage. Since

- higher ferrite content may lead to a significant decrease in the electrical properties, we have used only up to 20% of ferrite.
- 14. The existence of "magnetic hysteresis loop" and "*P-E* hysteresis loop" is an indication of magnetic and electric ordering in the FM-FE composites. The magnetization is found to increase with the inclusion of ferrite as per the mixture rule.
- 15. The simultaneous existence of ferroelectric phase dilutes the magnetic moment due to the reducing amount of ferrite phase. As expected, the observed magnetization value of composites is less than the ZMF samples because of the "dilution effect" of ferrimagnetic phase with the existence of non-magnetic BTO phase. Since the ferrite (ZMF) grains are in the matrix of ferroelectric material (BTO), therefore ferrite grains will be separated by BTO grains.
- 16. The variation of thermomagnetic (M(T)) and dielectric properties indicate the coexistence of ferrimagnetic and ferroelectric phase. The FM-FE composites show a decrease in dielectric constant value and an increase in dielectric loss with increasing ferrite-content. It is clear from the results that magnetic, electric and dielectric properties of composites strongly depend on the microstructure of the sample and composition.

6.2 Further Scope of the present work

As per the conclusion drawn from the thesis, the present field has a scope for further investigations on various aspects of nanoparticles, thin films and FM-FE composites. Based on the above results, the following important work can be done in the future:

- 1. A complete study of ferrite nanoparticles, including the effect of sintering, can be done. The dielectric, resistivity and ESR studies as a function of temperature will be useful.
- 2. Optimizing different synthesis conditions for getting highly dense FM-FE composites for achieving good multiferroic properties.
- 3. A detailed study of FM-FE composite using Raman Spectroscopy, TEM analysis and temperature-dependent dielectric studies.

4. Fabrication of FM-FE composites thin films (multilayers) by using RF magnetron sputtering or pulse laser deposition (PLD). And detailed study of FM-FE composite films.

Synthesis and Study of Zn(Mn) Ferrite Nanoparticles, Thin Films and Zn(Mn) Ferrite-BaTiO3 Composites

by Atiya Farheen

Submission date: 15-Jun-2020 10:57AM (UTC+0530)

Submission ID: 1344036398

File name: Thesis Complete Final Atiya Farheen 14phph03 Library.pdf (6.56M)

Word count: 21340

Character count: 112472

Synthesis and Study of Zn(Mn) Ferrite Nanoparticles, Thin Films and Zn(Mn) Ferrite-BaTiO3 Composites

19%

4%

17%

7%

SIMILARITY INDEX

INTERNET SOURCES

PUBLICATIONS

STUDENT PAPERS

PRIMARY SOURCES

Atiya Farheen, Rajender Singh. "Synthesis of ferrimagnetic/ferroelectric composite and its magnetic and electrical characterization", Integrated Ferroelectrics, 2019

4%

Publication

Atiya Farheen, Rajender Singh. "Effect of hydrothermal annealing on structure and magnetic properties of RF sputtered Mn-Zn Ferrite thin films", Materials Research Express, 2019

3%

Publication

Atiya Farheen, Rajender Singh. "FMR and Magnetic Studies of RF-Sputtered Mn-Zn Ferrite Thin Films", Journal of Superconductivity and Novel Magnetism, 2019

3%

Publication

Atiya Farheen, Rajender Singh. "Structure and magnetic properties of superparamagnetic ferrite nanoparticles", IOP Conference Series: Materials Science and Engineering, 2019

2%

5	Atiya Farheen, Rajender Singh. "Effect of Mn Substitution on Structure and Magnetic Properties of Cobalt Ferrite Nanoparticles", Integrated Ferroelectrics, 2019	1%
6	Atiya Farheen, Rajender Singh. "Effect of sintering on structure and magnetic properties of Mn-doped Zn ferrite", AIP Publishing, 2018 Publication	1%
7	Atiya Farheen, Thirupathi Gadipelly, Rajender Singh. "Multiferroic properties of ferromagnetic and ferroelectric coupled Mn-Zn ferrite-BaTiO composite ", Ferroelectrics, 2017 Publication	1%
8	Submitted to Higher Education Commission Pakistan Student Paper	<1%
9	Submitted to University of Hyderabad, Hyderabad Student Paper	<1%
10	Submitted to Indian Institute of Technology Guwahati Student Paper	<1%
11	Submitted to Savitribai Phule Pune University Student Paper	<1%

12	aip.scitation.org Internet Source	<1%
13	worldwidescience.org Internet Source	<1%
14	shodhganga.inflibnet.ac.in Internet Source	<1%
15	Submitted to University of Pune Student Paper	<1%
16	Submitted to Indian Institute of Technology, Madras Student Paper	<1%
17	M Sultan. "Structural and optical properties of RF-sputtered ZnFe ₂ O ₄ thin films", Journal of Physics D Applied Physics, 06/07/2009	<1%
18	Submitted to Universiti Teknologi Malaysia Student Paper	<1%
19	Submitted to National Institute of Technology, Rourkela Student Paper	<1%
20	Submitted to IIT Delhi Student Paper	<1%
21	Kalim Deshmukh, Sowmya Sankaran, Basheer Ahamed, Kishor K. Sadasivuni et al. "Dielectric	<1%

	Spectroscopy", Elsevier BV, 2017 Publication	
22	Springer Theses, 2014. Publication	<1%
23	Submitted to University of Warwick Student Paper	<1%
24	M. Sultan, R. Singh. "Magnetic and optical properties of rf-sputtered zinc ferrite thin films", Journal of Applied Physics, 2009 Publication	<1%
25	Bijoy K. Kuanr, R.E. Camley, Z. Celinski. "Extrinsic contribution to Gilbert damping in sputtered NiFe films by ferromagnetic resonance", Journal of Magnetism and Magnetic Materials, 2005 Publication	<1%
26	Submitted to University of KwaZulu-Natal Student Paper	<1%
27	hdl.handle.net Internet Source	<1%
28	Submitted to Birla Institute of Technology and Science Pilani Student Paper	<1%

Submitted to University of Sheffield

Student Paper

30	Submitted to Kyungpook National University Student Paper	<1%
31	Ghasemi, A "The role of copper ions on the structural and magnetic characteristics of MgZn ferrite nanoparticles and thin films", Journal of Magnetism and Magnetic Materials, 201010 Publication	<1%
32	Submitted to Malaviya National Institute of Technology Student Paper	<1%
33	Ari Ben-Menahem. "Historical Encyclopedia of Natural and Mathematical Sciences", Springer Science and Business Media LLC, 2009 Publication	<1%
34	iopscience.iop.org Internet Source	<1%
35	cnr.it Internet Source	<1%
36	Submitted to University of Sydney Student Paper	<1%

Exclude quotes

On

On

Exclude matches

< 14 words

Exclude bibliography